ON A GENERAL THEORY OF PHASE CHANGE, NUCLEATION, AND GROWTH, AND THE FORMATION OF ICE IN CRYOPRESERVED SYSTEMS

A DISSERTATION
SUBMITTED TO THE FACULTY OF THE
UNIVERSITY OF MINNESOTA
BY

Joseph R. Kangas

IN PARTIAL FULFILLMENT OF THE REQUIREMENTS
FOR THE DEGREE OF
DOCTOR OF PHILOSOPHY

Professor John C. Bischof, Co-advisor
Professor Christopher J. Hogan Jr., Co-advisor

January, 2023

Acknowledgements

I would like to thank my advisors Dr. Chris Hogan and Dr. John Bischof for providing me with guidance, as well as giving me the academic freedom to pursue my own ideas on my own terms. I would also like to thank my labmates for helping me become a better scientist and teacher, and for broadening my intellectual horizons. I'd also like to thank my parents for helping and supporting me throughout my schooling

I would like to extend my gratitude to the Minneapolis Institute of Art, for providing me a space to think clearly about my research; and to Bach, Ravel, Chopin, Scriabin, and Beethoven for calming my anxious mind.

I would like to thank the National Science Foundation Engineering Research Center, ATP-Bio, for providing me with the funding necessary to complete this work, as well as providing an avenue for multidisciplinary collaboration.

I extend my thanks to all those who asked me about my thesis, and then never asked again. You made me feel like the Godfather.

I would also like to thank myself, without which most of this work could not have been accomplished.

Finally, I would like to thank the mostly horrible programming on Netflix, without which I would not have been bored enough to derive the material in chapter 2 for fun. Math can be fun!

Abstract

In this work we address longstanding gaps in understanding in phase change theories linking the nucleation rate, growth rate, growth geometry, and transformed fraction of phase. We take a first principles approach whereby a fundamental understanding of the relationships between these properties can be derived without obfuscation by previous efforts. This is carried out by examining a growing region of space with some prescribed geometry which is transforming from one phase to another, tracking its volume as it grows and intersects with other transforming regions of space. Using this approach, we derive both ordinary and partial differential equations linking the nucleation rate, growth rate, fractal dimension, transformed fraction, phase size distribution, and initial distributions of phase for a system undergoing phase change. We then show that solutions to these equations under special conditions yield methods for extracting nucleation and growth rates for heat release curves, as well as more detailed descriptions of growth geometries. These nucleation and growth rates are important for understanding systems hindered by phase change, including cryobiology, metallurgy, pharmacology, and food science, among others. Extensions to gas phase allow for a deeper understanding of aerosol science and cavitation dynamics as well.

Ice crystallization is studied in cryoprotectant agents (CPAs) in low concentrations via direct quenching and laser calorimetry. Critical cooling rates were measured by examining the temperature-time profiles during the direct quenching of droplets of CPA into liquid nitrogen. Critical warming rates were measured by examining ice crystallization in vitrified droplets of CPAs and plasmonic gold nanoparticles during high energy laser irradiation. High-speed imaging allowed for accurate measurements of the temperature rates necessary for avoiding ice formation on rewarming from a vitrified state. A model linking the critical cooling and warming rates in mixtures of CPA was also developed and verified. Additionally, the phase change theory we derived allow for corroboration of the rates necessary for the vitrification of pure water.

The laser warming process was also studied numerically via Monte Carlo simulations of light transport in scattering media. The effect of system geometry, absorption coefficient, scattering coefficient, scattering anisotropy, and domain partitioning were studied for a variety of systems including the laser warming of spherical and hemispherical droplets laden with zebrafish embryos and coral nanofragments. Warming uniformity was the main focus of optimization as it is the driving factor in post-warming survival in laser warmed cryopreserved specimens. Laser warming in multi-laser systems is also briefly discussed.

Table of Contents

List of Figures

List of Tables

Chapter 0

Introduction

The original motivation for this work was to better our understanding of cryopreservation (the viable freezing and thawing) of biological substances; however, this work has blossomed into a broader theory of phase change, clarifying the relationships between nucleation, growth, phase geometry, and transformed fraction. This work starts by giving a broad overview of the topics covered in this thesis in chapter 1, which includes an overview of crystal nucleation, growth, and crystal geometry, as well as an overview of cryopreservation and cryoprotectants. This is to provide the reader with sufficient background information to understand the derivations, arguments, and analysis throughout the rest of this work. This chapter, aptly titled chapter 0, will address the objectives, overview, and significance of the work presented, while chapter 1 will address the technical background.

This work has two main aims that fall under one broad category: phase change. The first aim is to develop a theoretical model to better understand the process of phase change, particularly how nucleation, growth, phase geometry, and transformed fraction are linked.

This model should be based on first principles and should be so sufficiently clear as to make the reader ponder not on how it *can* be true, but rather on how it *must* be true. Additionally, we seek to test this model against real world and simulated data to further bolster its validity. The second aim is to better understand the crystallization tendency in low concentration cryoprotective agents (CPAs) so that we may better design cooling and warming protocols. This requires the measurement and modeling of critical cooling and warming rates and their relationship with concentration, as well as modeling the laser warming process itself. Our ultimate aim is to find the ideal concentrations of CPA and gold nanoparticles to maximize temperature uniformity and minimize ice formation during the cooling and warming of cryopreserved specimens.

In chapter 1 we provide a background of the thermodynamics of crystallization and vitrification. We discuss what a phase is with regards to phase change, with particular importance to the solid crystal and amorphous glass phases of water and aqueous solutions. Mathematical descriptions of crystal nucleation and growth are given in terms of fundamental parameters. Additionally, we introduce the topics of cryopreservation, vitrification, and cryoprotectants, as well as common protocols for cryopreserving biological specimens.

In chapter 2 we take a first principles approach to describing phase change by first considering a singular growing spherical region of space, where the boundary of the sphere partitions the space into two separate phases. By prescribing a constant velocity to the surface of the growing sphere, we create a simple description of a growing spherical crystal. To model nucleation, we consider these spheres being formed uniformly randomly throughout the greater space at some constant nucleation rate. We devised a way to compensate for the overlap of these growing spheres, ultimately deriving a nonlinear differential equation (we call this the GNA equation) linking the nucleation rate, growth rate, and transformed fraction. Next, we derived a first order partial differential equation (PDE) describing the sphere (phase) population size distribution, and its solution in terms of the nucleation rate and growth rate of the system, as well as the initial distribution of transformed phase. By integrating the phase size distribution with respect to the volume of a growing sphere, we provided a link between the phase size distribution and transformed fraction, and thus the GNA equation, allowing for the derivation of the initial conditions to said differential equation. The nucleation and growth rates for water were then calculated based off classical nucleation theory and values of fundamental parameters found in the literature. We then simulated the phase size distributions for water that was cooled and rewarmed isothermally, ultimately accurately predicting the critical cooling rate of pure water. The general behavior of the solutions to the PDE and GNA equation are also discussed. The significance of the theory derived in this chapter lies in our deconvolution of the classic integral phase change relations into a differential equation linking nucleation, growth, and transformed fraction, thereby allowing for the determination of one of these variable, provided the other two are known. This lays the framework for chapter 3, whereby we build on the theory presented in chapter 2 and leverage it to determine growth and nucleation rates from calorimetry curves.

In chapter 3, we take what we learned in chapter 2 and apply it to an isothermal phase change process. Isothermal phase change processes are well described by the Avrami equation and associated Avrami parameters, which describe how the transformed fraction changes with time. These Avrami parameters are rarely known in terms of fundamental parameters outside of idealized cases, such as perfect isothermal constant spherical growth. We use solutions to the PDE presented in chapter 2 to derive the exact values of these parameters in terms of the nucleation rate, growth rate, and fractal dimension. Next, we showed that the solutions resulting from a step change in temperature could be used to estimate the relative change in the growth rate and nucleation rate, as well as the absolute change in fractal dimension from the resulting heat release calorimetry curves associated with a step change in temperature during an isothermal phase change process. To test our new theory, we simulated the growth of diffusion limited aggregation “pseudo-crystals” which grew in a fractal manner similar to snowflake growth. When these simulated crystals grew, they released heat according to some arbitrary temperature dependent latent heat value. We then used this heat release and treated it as a heat release curve from a differential scanning calorimetry experiment. Then, by using the protocol derived from the theory in this chapter, we were able to estimate the change in growth and nucleation rate from simulated DLA heat release curves with high fidelity. We ultimately showed that we now have a protocol to derive nucleation and growth rates from calorimetric curves, radically advancing the field in this space.

In chapter 4 we shift directions to experiments measuring ice crystallization in cryoprotective agents during both cooling and warming. We examine a mixture of several common cryoprotectants in microliter-scale droplets, measuring both the critical cooling rates and critical warming rates. For the critical cooling rate measurements, droplets of variable size in the microliter range were placed on a cryotop fastened with a thermocouple. This droplet was quenched directly into liquid nitrogen then subsequently imaged to optically assess for ice crystallization. Droplets were categorized as either vitrified or not vitrified based on the absence or presence of ice respectively. If ice was present, the droplet volume was reduced, thus increasing the cooling rate, until no further ice formed. If there was no ice present, the droplet volume was increased, thus decreasing the cooling rate until ice was present. The critical cooling rate for that particular CPA was the rate associated with the visual detection threshold for ice. This was carried out for a variety of CPA mixtures and concentrations. To measure the critical warming rates, droplets were formed in a similar fashion with the addition of plasmonic nanoparticles, which readily convert infrared laser light into heat. These droplets were then cooled sufficiently above the critical cooling rate as to remain ice-free. Next, the vitrified droplets were fired upon with a high-energy infrared laser, rapidly warming the droplets. The warming took place over a few milliseconds, warming the droplets on the order of a million degrees per minute. High-speed imaging of the droplet during warming allowed for the visual detection of ice similar to the critical cooling rate experiments. The warming rates were modulated by adjusting the energy of the laser so that the visual detection threshold, and thus the critical warming rate for that particular CPA, could be determined. Using the data gathered in the critical cooling and warming experiments, a model for determining the critical cooling and warming rates for mixtures of CPAs was tested and verified. This model allowed for the prediction of these rates in mixtures of CPAs given knowledge about their constituents. Additionally, extrapolations of critical cooling and warming rates of the CPAs allowed for the prediction of the critical cooling rate and warming rate of pure water, which showed strong agreement from the predictions made by the theory outlined in chapter 2.

In chapter 5 we take a closer look at the warming of cryopreserved droplets, simulating the light transport within various constructs that exhibit scattering and absorbative properties. We implemented a Monte Carlo algorithm to track photons as they propagate through several different environments. In this type of simulation, many photon trajectories were simulated throughout the environment (e.g., a droplet of CPA) which may refract through or reflect off a boundary, be absorbed, scatter, or transmit in this simulated environment. By averaging tens of thousands of photons trajectories, we were able to calculate a specific absorption rate or SAR (the volumetric heat source function associated with laser warming). By adjusting various optical properties such as the scattering and absorption coefficients or scattering anisotropy, we were able to estimate the ideal values of these properties given system constraints such as the index of refraction and domain shape. We analyzed laser warming profiles in hemispherical and spherical droplets, as well as droplets laden with zebrafish embryos, artemia, and other cells. We determined the ideal scattering and absorption coefficients, and thus gold nanoparticle concentrations, for these various systems which allowed for the optimization of warming protocols and thus increasing post-warming cell survival.

The theoretical work presented on phase change throughout this thesis is an important advancement in the understanding of phase change, particularly for those interested in crystallization, nucleation, and growth dynamics. We present a theory which not only deepens our understanding of the relationship between these phenomena, but also provides a framework for their measurement as well, which is of particular importance in metallurgy, polymer science, food science, pharmacology, and cryobiology. Additionally, the work we present on critical cooling and warming rates fills an important gap in our knowledge of these rates in low concentration CPAs, which is important for systems that poorly tolerate CPA, such as aquatic embryos and pancreatic islets. Finally, the Monte Carlo simulations presented help fine tune the warming protocols used in low concentration cryopreservation, which is necessary for increasing cell survival and throughput. We will now provide a technical background related to the topics throughout this thesis, covering an overview of the thermodynamics of crystallization and vitrification.

Chapter 1

The Thermodynamics of Crystallization and Vitrification

1.1 Introduction

Changes between thermodynamic states involve abrupt changes in thermodynamic properties, loss or gain of molecular degrees of freedom, and the breaking or formation of symmetries. These phase changes characterize the transition between liquids, solids, gasses, and plasmas, bar the exotic phases of which we need not concern ourselves. Of these transitions, the transition between solid and liquid states (vitrification, crystallization, and melting) is of particular importance to our studies throughout this work. A crystal is an ordered lattice of molecules or atoms with periodic symmetry resulting from the thermodynamic phase change from liquid to solid, or even from solid to solid. Crystals and crystal-like structures are found throughout nature, ranging in size from nanometers to meters and forming over both human and geological timescales. They are important in the study of geological processes due to their immense resilience and physical structure. For example, zircon crystals (a tetragonal crystal of zirconia silicate) are so resilient that they have survived the Hadean epoch in the Earth's most early history, with uranium-lead radiometric dating showing some crystals found in Western Australia to be over 4.4 billion years old.[1] Additionally, these crystals have shown evidence of liquid water over 4.4 billion years ago and biological life over 4.1 billion years ago on Earth's surface.[2,3] Diamond is an additional crystal formed on geological timescales. Aside from its aesthetic beauty, the hexoctahedral carbon structure constituting diamond gives it a variety of properties, including extreme hardness, high refractive index, high electrical resistance, and the highest thermal conductivity of any naturally occurring known substance. These properties can be attributed to the dense crystal structure that allows for very efficient phonon (the quanta of thermal vibrations) propagation throughout the crystal.[4] Both zircons and diamonds are examples of crystals that form under extreme thermodynamic conditions over incomprehensible lengths of time. On everyday time scales one may notice the crystallization of sugar when failing an attempt to make caramel, or those due to supersaturation in cold maple syrup. Perhaps the most salient example of crystallization is crystalized water, more commonly referred to as water-ice. Due to the unique nature of water, ice crystallization exhibits a wide variety of geometries and crystallization types. For example, small changes in the humidity and atmospheric pressure can lead to a seemingly endless variety of snowflake shapes and sizes (though small nano-snowflakes can in fact be identical). For average size snowflakes, it has been estimated that there are over 10^{150} possible configurations of the ice crystals, meaning that no two snowflakes will ever repeat in the lifetime of the observable universe.[5] It is then no surprise that water has a complex phase diagram for the solid state, see Figure 1.1, with many different crystal structures and densities of ice possible throughout the temperature and pressure regime. The transition between the liquid state and common ice (Ih) is what is typically meant by "freezing"; however, the importance of other liquid-ice transitions will be discussed later.

The formation of ice in aqueous systems is of particular importance in the cryopreservation of biological systems. The cascade of effects associated with ice formation including changes in pH, osmotic pressure, available water, and physical changes in cell shape and volume all contribute to cell damage and cell death when water crystalizes in biological systems.[6] For direct physical damage, the shape of the ice crystals is particularly important. Dendritic and spicular ice crystals are especially damaging as their high aspect ratio draws parallels to needles, easily puncturing cells and causing widespread membrane damage.[7] Thus, understanding the location and rate of ice formation in cells is important for designing current and future cryopreservation protocols; therefore, we will direct our focus to the of the crystallization of water.

One can think of crystallization as an energy minimizing process whereby the molecules, water in the cases we are concerned with, must reorient themselves into a lower energy ordered state. Due to the sudden drop in entropy, the water molecules in the new crystal lattice give off heat as a byproduct. Although under ordinary conditions we might treat this process as happening instantaneously, there is indeed a speed of this process, and thus a characteristic time for the molecules to reorient themselves into the newly formed crystal lattice. Clearly, under isothermal conditions below the melting point, the formation of a complete crystal is inevitable; however, if the temperature is reduced during this crystallization process, then the viscosity of the system rises and thus the molecules have a more difficult time moving, increasing the crystallization time. If we rapidly reduce the temperature of a system starting from its melting point T_m, it is possible to outpace the reorienting of water molecules entirely and avoid crystallization. Since viscosity rises exponentially as temperature decreases, we eventually reach a point where the viscosity is so high that molecular motion essentially ceases on time scales relevant to humans. This is the so-called *glass transition* temperature T_g. This glass transition is not a thermodynamic phase change process in the traditional sense, but rather a consequence of a loss in the major degrees of freedom in the liquid.

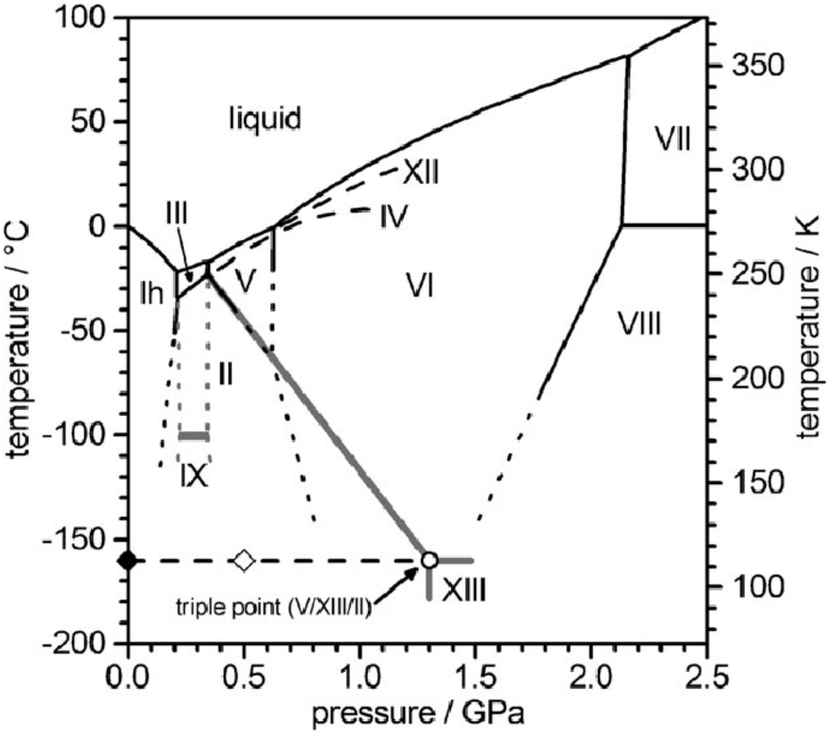

Figure 1.1. The phase diagram for liquid and solid water of various crystal structures and densities.[8]

This process is referred to as *vitrification,* where the substance is simply a supercooled liquid, or an amorphous glass, with effectively no molecular motion. This is the ideal state for long term storage of biological specimens, as metabolic processes cease to function, with the only damage to cells from light, particularly high energy cosmic rays.[9] Once in this vitrified state a substance may be stable for an immense period of time (decades to thousands or even millions of years given our current understanding of the processes involved). Once vitrified, the system can be brought back to the liquid state by warming at sufficiently rapid rates such that the water molecules don't have time to come together and form crystals of appreciable scale. The rates required to vitrify a substance and then bring it back to the liquid state without crystallization (devitrification) are the critical cooling rate (CCR) and critical warming rate (CWR) respectively. Through modulation of viscosity and other thermodynamic properties, the CCR and CWR, and thus the glass forming tendency, can be altered. Chemicals that have these properties are known as cryoprotective agents (CPAs) and help suppress the formation of ice during cryopreservation. To examine these CPAs and their associated CCRs and CWRs in more depth we must first review the thermodynamics of crystallization.

Table 1.1. A table of some of the most used parameters involving the thermodynamics and kinetics of phase change used throughout this chapter.

PARAMETERS	DESCRIPTION	UNITS
J	Nucleation Rate	$m^{-3}s^{-1}$
u	Crystal Growth Rate	ms^{-1}
T_m	Meting Temperature	K
T_g	Glass Transition Temperature	K
T_H	Homogeneous Nucleation Temperature	K
$\mathit{\Delta} H_m$	Melting Enthalpy	J
$\mathit{\Delta} h$	Specific Melting Enthalpy	$J\ kg^{-1}$
$\Delta\mu$	Chemical Potential of the Liquid Phase	$J\ kg^{-1}$
ΔG_{cr}	Free Energy of Formation of the Crystal Phase	J
ΔG_N	Free Energy of Formation of a Critical Nucleus	J
C_p^s	Specific Heat of the Supercooled Liquid Phase	$J\ kg^{-1}K^{-1}$
C_p^{cr}	Specific Heat of the Crystal Phase	$J\ kg^{-1}K^{-1}$
γ_e	Crystal-Liquid Interfacial Surface Energy	$J\ m^{-2}$
η	Dynamic Viscosity	$Pa\ s$
d_0	Mean Molecular Diameter	m
ρ_s	Number Density of Nucleation Sites in the Supercooled Liquid Phase	m^{-3}
D_*	Nuclei Diffusion Coefficient Across the Free Energy Barrier	s^{-1}
R_*	Critical Radius of a Crystal Nuclei	m
n_*	Number of Molecules in a Critical Nuclei	m
i_*	Number of Molecules on the Surface of a Critical Nuclei	m
k_B	Boltzmann Constant	$J\ K^{-1}$

1.2 Thermodynamics of Crystallization

The thermodynamics of crystallization can be broken up into two separate processes: nucleation and growth. Nucleation is the process by which molecules come together to form stable nuclei, while growth describes how the geometry and characteristic length of the nuclei changes with time.

1.2.1 *Nucleation*

Nucleation involves the stable formation of small collections of particles (nuclei), from a sea of particles, thermodynamically favored to grow, or at the very least, to not shrink. Underlying this description are several key assumptions. First, that there is some sea of particles in which the nuclei can form. Second, that these particles aggregate to form metastable clusters which may grow or disassociate randomly to do intermolecular interactions with the surrounding particles as well as intramolecular interactions within the cluster itself. These metastable clusters are constantly forming, growing, and disassociating within this sea of particles; however, after attaining a certain size, the critical radii, the metastable proto-nuclei transform into stable nuclei which can then grow in a more stable fashion. The rate that these stable nuclei form from the sea of particles is called the nucleation rate, which gives the number of nuclei formed per unit volume per unit time. Though the process is simple enough to describe, accurate mathematical descriptions of these processes remain a challenge. The main difficulty with describing nucleation is that we would like to paint a picture of reality using continuous functions, differential equations, and familiar geometry; however, the processes underlying nucleation lend themselves better to descriptions by molecular dynamics and stochastic simulations, which ultimately give rise to the emergent phenomenon we are seeking to describe. Additionally, it is not clear that a critical radius exists differentiating proto-nuclei from stable nuclei, or even that there is a clear boundary between the crystal and liquid phases on scales that miniscule. Another complicating factor is that thermal fluctuations driving nucleation and sub-nuclei growth occur on length scales of 10^{-10} meters and time scales of 10^{-13} seconds, comparable to the vibrational frequencies of the atoms constituting the nuclei.[10]

Many theories have been developed to understand and predict nucleation, but the first and most widely used is classical nucleation theory (CNT). We will focus our discussions here mostly to CNT, though the readers should be aware that many other theories exist. Density functional theories seeks to express the free energy of formation of the nucleus as a functional of molecular number density and intermolecular potentials. Functional theories seek to describe systems of many particles using functionals (functions of functions). In particular, for theories applied to nucleation, they require intermolecular potentials which are in general not known outside of extremely simplified and idealized systems.[11] Another approach that seeks to eliminate the sharp boundaries between phase is diffuse interface theory, a phenomenological theory that inserts an interface thickness into standard CNT to modify the underlying equations, to limited success. A nonclassical approach adds an extra step to the nucleation process. These two-step nucleation theories suppose the system first transitions to a solid-liquid mix, perhaps an amorphous solid, which then transitions into the crystalized state.[12] These two-step theories have shown a fair bit of success but complicate the processes by adding more unknown terms to be either assumed or extracted empirically via simulations and fitting. Though these theories have their own merits and potential for use, for the purposes of this work we only consider that a nucleation rate exists and can be expressed in terms of fundamental parameters that have measured values, making CNT the obvious choice.

1.2.1.1 *Homogeneous Nucleation*

Nucleation can be broken down into two categories: heterogeneous nucleation and homogeneous nucleation. Homogeneous nucleation is nucleation in the bulk of the substance, whereby particles come together to form metastable clusters which grow and dissolve until they surpass some critical size threshold. For heterogeneous nucleation, particles can attach themselves to preexisting structures such as features in the environment, like scratches, or even to other particles, thus surpassing the free energy of formation barrier that favors small clusters of particles to dissolve. The free energy of formation of a nucleus can be thought of as the sum of a volume-dependent energy contribution and a surface area dependent energy contribution, seen in equation (1.1). The surface term, $4\pi r^2\gamma_e$, with interfacial surface energy γ_e, corresponds to the energy contribution caused by the formation of the surface, which naturally resists an increase in surface area. The volume term, $-\frac{4}{3}\pi r^3\Delta\mu$, with chemical potential $\Delta\mu$, describes the energy released via the formation of new volume, akin to the enthalpy of fusion. For small radius nuclei, the surface term dominates, and growth is unfavorable, while for large radius nuclei the volume term dominates, and growth is favorable. This surface and volume contributory effect is outlined in Figure 1.2.

$$\Delta G = 4\pi r^2\gamma_e - \frac{4}{3}\pi r^3\Delta\mu \tag{1.1}$$

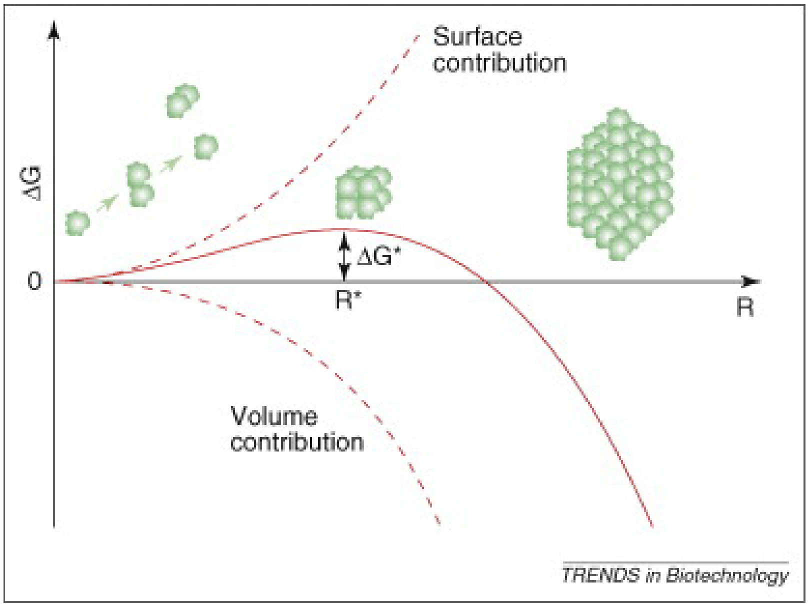

Figure 1.2. The free energy of formation ΔG vs radius of a growing nucleus, showing the peak in free energy corresponding to the critical radius.[13]

The free energy of formation ΔG_N of a critical nucleus of a crystal in a super cooled liquid can be defined by equation (1.2)[14], where γ_e is the interfacial solid-liquid surface energy of the critical nucleus, ρ_s is the density of the supercooled water, and $\Delta\mu = \Delta h \Delta T / T_m$ is the chemical potential defined in terms of the specific melting enthalpy and melting temperature of water. This can be solved by finding the maximum value ΔG takes in equation (1.1).

$$\Delta G_N = \frac{16\pi}{3} \frac{\gamma_e^3}{\rho_s^2 \Delta\mu^2} \tag{1.2}$$

This ΔG_N is the energy barrier that must be overcome for a stable nucleus to form. In liquids at or above the melting temperature T_m, this energy barrier is infinite. As the temperature T decreases further and further from T_m this energy barrier decreases until it reaches a point where nuclei form on a timescale of seconds to minutes. This is referred to as the homogeneous nucleation temperature T_H, however it is not a set thermodynamic parameter like T_m since it doesn't describe a change in state, only a temperature associated with a certain timescale for nucleation. This is discussed further later in the chapter.

The interfacial solid-liquid surface energy γ_e can be thought of as the excess energy stored in the interface between the two phases, characterizing the intermolecular forces between the liquid and the solid. In the case of water, temperature dependent ice-water interfacial surface energy values have been measured previously, showing a power law dependence on temperature given by equation (1.3).[15]

$$\lambda_e = \lambda_0 \left(\frac{T}{235.8}\right)^n \tag{1.3}$$

We can then define the number of particles in a critical radius as n_*, where d_0 is the effective diameter of one of the particles.

$$n_* = \frac{128\pi^3}{27} \frac{d_0^2 \gamma_e^3}{\Delta\mu^3} \tag{1.4}$$

Next, we can determine the nucleation rate from a Boltzmann type equation for J, for some preexponential factor.

$$J = A \exp\left(\frac{\Delta G_N}{k_B T}\right) \tag{1.5}$$

Now we just need to derive an expression for the preexponential term A. We can think of A as a product of the number density of nucleation sites ρ_s, the nuclei diffusion coefficient D_* (which gives the rate of nuclei moving over the boundary), and the probability Z that a critical nuclei will grow vs dissolve. The latter is the nonequilibrium Zeldovich factor, which derives from approximation of complex integrals regarding the kinetics of growing subnuclei.[16] For the purposes of these studies we will take these parameters at face value, although it should be noted that many other derivations exist for alternate representations of these parameters.

$$A = \rho_s D_* Z \tag{1.6}$$

$$D_* = \frac{i_* k_B T}{3\pi d_0^3 \eta} \tag{1.7}$$

$$Z = \sqrt{\frac{\Delta G_N / k_B T}{3\pi n_*}} = \frac{4R_*^2 \gamma_e}{9 k_B T n_*^2} \tag{1.8}$$

Where i_* is the number of particles on the surface of a critical nucleus and η is the dynamic viscosity of the supercooled liquid. Putting equations (1.5-1.8) together yields the nucleation rate derived from CNT.

$$J = \rho_s D_* Z \exp\left(\frac{\Delta G_N}{k_B T}\right) \tag{1.9}$$

1.2.1.2 *Heterogeneous and Surface Nucleation*

Deriving expressions for heterogeneous nucleation is much more difficult, with extensive work done on quantifying its various forms.[17] This type of nucleation relies on nucleation sites not intrinsic to the pure system. These would occur at boundaries between phases, such as surface nucleation; impurities in the solution, such as dust; and at physical boundaries, such as cracks in a vessel. Some attempts have been made to quantify heterogeneous nucleation, including a sister equation to equation (1.9).

$$J_{het} = \rho_{het} D_{het} Z_{het} \exp\left(\frac{\Delta G_{N_{het}}}{k_B T}\right) \tag{1.10}$$

This equation does little to elucidate the underlying mechanisms governing heterogeneous nucleation, as it is merely an application of the homogeneous nucleation equation with a simple relabel. Depending on the type of heterogeneous nucleation we may add term to equation (1.9) denoting the introduction of a set amount of nucleation sites to the system. Then we can express the total nucleation rate as the sum of the homogeneous and heterogeneous rates with equation (1.11).

$$J_{total} = J_{hom} + J_{het} \tag{1.11}$$

If we only consider the introduction of a constant number of nucleation N_{het} sites to the system, we may express the heterogeneous nucleation rate with the Dirac delta function $\delta(t)$, thus:

$$J_{het}(t) = N_{het}\delta(t) \tag{1.12}$$

Then when we integrate J_{het} over time we recover the number of nucleation sites added via heterogeneous nucleation. Measuring this value may be possible and is outlined in chapter 3. Alternate formulations of equation (1.12) are possible, if we allow growth of these heterogeneous nucleation sites to occur probabilistically relative to their remaining concentration, similar to a Michaelis-Menten-type equation.

1.2.2 *Growth*

Crystal growth dynamics are comprised of an incredibly complicated series of processes arising from a combination of diffusion phenomena and attachment-dissolution kinetics. To start, the growth rate of a crystal cannot be defined without some sort of length scale characteristic of the crystal itself. Oftentimes this may be a simple radius, but depending on the geometry of the crystal, some other length scale may be more applicable, such as hydrodynamic radius, radius of gyration, effective volume radius, etc. This implies that one cannot simply refer to the growth rate of a crystal alone, but it must be taken within some context of its shape. Let us, for ease of arithmetic, take a spherical crystal for example. Using the Gibbs relation, we can represent the free energy of formation ΔG_{cr} of new crystal as follows:

$$H = G + ST \tag{1.13}$$

Where H is the enthalpy, G is the Gibbs function, S is entropy, and T is temperature. By applying differentials to each side, we end up with:

$$\Delta G_{cr} = \Delta H - \Delta ST - S\Delta T \tag{1.14}$$

The driving force for crystal growth is the difference in free energy between the liquid and crystal phases ΔG_{cr}. By using the definition of entropy, equation (1.14) can be described in terms of the specific heats of the crystal and liquid phase, C_p^{cr} and C_p^{m}, melting enthalpy ΔH_m, melting temperature $\mathrm{T_m}$, and difference between the current temperature T and melting temperature, ΔT.[18]

$$\varDelta G = \frac{\varDelta H_m \varDelta T}{T_m} + \int_T^{T_m} (C_p^{cr} - C_p^{m}) dT + T \int_T^{T_m} (C_p^{cr} - C_p^{m}) \frac{dT}{T} \tag{1.15}$$

Using this free energy of formation, several expressions for the growth velocity has been proposed. Under the normal growth (NG) model for of crystallization for $\Delta T < 60$, equation (1.16), the growth velocity can be described as a function of temperature, melting temperature, viscosity η, and mean interatomic distance a_0. For larger supercooling, $90 < \Delta T < 160$, equation (1.17), the screw dislocation growth (SDG) model applies better.

$$u = \frac{k_B T}{3\pi a_0^2 \eta} \left(1 - \exp\left(-\frac{\varDelta G}{RT}\right)\right) \tag{1.16}$$

$$u = \frac{k_B T}{3\pi a_0^2 \eta} \frac{\Delta T}{2\pi T_m} \left(1 - \exp\left(-\frac{\varDelta G}{RT}\right)\right) \tag{1.17}$$

The preexponential term in equations (1.16) and (1.17) can be thought of as a velocity time scale: the diffusion coefficient, from the classic Stokes-Einstein relation, multiplied by a length scale of the system a_0, the average intermolecular distance.

1.2.3 *Melting and Freezing - The Stefan Problem*

Though there are many thermodynamic formulations of the crystal growth velocity, it is also helpful to represent the ideal system mathematically. The Stefan problem is a free-boundary problem which seeks to characterize the moving phase front for diffusion-limited growth via the heat equation PDE.[19] Consider the problem of phase change from a liquid to a solid in one-dimension, shown in Figure 1.3 below.

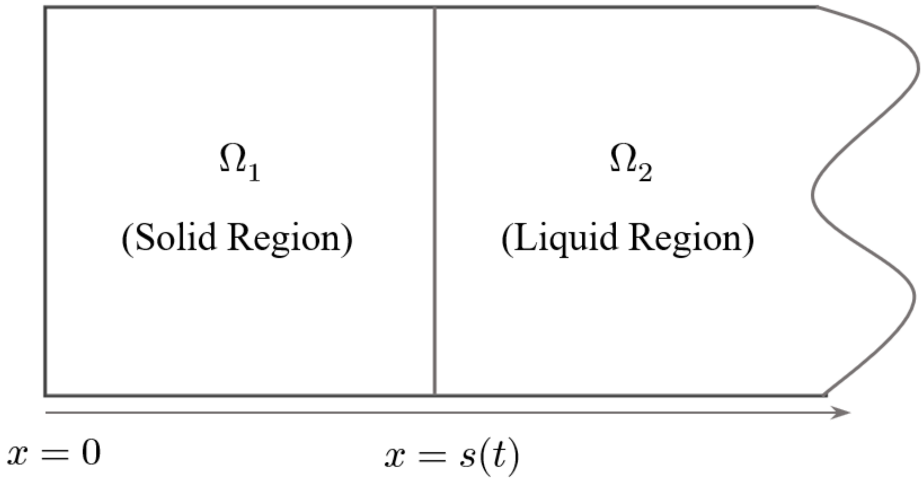

Figure 1.3. Stefan problem domain

Several assumptions are made for this problem. First, the domain is a semi-infinite block of liquid above the melting temperature $T = 0$. There is a fixed boundary at $x = 0$, with temperature $T(0, t) = 0$ at this boundary, and a moving boundary $s(t)$ which defines the separation between the liquid and solid phases. The solid portion of the boundary is considered at the constant temperature $T = 0$, while the liquid temperature is free. At the point $x = s(t)$ we impose a boundary condition having to do with the enthalpy of fusion of the material.

The solid region $0 \leq x \leq s(t)$

$$T(x, t) = 0 \tag{1.18}$$

The liquid region $s(t) \leq x \leq \infty$

$$\frac{\partial T}{\partial t} = \frac{k}{c_p \rho} \frac{\partial^2 T}{\partial x^2} \tag{1.19}$$

$$T(x,0) = f(x) \tag{1.20}$$

The moving boundary $x = s(t)$

$$-\Delta H_m \rho \frac{ds}{dt} = -k \frac{\partial T}{\partial x} \tag{1.21}$$

$$s(0) = 0 \tag{1.22}$$

$$T(s(t),t) = 0 \tag{1.23}$$

Equation (1.21) relates the heat of fusion given off by the phase change at the solidification line to the heat flux into the liquid. In this simplified model all the heat release associated with phase change is directed into the liquid region. In reality, it is more complex, with conduction through the solid region as well.

The general solution methods and general solutions to these types of problems are quite interesting, but not of importance here. For our purposes, we only care about the functional form of the growth velocity, which in this case would be $u(t) = \frac{ds}{dt}$. In this problem, we then have:

$$u(t) = \lambda \sqrt{\frac{k}{c_p \rho t}} \tag{1.18}$$

Where lambda is the transcendental number defined as follows:

$$\lambda e^{\lambda^2} \operatorname{erf}(\lambda) = \frac{St_L}{\sqrt{\pi}} \tag{1.19}$$

The dimensionless parameter St_L is the Stefan number and is specific to the setup of the problem. In this system, we have swapped the traditional locations of the liquid and solid region; however, if we consider the system as time reversed, the subsequent melting becomes freezing, and the velocity of the moving phase front remains the same. In general, this cannot be done, as there are fundamental differences between freezing and melting, but in this simplified picture it makes no difference.

In this picture, considering a simplified model of crystal growth via conduction driven phase change, we arrive at a time-dependent growth velocity, which is different than those posed in equations (1.16) and (1.17). This is partially due to the consideration of the heat released after phase change occurs, and also that this is a bulk velocity associated with non-isothermal temperature conditions within the substance. We could think about this velocity as the collective effects of different growth velocities of small regions of the liquid/solid that can be approximated as isothermal, at different temperatures throughout the domain of course.

1.2.4 *Shape*

The shapes of growing crystals range from the simple, such as spherical or rod like; to complex, such as dendritic or snowflake-like. For instance, Figure 1.4 shows the variety of crystal geometries for ice crystallization alone. One common method of characterizing the shapes of crystals is by defining their fractal dimension.[20] This is a measure of dimensionality of the crystal, which along with its hydrodynamic or effective radius, gives the shape information necessary to characterize the crystal. The shape of the crystal is intimately related to the growth rate, as it is impossible to characterize the growth rate without reference to some changing length scale. In the case of a crystal with some fractal dimension D and some effective radius r, we can describe the volume of the crystal with relation to these two quantities.

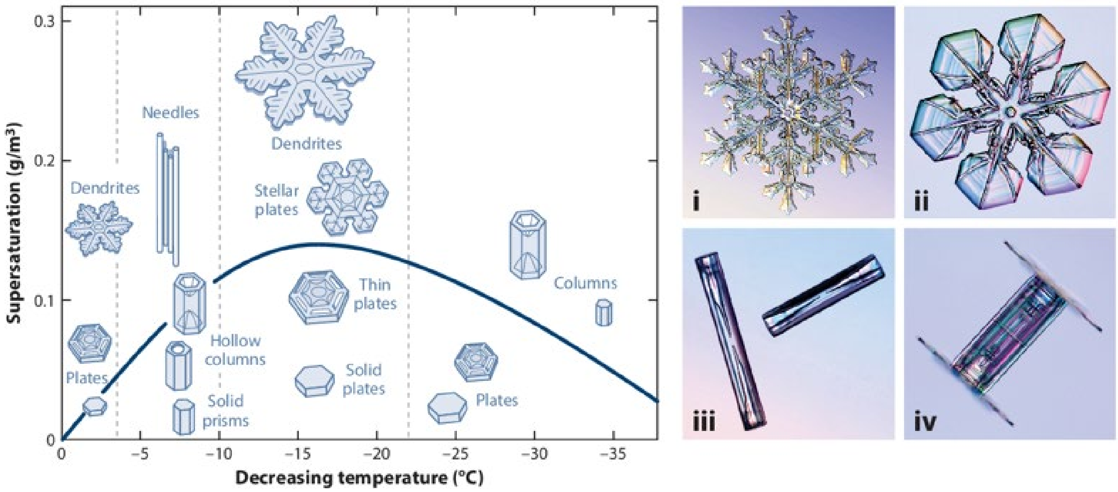

Figure 1.4. Formation of ice crystals from condensation of water vapor for various temperatures and supersaturations.[21]

$$V = Ar^{D} \tag{1.20}$$

Where A is some prefactor also relating to the crystal geometry. For instance, if we have a cubic crystal, then clearly $A = 1$ and $D = 3$, if we take r to be the width of the cubic crystal. In actual crystal networks, these values exist in some distribution, as crystals form stochastically. We can also relate the growth velocity $\frac{dr}{dt}$ to the other parameters by taking the derivative with respect to time of equation (1.20).

1.2.5 *Measurement of Nucleation rates, Growth rates, and Crystal Geometry*

In general, measurements of nucleation rates are quite difficult, as they typically rely on microscopy of very small volumes and directly counting nuclei, or in direct methods of characterization. The latter is almost exclusively used in systems where nucleation happens too quickly relative to imaging methods, if the system is sufficiently opaque, or if the new phase is difficult to distinguish from the progenitor phase.[22] Additional non-direct methods for measuring nucleation rates include optical techniques such as optical reflective measurements (ORM), laminar flow diffusion chambers, measurements of changes in electrical resistance, and calorimetric measurements.[23–25] These indirect measurements are dependent to varying degrees on models of how nucleation occurs in a system, often using classic CNT predictions. Molecular dynamics simulations also give insight into nucleation rates in systems simple enough to accurately model the molecular interactions.[26]

Measurement methods for crystal growth rates can also be broken down into direct and indirect methods. Direct methods involve imaging the growing crystal vs time and directly calculating the growth rate. This is clearly only possible in systems that one can isolate crystals in and get a clear image of the moving crystal front. Indirect methods include spectroscopic methods relating to changes in opacity or infrared light release, calorimetric methods relating heat release to growth, and population density methods tracking the changes in the size distribution.[27–29] Shape measurements are related to the growth rate measurements and can also be inferred from heat release curves and direct measurements. In chapter 3, we outline a method for extracting growth rates, dimensionality, and nucleation rates of transforming phase from calorimetric curves.

1.3 Cryopreservation

Cryopreservation is the storage of biological systems (cells, tissues, embryos, organs, etc.) at cryogenic temperatures (less than -100 °C).[30] At these temperatures, the metabolic processes normally associated with life and death slow down by many orders of magnitude, thus allowing for the storage of these systems for extended periods of time.[31,32] Proper cryopreservation, insofar that the biological sample isn't destroyed or heavily damaged upon rewarming, involves the mitigation of ice formation, ideally to the extracellular space (in the case of slow freezing) or altogether (in the case of vitrification). Water alone freezes far too rapidly to maintain cell viability during cooling and warming.[33] To compensate, special chemicals called cryoprotective agents (CPA) help to minimize ice formation by modulating the ice growth and nucleation rates, glass transition temperature, melting temperature, and viscosity of the system (see Figure 1.5).[34] Along with CPAs, engineering cooling and warming rates tailored to specific systems is also an integral part of cryopreservation. For example, systems that do not tolerate ice formation nor high-concentration CPAs require rapid cooling rates and ultrarapid warming rates to avoid ice formation. On the other hand, systems that have high toxicity thresholds may be more suitable for high concentration CPA, slow-freezing approaches. There exists a variety of cooling and warming techniques used throughout the field.

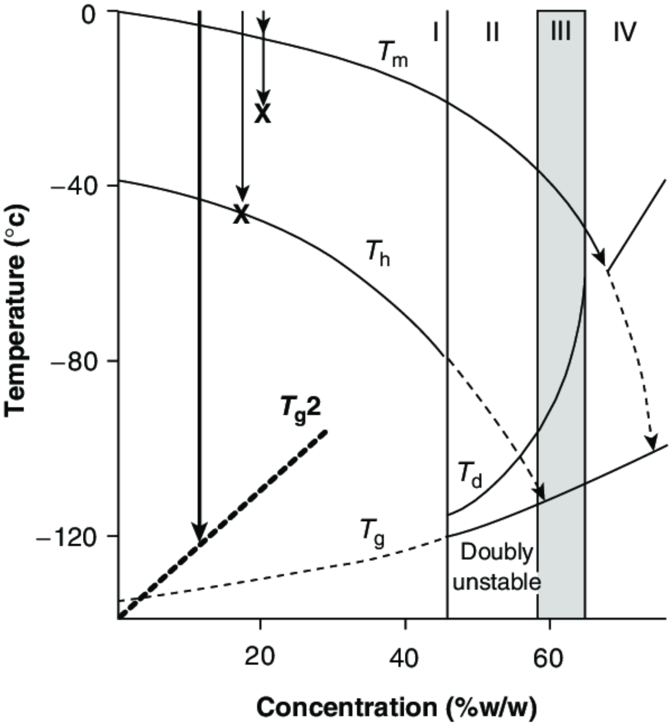

Figure 1.5. A non-equilibrium phase diagram for a hypothetical cryoprotectant. Notice the concentration dependence of melting temperature, nucleation rate, and glass transition temperature. The "danger zone" can be seen between the homogeneous nucleation temperature and glass transition temperature, where ice formation is most rapid.[35]

1.3.1 *Cryoprotectants*

CPAs are chemicals that aid in the process of cryopreservation through a variety of mechanisms. There are several different groups of CPAs that have different mechanisms of action, summarized in Table 1.2. These consist of alcohols, glycols, sugars, sulfides, amides, polymers, and CPA cocktails. Omitted from this tables are the more exotic forms of cryoprotectants, such as ice recrystallization inhibitors, which act to limit size and formation of ice crystals. Examples of these include antifreeze proteins and glycoproteins, which have shown promising potential to inhibit ice growth even at miniscule concentrations.[36]

Table 1.2. A list of common cryoprotectants.[34]

Alcohols and Glycols	Sugars	Sulfides and Amides	Polymers	Cocktails[37]
Propylene glycol (PG)	Sucrose	Formamide	Polyethylene glycol (PEG)	VS55
Ethylene glycol (EG)	Trehalose	Dimethyl sulfoxide (DMSO)	Polyvinyl pyrrolidone (PVP)	DP6
Glycerol	Glucose	Dimethyl	Dextrans	M22
Ethanol	Lactose	Formamide	Serum proteins	
Methanol		Acetamide	Milk proteins	

An additional method of characterizing CPAs is methodologically, that is, how they work in practice. When considering a system undergoing cryopreservation, the CPAs can be classified as either penetrating or nonpenetrating. Nonpenetrating CPAs work by increasing the solute concentration outside of the cell, which causes water to leave the cells to the minimize the chemical potential gradient. The “pulling” of water out of the cells via nonpenetrating cryoprotectants decreases the freezable fraction of the interior of the cell as well as raises the concentration of both exogeneous and intrinsic cryoprotectants. Sugars typically act as nonpenetrating cryoprotectant as they are too bulky to cross the cell membrane. Penetrating cryoprotectants, such as glycols and alcohols, easily pass through a variety of cell membranes and cause a characteristic “shrink-swell” effect. When a cell is introduced to a penetrating CPA, it first undergoes an abrupt shrinkage due to water transport out of the cell. Following this shrinkage, CPA around the cell flows back into the cell as the membrane is less permeable to the CPA than water. Ultimately, the final concentration of CPA in the cell determines how readily ice will form, with higher concentrations of CPA making ice formation more difficult.

The formation of ice within a CPA loaded system is a function of CPA concentration, temperature, and time. For example, in high concentration CPA loaded systems, ice forms slowly enough so that the system may be brought to the glass transition temperature slowly, whereas with low concentration CPAs the system only has a small amount of time to reach the glass transition temperature without appreciable ice formation. The rates necessary to bring a CPA, or any system, form its melting point to its glass transition temperature is the critical cooling rate (CCR). Likewise, the rate required to bring the system from the glass transition to the melting temperature without ice formation is the critical warming rate (CWR). In reality, there will always be some ice that forms in a system; however, ice fractions of less than .002 are considered "effectively vitrified", though there is debate on the significance or relevance of this particular fraction. In other cases, especially those where quantitative ice fraction measurements are difficult or impossible, qualitative measurements may be used to indicate CCR and CWR, such as opacity or XRD which have limits of detection of roughly .01, though this may change based on the uniformity or nonuniformity of the ice formation i.e., one large crystal or many microcrystals. Measurement of CCR and CWR is addressed further in chapters 4 and 5, with theoretical predictions in chapters 2 and 3.

1.3.2 *Mechanisms of damage*

Understanding the mechanisms of cell damage and death during the cryopreservation process is necessary to engineer better protocols and achieve more favorable outcomes. The death mechanisms can be separated into four categories, summarized in Figure 1.6. First is osmotic shock, which occurs due to the rapid and extreme changes in cell volume when cells are exposed to high osmotic gradients, such as high concentrations of CPA. These large changes in volume can cause physical damage to the cell membrane and structures within the cell, but also lead to large changes in internal cell constitution. For example, the large decrease in intercellular water concentration leads to large changes in pH and disruptions in the hydrogen bonding necessary to facilitate normal cell processes. A whole laundry list of other proposed death mechanisms of these "solute effects" or "solution effects" have been proposed but are difficult to verify quantitatively.

The CPAs themselves are also often cytotoxic, that is, they result in toxication of the cell, which seems to be cell-specific and is poorly understood. Due to the nature of cell behavior in the presence of CPA, along with uncertainties about internal CPA concentrations, it is difficult to determine the mechanisms of death, especially solute effects vs cytotoxicity, which may share some characteristics. Chilling and cold injury also is difficult to quantify but leads to measurable reductions in viability in many systems. For example, warm water aquatic species, such as zebrafish, will die if they experience excessive cooling while in the embryonic stage. Changes in temperature may lead to changes in metabolic activity that leads to injury in the cells. The final mechanism for cell injury and death during cryopreservation is intracellular ice formation, where ice forms directly inside the cell. This can cause mechanical damage to the cell membrane and internal structures of the cell due to the expansion of ice and crystals propagating across important structures. Additionally, ice formation is associated with the loss of liquid water in the cell, causing increases concentration of internal species, leading to changes in pH among other things associated with both osmotic intolerance and CPA cytotoxicity. Interestingly, some of these injury mechanisms can be leveraged to minimize the effects of other injury mechanisms. For example, the associated changes in metabolic activity following decreases in cell temperature are useful when loading a system with CPA, as the CPAs toxic effects take more time to propagate throughout the cell than at lower temperatures. Stepwise loading can also be implemented to mitigate the damages associated with the volume changes and osmotic gradients during CPA loading.

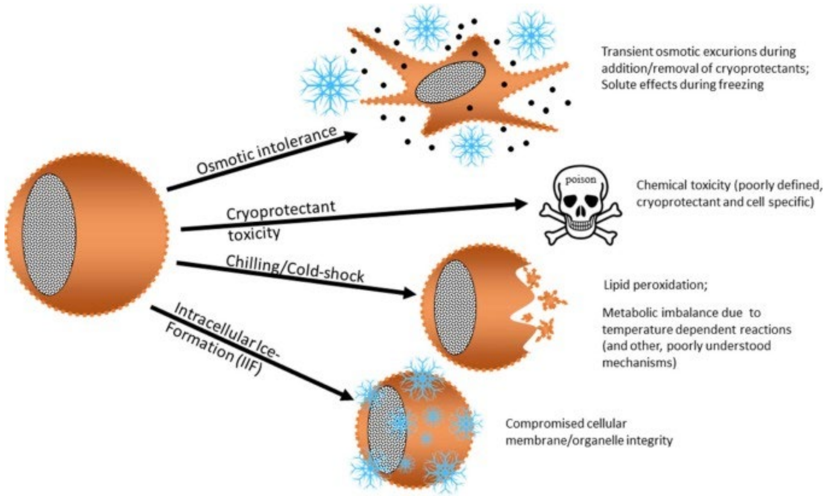

Figure 1.6. Shows the various death mechanisms during the cryopreservation process.[38]

1.3.3 *Cooling and Warming Techniques*

Since many cell and tissue types can only tolerant certain concentrations CPA, or certain levels of ice formation, choosing the proper cooling and warming rate for each system is important. Ideally, we would like to instantaneously change the temperature of the system uniformly throughout the sample; however, we are limited by the speed of conduction on cooling, making this a mere pipe dream. The only currently viable method for cooling a system is via convective cooling. This means placing the sample in an environment at cryogenic temperatures or perfusing cold solution through the sample. Typically for small samples, this is achieved via direct quenching into liquid nitrogen or some other cryogenic fluid. This can result in cooling rates anywhere from 100-100,000 ℃/min for samples ranging from .1 µL to 1 mL samples.[39] Placement of samples onto pre-chilled substrates has also been shown to be a viable alternative to direct quenching. In this method, a substrate with high thermal mass and high thermal conductivity (typically copper) is equilibrated to liquid nitrogen temperature. Next, the specimen is placed on the chilled copper and is rapidly cooled. This is advantageous for some systems, as certain materials (especially those with larger thermal mass) induce boiling of the liquid nitrogen on contact—the so-called Leidenfrost Effect. This causes a vapor layer to form between the sample and the liquid nitrogen, rapidly decreasing the cooling rate. For larger samples (>1 μL), thermal gradients are so large that they may induce cracking during direct quenching into liquid nitrogen, and thus require lower heat transfer coefficient convective cooling such as a controlled-rate freezer. One advantage of this is that the system can be cooled in a stepwise fashion, minimizing thermal gradients that can lead to damaging crack formation; however, cooling rates are quite slow (~1℃/min). Unfortunately, all these cooling methods ultimately rely on convective cooling and are thus cooling from the outside in, necessitating the existence of thermal gradients. As of the writing of this thesis, the only known volumetric cooling method is magnetic refrigeration, but is limited to small changes in temperature of a degree or two. A summary of the current cooling and warming methods used in cryopreservation are shown in Table 1.3.

Table 1.3. A table summarizing the current methods for cooling and warming used in cryopreservation.

Cooling		**Warming**	
Convective (sample size dependent)	Volumetric	Convective (sample size dependent)	Volumetric
Liquid nitrogen quenching (10^3-10^5 C/min)	Magnetic refrigeration (uncharacterized)	Warm water quenching (10^3-10^5 C/min)	IR Lamp (3,000-20,000℃/min)
Contact cooling (10^3-10^5 C/min)		Joule heating (10^4-10^8 C/min)	Laser nanowarming (10^4-10^9 C/min)
Air/gas cooling (<1 C/min)		Laser nanowarming (exterior nanoparticles) (10^4-10^7 C/min)	RF nanowarming (1-100 C/min)

Similar to cooling, warming can also be carried out convectively, typically in a bath of room temperature to warm liquid that is conducive to sample survival, with warming rates similar to cooling rates via direct quenching. Additionally, these warming baths may contain solutes so that the newly warmed sample doesn't experience the damages associated with osmotic shock. An additional convective warming method is the joule-heating method, whereby the cryopreserved sample is placed on a substrate and the substrate is warmed via electrical-resistive heating. This can achieve rapid warming rates in excess of 1,000,000 ℃/min.[40] Unlike cooling, there exists several volumetric warming approaches. The first and most simple is simple infrared warming, whereby the sample is placed under a high-powered infrared lamp and heating via photon absorption and achieving warming rates of 3,000-20,000 ℃/min.[41] For small systems that require ultra-rapid warming rates due to low CPA concentration, laser nanowarming is a viable method for rewarming. Nanoparticles tuned to the laser frequency are introduced to the specimen's environment, either inside or outside of the specimen. When the laser fires, the nanoparticles undergo plasmonic heating and rapidly rewarm the sample. In the case volumetric warming, when the nanoparticles are inside the specimen, warming rates in excess of 10,000,000 ℃/min can be attained. For exterior nanoparticles, the size of the specimen dictates the warming rate, with rates typically ranging from 10,000-1,000,000 ℃/min. The final volumetric warming method is radio frequency (RF) warming. In this method, magnetic nanoparticles within the system are heated by a high-powered alternating magnetic field. This allows for uniform and relatively fast warming (up to 100 ℃/min) given the size of the system and concentration of nanoparticles.[42,43]

Chapter 2

The Kinetics of Nonisothermal Phase Change

2.1 Introduction

A mathematical description of isothermal crystallization kinetics, or kinetics of phase transformation more generally, was first derived by Kolmogorov in 1937[44], then popularized by Avrami in a series of papers on the kinetics of phase change several years later.[45–47] The key equation, the Avrami equation, describes how the fraction of transformed phase changes with time given a constant growth and nucleation rate. The use of this equation is ubiquitous in the study of phase change; however, it is often misused by being applied to nonisothermal systems. Many attempts have been made to arrive at a general equation relating fraction transformed, nucleation rate, and growth rate for non-isothermal processes, yet none do so in a robust manner, with many efforts fabricating arbitrary constants and parameters.[48–51] Additionally, the question of how to account for initial distributions of the nucleated phase remains; this is also lacking in a general nonisothermal picture of phase change.

In this chapter, we describe a generalized approach to evaluate nonisothermal phase change by relating the nucleation rate, growth rate, and transformed fraction in an ordinary differential equation. This equation can be derived from first principles by first taking a geometric picture of nucleation and growth, then by examining phase change in Fourier space, where we find that a clear description arises between the nucleation rate, growth rate, and transformed fraction. We subsequently present an analytic solution to the traditional population balance partial differential equation for nucleating systems which describes how the size distribution of phase changes with time. By equating the analytic solution to the PDE with the differential equation, we are able to derive the ODE initial conditions, which capture the effects of the initial distribution of phase, completing the description of nonisothermal phase change. We then use this model, along with classical nucleation theory, to predict the critical cooling rate of pure water to surprising accuracy.

2.2 Nonisothermal Phase Transformation

2.2.1 *Transformed Fraction and the Extended Volume*

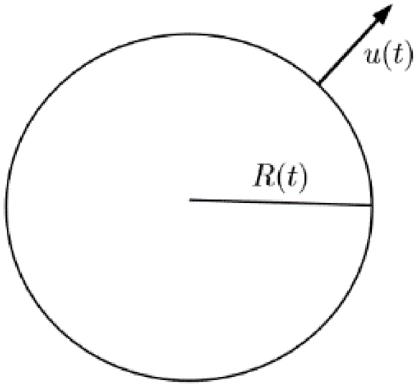

Figure 2.1. A diagram showing the geometry of a symmetrically growing crystal.

This derivation relies on some key assumptions about the phase change process, mainly, that there exists temperature dependent properties u and J, which represent the crystal growth velocity and nucleation rate respectively, and that these are strictly positive and smooth functions of temperature. Consider ice crystallization in water, or in any applicable liquid, being cooled from its melting point T_m for some time t at rate $\dot{T} = T(t)$. Then for a crystal nucleated at time $t_0 = 0$, its radius R (assuming spherical growth) is:

$$R(t) = \int_0^t u(T(t))dt \tag{2.1}$$

Equation (2.1) describes the growing radius of a symmetrically growing crystal depicted in Figure 2.1. Since crystals can nucleate at any time, we must modify equation (2.1) to include the time at nucleation, giving us a crystal radius that is a function of the global time t and the time at nucleation t_i. Since temperature is ultimately a function of time, we can omit it and simply state $u(T(t))$ as $u(t)$.

$$R(t, t_i) = \int_{t_i}^t u(t)dt \tag{2.2}$$

Equation (2.2) now describes the radius of a crystal at time t that was nucleated at time t_i, given the time dependent growth velocity $u(t)$. We will now consider a small interval around time $t = t_i$, expressed as dt_i. Then, given a nucleation rate of $J(t_i)$ and volume of V_0, we can express the number of nuclei formed $N(dt_i)$ at time t_i in the time interval dt_i, given a spatial volume of V_0 and a nucleation rate of $J(t_i)$ as:

$$N(dt_i) = J(t_i)V_0 dt_i \tag{2.3}$$

From equation (2.3), we can then express the volume V_i of the crystals formed at time t_i in the time interval dt_i as:

$$V_i(t_i) = \frac{4}{3}\pi R^3(t, t_i)N(dt_i) = \frac{4}{3}\pi R^3(t, t_i)J(t_i)V_0 dt_i \tag{2.4}$$

We now introduce the concept of the extended volume V_e, which is the total volume of all the crystals formed disregarding overlap.

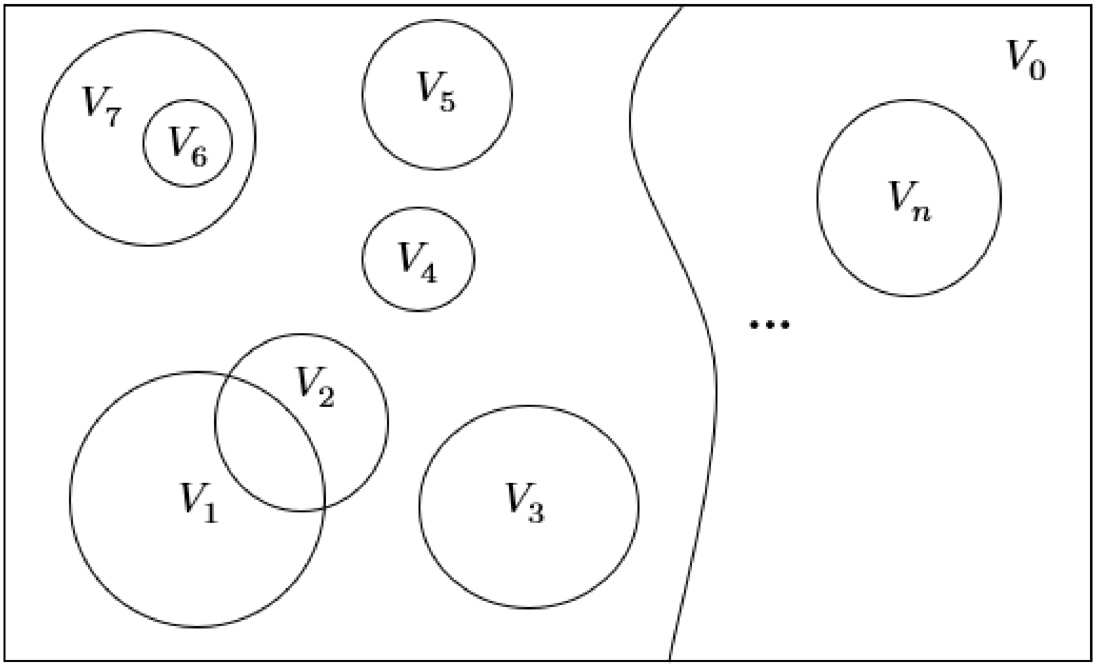

Figure 2.2. Extended volume and overlap of sub-volumes in a large domain.

We can calculate V_e by integrating equation (2.4) over all start times t_i. Thus:

$$V_e(t) = \frac{4}{3}\pi \int_0^t R^3(t, t_i) J(t_i) V_0 dt_i \tag{2.5}$$

We now have an expression for extended volume in terms of the nucleation rate and radii distribution of the growing crystals. As we are concerned with nucleation and growth rates during phase change, there is a problem with calculating the transformed fraction, i.e., the fraction which has undergone phase change. Given perfect knowledge of both nucleation and growth rates, we still have to deal with overlap between growing regions of transformed phase arising as phase change occurs. To compensate for this overlap, we consider a finite but large space V_0 divided into two sections, a transformed section with volume $V_0 f$ and an untransformed section with volume $V_0(1-f)$, where f is the transformed fraction of the volume. Inside V_0 there is a randomly distributed collection of n sub-volumes $V_1, V_2, \dots V_n$ with $V_i \ll V_0, \forall i \in \{1,2, \dots n\}$. Given the definition of f, we can then express the probability that a randomly chosen point in V_0 lies in the untransformed region as $1 - f$. This is equivalent to the probability of the point not lying in each transformed region, thus:

$$1 - f = \left(1 - \frac{V_1}{V_0}\right)\left(1 - \frac{V_2}{V_0}\right)...\left(1 - \frac{V_n}{V_0}\right) = \prod_{i=1}^{n}\left(1 - \frac{V_i}{V_0}\right) \tag{2.6}$$

We can then take the natural logarithm of each side and get

$$\ln(1 - f) = \sum_{i=1}^{n} \ln\left(1 - \frac{V_i}{V_0}\right) \tag{2.7}$$

Since $V_i \ll V_0$ for all i, we can use the Taylor expansion of the natural logarithm to arrive at

$$\ln(1 - f) = -\sum_{i=1}^{n} \frac{V_i}{V_0} + O\left(\frac{V_i^2}{V_0^2}\right) \tag{2.8}$$

We then approximate each V_i as $\frac{V_e}{n}$ in each error term, and note that the extended volume is the sum of all the sub volumes, we can write an expression relating the transformed fraction to the extended volume:

$$V_e = \sum_{i=1}^{n} V_i \tag{2.9}$$

$$f = 1 - \exp\left(-\frac{V_e}{V_0} + O\left(\frac{1}{n}\frac{V_e^2}{V_0^2}\right)\right) \tag{2.10}$$

We can now use this expression to arrive at a length scale L_0 for validity for the following analysis. For isothermal, spherical growth of the transformed phase, defined by the Avrami equation, we have:

$$V_e(t) = \frac{4\pi}{3} V_0 J u^3 t^4 \tag{2.11}$$

$$N = V_0 J t \tag{2.12}$$

where $u(t)$ (ms^{-1}) is the growth velocity and $J(t)$ $(m^{-3}s^{-1})$ is the nucleation rate. We can identify instances where the higher order terms of equation (2.10) are negligible. We assume this term is negligible if it is less than one part in X the lower order term.

$$\frac{V_e}{V_0} \sim \frac{1}{XN}\frac{V_e^2}{V_0^2} \tag{2.13}$$

$$V_0 \sim \frac{4\pi}{3X}u^3t^3 \tag{2.14}$$

$$L_0 \approx V_0^{\frac{1}{3}} \sim \frac{1.61}{X^{\frac{1}{3}}}ut \tag{2.15}$$

Using a 1% criterion ($X = 100$) shows that the higher order term is only significant over extremely short length scales.

Now, assuming time (i.e., temperature) dependent growth velocities and nucleation rates, but negligible spatial variation in temperature we can relate the extended volume of phase $V_e(t)$, that is, the total volume of all the spheres of phase at that time disregarding overlap, to the fraction of transformed phase.

$$f(t) = 1 - \exp\left(-\frac{V_e(t)}{V_0}\right) \tag{2.16}$$

2.2.2 *Generalized Non-Isothermal Avrami (GNA) Equation*

Recall, equation (2.5) and combine it with equation (2.16) and we have

$$\ln\big(1 - f(t)\big) = \frac{4\pi}{3}\int_0^t J(t_i)R^3(t, t_i)dt_i \tag{2.17}$$

We can express $R(t, t_i)$ in terms of the antiderivative of the velocity $\boldsymbol{u(t)}$, $\boldsymbol{U(t)}$

$$R(t, t_i) = \int_{t_i}^{t} u(\tau)d\tau = U(t) - U(t_i) \tag{2.18}$$

Then, by taking the derivative of equation (2.17) with respect to time we get

$$\frac{1}{f-1}\frac{df}{dt}=\frac{\partial}{\partial t}\left(\frac{4\pi}{3}\int_0^t J(t_i)R(t,t_i)dt_i\right) \tag{2.19}$$

$$\frac{1}{f-1}\frac{df}{dt}=\frac{4\pi}{3}\int_0^t J(t_i)\frac{\partial}{\partial t}R^3(t,t_i)dt_i+\frac{4\pi}{3}J(t)R(t,t) \tag{2.20}$$

Note that

$$R(t,t)=\int_t^t u(\tau)d\tau=0 \tag{2.21}$$

Thus,

$$\frac{1}{f-1}\frac{df}{dt}=\frac{4\pi}{3}\int_0^t J(t_i)\frac{\partial}{\partial t}R^3(t,t_i)dt_i \tag{2.22}$$

$$\frac{\partial}{\partial t}R^3(t,t_i)=\frac{\partial}{\partial t}\big(U(t)-U(t_i)\big)^3=3\big(U(t)-U(t_i)\big)^2u(t) \tag{2.23}$$

$$\frac{1}{f-1}\frac{df}{dt}=4\pi\int_0^t J(\tau)\big(U(t)-U(t_i)\big)^2u(t)dt_i \tag{2.24}$$

$$\frac{1}{f-1}\frac{df}{dt}=4\pi\int_0^t J(t_i)u(t)U^2(t)dt_i-8\pi\int_0^t J(t_i)u(t)U(t_i)U(t)dt_i+4\pi\int_0^t J(t_i)u(t)U^2(t_i)dt_i \tag{2.25}$$

By denoting the antiderivative of $J(t)$ as $J^i(t)$ we have

$$\frac{1}{f-1}\frac{df}{dt}=4\pi u(t)U^2(t)J^i(t)-8\pi u(t)U(t)\int_0^t J(t_i)U(t_i)dt_i+4\pi u(t)\int_0^t J(t_i)U^2(t_i)dt_i \tag{2.26}$$

We can then pull out a factor of $4\pi u(t)$ yields

$$\frac{1}{f-1}\frac{df}{dt}\frac{1}{4\pi u(t)}=U^2(t)J^i(t)-2U(t)\int_0^t J(t_i)U(t_i)dt_i+\int_0^t J(t_i)U^2(t_i)dt_i \tag{2.27}$$

Taking the derivative of both sides with respect to time again yields

$$\frac{d}{dt}\left[\frac{1}{4\pi u(t)}\frac{1}{f-1}\frac{df}{dt}\right]=\frac{d}{dt}\Big(U^2(t)J^i(t)\Big)-\frac{d}{dt}\left(2U(t)\int_0^t J(t_i)U(t_i)dt_i\right)+J(t)U^2(t) \tag{2.28}$$

$$\frac{d}{dt}\left[\frac{1}{4\pi u(t)}\frac{1}{f-1}\frac{df}{dt}\right]=2U(t)u(t)J^i(t)+U^2(t)J(t)-2U^2(t)J(t)-2u(t)\int_0^t J(t_i)U(t_i)dt_i+J(t)U^2(t) \tag{2.29}$$

$$\frac{d}{dt}\left[\frac{1}{4\pi u(t)}\frac{1}{f-1}\frac{df}{dt}\right]=2U(t)u(t)J^i(t)-2u(t)\int_0^t J(t_i)U(t_i)dt_i \tag{2.30}$$

$$\frac{1}{2u(t)}\frac{d}{dt}\left[\frac{1}{4\pi u(t)}\frac{1}{f-1}\frac{df}{dt}\right] = U(t)J^{i}(t) - \int_0^t J(t_i)U(t_i)dt_i \tag{2.31}$$

We can take the derivative with respect to time, yielding

$$\frac{1}{2u(t)}\frac{d}{dt}\left[\frac{1}{4\pi u(t)}\frac{1}{f-1}\frac{df}{dt}\right] = u(t)J^{1}(t) + U(t)J(t) - J(t)U(t) = u(t)J^{1}(t) \tag{2.32}$$

Finally, we can divide both sides by $u(t)$ and then take the derivative with respect to time one last time and get

$$J(t) = \frac{1}{8\pi}\frac{d}{dt}\left[\frac{1}{u(t)}\frac{d}{dt}\left[\frac{1}{u(t)}\frac{d}{dt}\left[\frac{1}{f-1}\frac{df}{dt}\frac{1}{u(t)}\right]\right]\right] \tag{2.33}$$

Equation (2.33) is a general ordinary differential equation for either the fraction of nucleated phase or the growth rate, linked to the nucleation rate. This equation applies for arbitrary evolution of temperature with time. We refer to this as the General Nonisothermal Avrami Equation (GNA Equation). If we allow for $J(t)$ and $\boldsymbol{u(t)}$ to be constant functions of time, in other words isothermal temperature conditions, we have

$$\frac{1}{8\pi u^3}\frac{d^4}{dt^4}(-\ln(1-f)) = J \tag{2.34}$$

Solving this, for initial conditions of zero, we get

$$f(t) = 1 - \exp\left(-\frac{\pi}{3}u^3Jt^4\right) \tag{2.35}$$

Which is precisely the Avrami equation for uniform, constant spherical growth. Now the question arises, what are the initial conditions for this system?

2.2.3 *General relation between transformed fraction, nucleation rate, and growth velocity*

In this section we will extend the differential equation (2.33) into an arbitrary number of dimensions and growth geometries by looking at phase change in Fourier space. Recall equations (2.17) and (2.18), we then have

$$\ln\bigl(1-f(t)\bigr) = \frac{4\pi}{3}\int_0^t J(t_i)R^3(t,t_i)dt_i \tag{2.36}$$

Now consider the velocity $\boldsymbol{u(t)}$ to have radial dependence. Then

$$u(t) = \frac{dR}{dt} = \frac{v(t)}{R^m} \tag{2.37}$$

Integrating both sides from t_i to $\boldsymbol{t}$ gives us the following, with $\boldsymbol{V}$ as the antiderivative of $\boldsymbol{v}$

$$\frac{R^{m+1}}{m+1} + \frac{R_0^{m+1}}{m+1} = V(t) - V(t_i) \tag{2.38}$$

Since $R_0 \ll R$ for almost all $\boldsymbol{t}$, then

$$R(t, t_i) = \Big((m+1)\big(V(t) - V(t_i)\big)\Big)^{\frac{1}{m+1}} \tag{2.39}$$

Since the crystal grows uniformly, it grows with the volume of an n-ball. That is, in two dimensions it grows with flat-circular growth, in three dimensions with spherical growth, and so on. In higher dimensions, the nucleating species may be something more abstract, like nucleation and growth through information networks. In this case, equation (2.36) is transformed into the following, with m and D as the growth geometry parameter and dimensionality of the phase change respectively. $\pi^{\frac{D}{2}}/\Gamma(\frac{D}{2}+1)$ is the volume scaling term for an n-ball, and Γ is the gamma function.

$$-\ln\big(1 - f(t)\big) = \frac{\pi^{\frac{D}{2}}}{\Gamma\left(\frac{D}{2}+1\right)} \int_0^t J(t_i)\,\Big((m+1)\big(V(t) - V(t_i)\big)\Big)^{\frac{D}{m+1}} dt_i \tag{2.40}$$

$$-\ln\big(1 - f(t)\big) = \alpha \int_0^t J(t_i)\big(V(t) - V(t_i)\big)^{\frac{D}{m+1}} dt_i \tag{2.41}$$

$$\alpha = \frac{\pi^{\frac{D}{2}}(m+1)}{\Gamma\left(\frac{D}{2}+1\right)} \tag{2.42}$$

By applying the substitutions $y = V(t)$, $z = V(t_i)$, and $dz = v(t_i)dt_i$, we transform equation (2.41) into

$$-\ln\big(1 - f(t)\big) = \alpha \int_0^t \frac{J\Big(U^{-1}(z)\Big)}{v\big(V^{-1}(z)\big)} (y - z)^{\frac{D}{m+1}} dz \tag{2.43}$$

Making one further substitution of $w = y - z$, we get

$$-\ln\bigl(1-f(t)\bigr) = -\alpha \int_{y}^{y-U(t)} \frac{J(U^{-1}(y-w))}{v(U^{-1}(y-w))} w^{\frac{D}{m+1}} dw \tag{2.44}$$

$$-\ln\bigl(1-f(t)\bigr) = \alpha \int_{0}^{y} \frac{J(U^{-1}(y-w))}{v(U^{-1}(y-w))} w^{\frac{D}{m+1}} dw \tag{2.45}$$

$$-\ln\bigl(1-f(t)\bigr) = \alpha \int_{0}^{\infty} \theta(y-w) \frac{J(U^{-1}(y-w))}{v(U^{-1}(y-w))} w^{\frac{D}{m+1}} dw \tag{2.46}$$

Where θ is the Heaviside step function. This may at first seem like a useless complication of what we had earlier, but if one makes the following substitutions

$$F(y) = -\ln\left(1 - f\bigl(U^{-1}(y)\bigr)\right) \tag{2.47}$$

$$P(y) = \frac{J\bigl(U^{-1}(y)\bigr)}{u\bigl(U^{-1}(y)\bigr)} \tag{2.48}$$

$$G(y) = \theta(y)\alpha y^{\frac{D}{m+1}} = \theta(y) \frac{\pi^{\frac{D}{2}}(m+1)}{\Gamma\left(\frac{D}{2}+1\right)} y^{\frac{D}{m+1}} \tag{2.49}$$

Then equation (2.46) can be rewritten as,

$$F(y) = \int_{0}^{\infty} P(z)G(y-z)dz \tag{2.50}$$

Where F, P, and G all have values of zero for $y < 0$. This permits us to write a relation between these three functions with the convolution operator $(*)$.

$$F(y) = (P * G)(y) \tag{2.51}$$

We see that $G(y)$ is the volume of a growing sphere of the newly transformed phase and $P(y)$ is the phase size distribution at that radius. As is often the case, relationships involving the convolution operator are more easily interpreted in Fourier space. Applying the Fourier transform, denoted $\mathcal{F}(F) = \hat{F}$, to equation (2.51) yields

$$\hat{F} = \hat{G}\hat{P} \tag{2.52}$$

$$\hat{G} = \frac{\hat{F}}{\hat{P}} \tag{2.53}$$

$$G(y) = \left(F * \mathcal{F}^{-1}\left(\frac{1}{\hat{P}}\right)\right)(y) \tag{2.54}$$

$$\hat{P} \ = \alpha \int_{-\infty}^{\infty} \theta(y) y^{\frac{D}{m+1}} \exp(-2\pi i y \xi)\, dy \tag{2.55}$$

Invoking the derivative property of the Fourier transform we get letting $\frac{D}{m+1} = a$,

$$\hat{P} = \alpha \left(\frac{i}{2\pi}\right)^{a} \frac{d^{a}}{d\xi^{a}} \mathcal{F}\{\ \theta(y)\} = \left(\frac{i}{2\pi}\right)^{a} \frac{d^{a}}{d\xi^{a}} \left(\frac{1}{2}\left(\frac{1}{i\pi\xi} + \delta(\xi)\right)\right) \tag{2.56}$$

$$\hat{P} = \alpha \left(\frac{i}{2\pi}\right)^{a} \frac{d^{a}}{d\xi^{a}} \mathcal{F}\{\ \theta(y)\} = \left(\frac{i}{2\pi}\right)^{a} \frac{1}{2i\pi} i^{2a} \frac{\Gamma(1+a)}{\xi^{1+a}} \ + \left(\frac{i}{2\pi}\right)^{a} \frac{1}{2} \frac{d^{a}\delta(\xi)}{d\xi^{a}} \tag{2.57}$$

$$\hat{P} = \alpha \frac{i^{3(a+1)}}{(2\pi)^{1+a}} \frac{\Gamma(1+a)}{\xi^{1+a}} \ + \alpha \left(\frac{i}{2\pi}\right)^{a} \frac{1}{2} \frac{d^{a}\delta(\xi)}{d\xi^{a}} \tag{2.58}$$

$$\frac{1}{\hat{P}} = \frac{1}{\alpha} \frac{1}{\frac{i^{3(a+1)}}{(2\pi)^{1+a}} \frac{\Gamma(1+a)}{\xi^{1+a}} \ + \left(\frac{i}{2\pi}\right)^{a} \frac{1}{2} \frac{d^{a}\delta(\xi)}{d\xi^{a}}} \tag{2.59}$$

$$\frac{1}{\hat{P}} = \frac{1}{\alpha} \frac{\frac{(2\pi i\xi)^{1+a}}{i^{4a}\varGamma(1+a)}}{1 \ + \frac{(2\pi i\xi)^{1+a}}{i^{4a}\Gamma(1+a)} \ \left(\frac{i}{2\pi}\right)^{a} \frac{1}{2} \frac{d^{a}\delta(\xi)}{d\xi^{a}}} \tag{2.60}$$

Then inserting equation (2.60) into equation (2.54) we get

$$\hat{G} = \frac{1}{\alpha} \frac{\hat{F}}{i^{4a}\Gamma(1+a)} (2\pi i\xi)^{1+a} \frac{1}{1 \ + \frac{(2\pi i\xi)^{1+a}}{i^{4a}\Gamma(1+a)} \ \left(\frac{i}{2\pi}\right)^{a} \frac{1}{2} \frac{d^{a}\delta(\xi)}{d\xi^{a}}} \tag{2.61}$$

$$G(y) = \frac{1}{\alpha} \frac{1}{i^{4a}\Gamma(1+a)} \frac{d^{1+a}}{dy^{1+a}} F(y) * \mathcal{F}^{-1} \left\{ \frac{1}{1 \ + \frac{(2\pi i\xi)^{1+a}}{i^{4a}\Gamma(1+a)} \ \left(\frac{i}{2\pi}\right)^{a} \frac{1}{2} \frac{d^{a}\delta(\xi)}{d\xi^{a}}} \right\} \tag{2.62}$$

$$G(y) = \frac{1}{\alpha i^{4a}\Gamma(1+a)} \frac{d^{1+a}}{dy^{1+a}} F(y) * \delta(y) \tag{2.63}$$

$$G(y) = \frac{1}{\alpha i^{4a}\Gamma(1+a)} \frac{d^{a}}{dy^{a}} \left(\frac{dF(y)}{dy}\right) \tag{2.64}$$

For $N \equiv a \ mod \ 1$ and for $\boldsymbol{M} = \lfloor \boldsymbol{a} \rfloor$ so $a = N + M = \frac{D}{m+1}$, we have

$$G(y) = \frac{1}{\alpha i^{4(M+N)}\Gamma(1+M+N)} \frac{d^{N}}{dy^{N}} \left(\frac{d^{M+1}F(y)}{dy^{M+1}}\right) \tag{2.65}$$

For the simple case of the traditional three dimensions and uniform spherical growth we have $D = 3$ and $m = 0$, thus $a = 3$, $M = 0$, $N = 3$. Thus,

$$G(y) = \frac{1}{\alpha\Gamma(4)} \frac{d^3}{dy^3} \left(\frac{dF(y)}{dy} \right) \tag{2.66}$$

$$\alpha\Gamma(4) = \frac{12\pi^{\frac{D}{2}}(m+1)}{\Gamma\left(\frac{D}{2}+1\right)} = 8\pi \tag{2.67}$$

$$G(y) = \frac{1}{8\pi} \frac{d^4 F(y)}{dy^4} \tag{2.68}$$

Since $y = V(t)$, and since $m = 0$, we have $u(t) = v(t)$, thus

$$\frac{d}{dy} = \frac{1}{u(t)} \frac{d}{dt} \tag{2.69}$$

$$J(t) = \frac{1}{8\pi} \frac{d}{dt} \left[\frac{1}{u(t)} \frac{d}{dt} \left[\frac{1}{u(t)} \frac{d}{dt} \left[\frac{1}{u(t)} \frac{d}{dt} \left(-\ln\big(1 - f(t)\big) \right) \right] \right] \right] \tag{2.70}$$

Which is precisely equation the general nonisothermal Avrami equation, i.e., equation (2.33)!

2.2.3 *Phase size distribution and the initial conditions to the GNA equation*

The phase size distribution $\rho(r,t)$ can be defined as the number concentration density function per unit radii of the transformed phase, i.e., the number of spherulites N per unit volume that have radii between r_1 and r_2:

$$N = \int_{r_1}^{r_2} \rho(r,t)\,dr \tag{2.71}$$

More general solutions to the GNA Equation require either four initial conditions for $f(t)$, or three for $u(t)$. To identify these initial conditions, we now consider the population balance equation on phase size distribution $\rho(r,t)$, given initial distribution $R_0(r)$:

$$\frac{\partial \rho(r,t)}{\partial t} + \frac{\partial}{\partial r}\big(u(r,t)\rho(r,t)\big) = 0 \tag{2.72}$$

$$\rho(r,0) = R_0(r) \tag{2.73}$$

This picture is incomplete without including the new phase entering the system as nuclei. We consider the number of nuclei created in a small window of time to be $J(t)\Delta t$. By the definition of $\rho(r,t)$ this is equivalent to:

$$J(t)\Delta t = \int\limits_{r_0}^{r_0+u(t,r_0)\Delta t} \rho(r,t)dr \approx \rho(t,r_0)\rho\left(r_0 + \frac{u(t,r_0)}{2}\Delta t, t\right)\Delta t \tag{2.74}$$

Where r_0 is the critical radius.

Letting Δt approach zero leads to:

$$\rho(r_0,t) = \frac{J(t)}{u(r_0,t)} \tag{2.75}$$

Since r_0 is extremely small, we can shift r by r_0 and not affect the governing equations.

$$\rho(0,t) = \frac{J(t)}{u(0,t)} \tag{2.76}$$

For the radially independent case of growth velocity $u(t)$, using the method of characteristics, we note the solution is constant along the line $C = U(t) - r$. By observing that any phase nucleated after time zero will never catch up in size to phase due to the initial distribution, we can split the solution up into two regimes. The first pertains to the initial distribution of radii, $r - U(t) > 0$; the second pertains to the newly formed nucleated crystals, $r - U(t) < 0$. Using the initial and boundary conditions we then find the full solution as follows.

$$\rho(r,t) = g(C) = g(U(t) - r) \tag{2.77}$$

$$\rho(r,t) = \ \theta\big(r - U(t)\big)R_0\big(r - U(t)\big) + \theta(U(t) - r)\frac{J\Big(U^{-1}(U(t) - r)\Big)}{u\big(U^{-1}(U(t) - r)\big)} \tag{2.78}$$

Where $U^{-1}\big(U(t)\big) = t$, and θ is the Heaviside step function.

We can make the substitution $v = U^{-1}(t)$ to eliminate the inverse function, which can be found by can be solving the following differential equation:

$$\frac{dv}{dt} = \frac{1}{u(t)} \tag{2.79}$$

We can then rewrite equation (2.78) as

$$\rho(r,t) = \theta\big(r - U(t)\big)R_0\big(r - U(t)\big) + \theta(U(t) - r)\frac{J(v(U(t) - r))}{u\big(v(U(t) - r)\big)} \tag{2.80}$$

By integrating $\rho(r,t)$ multiplied by $\frac{4}{3}\pi r^3$, we arrive at an alternate expression for the extended volume of transformed phase. Then by applying equation (2.16) we find:

$$-\ln\big(1 - f(t)\big) = \int\limits_0^\infty \frac{4}{3}\pi r^3 \rho(r,t) dr \tag{2.81}$$

We can now use this equation to derive initial conditions to the GNA equation (2.33).

$$\frac{d^n}{dt^n}(-\ln\big(1 - f(t)\big))\bigg|_{t=0} = \frac{d^n}{dt^n}\left(\int_0^\infty \frac{4}{3}\pi r^3 \rho(r,t)\, dr\right)\bigg|_{t=0} \quad n \in 0{,}1{,}2{,}3 \tag{2.82}$$

$$f(0) = 1 - \exp\left(\ - \int_0^\infty \frac{4}{3}\pi r^3 R_0(r) dr\right) \tag{2.83}$$

$$\dot{f}(0) = \big(1 - f(0)\big)\int_0^\infty \frac{4}{3}\pi r^3 u(0) R_0'(r) dr \tag{2.84}$$

$$\ddot{f}(0) = \frac{\dot{f}(0)^2}{f(0) - 1} + (f(0) - 1)\int_0^\infty \frac{4}{3}\pi r^3 \Big(u(0)^2 R_0''(r) - \dot{u}(0) R_0'(r)\Big) dr \tag{2.85}$$

$$\begin{gathered} \dddot{f}(0) = \frac{3\dot{f}(0)\ddot{f}(0)}{f(0) - 1} - \frac{2\dot{f}(0)^3}{(f(0) - 1)^2} + \\ (f(0) - 1)\int_0^\infty \frac{4}{3}\pi r^3 \Big((2u(0)\dot{u}(0) + \dot{u}(0)^2) R_0''(r) - u^3(0) R_0'''(r) - \ddot{u}(0) R_0'(r)\Big) dr \end{gathered} \tag{2.86}$$

Alternatively, these could be rearranged in terms of initial conditions for $u(t)$, if it is the variable of interest.

$$u(0) = \frac{\dot{f}(0)}{\big(1 - f(0)\big) \int_0^\infty \frac{4}{3}\pi r^3 R_0'(r)\, dr} \tag{2.87}$$

$$\dot{u}(0) = \frac{\frac{\dot{f}(0)^2}{f(0) - 1} - \ddot{f}(0) + (f_0 - 1)\frac{4}{3}\pi \int_0^\infty r^3 \Big(u(0)^2 R_0^{''(r)}\ \Big)dr}{\frac{4}{3}\pi \int_0^\infty r^3 (R_0'(r)\ )dr} \tag{2.88}$$

$$\ddot{u}(0) = \frac{\left(\frac{3\dot{f}(0)\ddot{f}(0)}{f(0) - 1} - \dddot{f}(0) + \frac{2\dot{f}(0)^3}{(f(0) - 1)^2}\right)}{\int_0^\infty r^3 (R_0'(r)\ )dr} +$$

$$\frac{\frac{4}{3}\pi(f(0) - 1) \int_0^\infty r^3 (2u(0)u'(0)R_0''(r) + u'(0)^2 R_0''(r) - u^3(0)R_0'''(r)\ )dr}{\int_0^\infty r^3 (R_0'(r)\ )dr} \tag{2.89}$$

2.3 Applications to the Crystallization of Pure Water

We apply our model to the formation of solid ice in liquid water to test its validity and capabilities; this particular instance is relevant to the cryopreservation of biological systems, where rapid cooling and warming rates render the isothermal approximation invalid. For application, we require the temperature dependent properties for the crystal growth and nucleation rates of pure water.

2.3.1 *Temperature dependent growth rate of pure water*

Classical theory yields the growth rate as:

$$u(T) = \frac{k_B T}{3\pi \mathrm{a}_0^2 \eta(T)} \left(1 - \exp\left(-\frac{\Delta G(T)}{RT}\right)\right) \tag{1.16}$$

Where $\eta(T)$ is the dynamic viscosity, a_0 is the mean inter-atomic distance between water molecules, R is the universal gas constant, and ΔG is the free energy difference between the crystal and liquid phases. ΔG can be found from the relation $G = H - TS$. For the difference in free energy between supercooled water and crystallized water we have:

$$\mathit{\Delta} G = \frac{\mathit{\Delta} H_m \mathit{\Delta} T}{T_m} + \int_T^{T_m} (C_p^{cr} - C_p^m) dT + T \int_T^{T_m} (C_p^{cr} - C_p^m) \frac{dT}{T} \tag{1.15}$$

Where $C_p^{cr} - C_p^{m}$ is the difference in specific heats of the crystalline and melted phase, H_m is the melting enthalpy of water, T_m is the melting temperature of water, and $\Delta T = T_m - T$. Figure 2.3 shows the specific heat of super cooled water as a function of temperature below.[52]

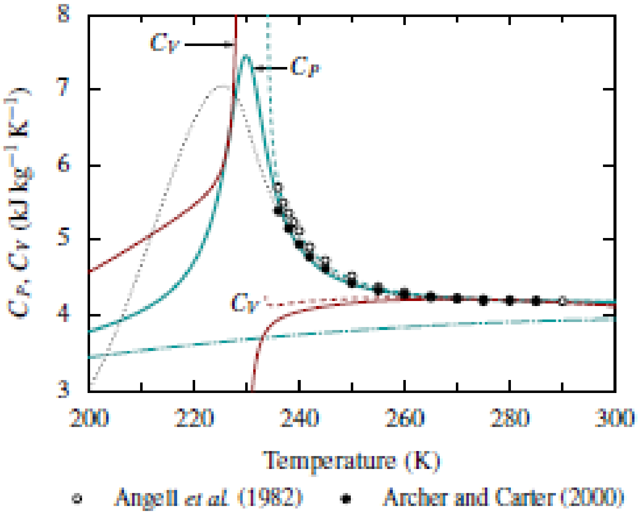

Figure 2.3. Plots shown of theoretical values of C_p^{cr} and C_p^{m} as the solid blue and dashed blue lines respectively.[52]

2.3.2 *Temperature dependent nucleation rate of pure water*

The rate at which nuclei are formed per unit time, $J(T)$, is defined bellow as a combination of the nuclei diffusion coefficient D and the Zeldovich factor Z.[14,16,53,54]

$$A = \rho_s D_* Z \tag{1.6}$$

$$D_* = \frac{i_* k_B T}{3\pi d_0^3 \eta} \tag{1.7}$$

$$Z = \sqrt{\frac{\Delta G_N / k_B T}{3\pi n_*}} = \frac{4R_*^2 \gamma_e}{9 k_B T n_*^2} \tag{1.8}$$

Where i_* is the number of molecules on the surface of a critical nuclei, n_* is the number of molecules in a critical nucleus, R_* is the radius of a critical nucleus, ρ_s is the number density of nucleation sites, γ_e is the ice-water inter-facial surface energy, and d_0 is the effective diameter of a water molecule. The work of formation of a critical nucleus of crystal is $\mathit{\Delta} G_N$, where ρ_s is the density of supercooled water and $\Delta\mu = \Delta h \Delta T / T_m$ is the chemical potential defined in terms of the specific melting enthalpy and melting temperature of water.

$$\mathit{\Delta} G_N = \frac{16\pi}{3} \frac{\gamma_e^3}{\rho_s^2 \mathit{\Delta}\mu^2} \tag{1.2}$$

Putting (1.2, 1.5-1.8) together yields the nucleation rate derived from CNT.

$$J = \rho_s D_* Z \exp\left(\frac{\Delta G_N}{k_B T}\right) \tag{1.90}$$

2.3.3 *Temperature dependent surface energy and viscosity of pure water*

The interfacial solid-liquid surface energy γ_e can be thought of as the excess energy stored in the interface between the two phases, characterizing the intermolecular forces between the liquid and the solid. In the case of water, temperature dependent ice-water interfacial surface energy values have been measured previously, showing a power law dependence on temperature.[15] Figure 2.4 shows the values of the ice-water interfacial energy, derived from nucleation data.

$$\lambda_e = \lambda_0 \left(\frac{T}{235.8}\right)^n \tag{1.91}$$

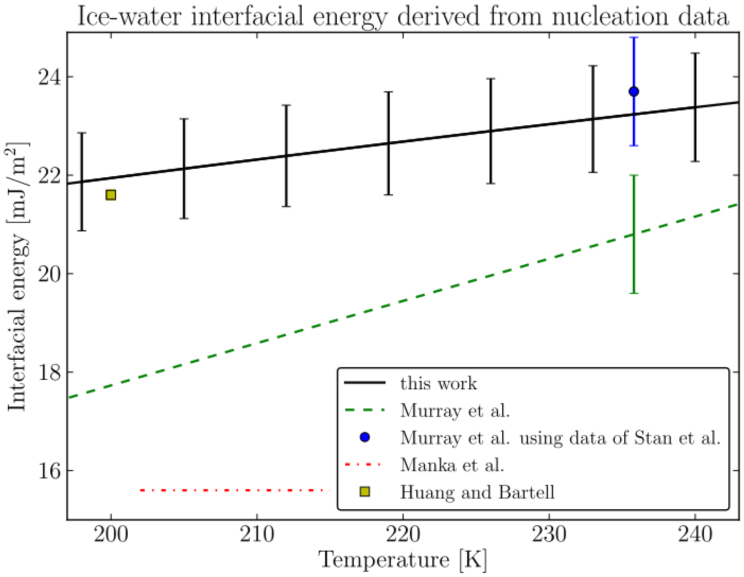

Figure 2.4. Comparison of the calculated ice–water interfacial energy with the literature.[15]

Several models have been proposed for an expression for the temperature dependent viscosity of supercooled water.[55–58] The power law (2.92) fits the data gathered by Dehaoui et al. well at high temperatures but begins to diverge to infinity well before the glass transition temperature of water. This divergence will cause problems in the model as the nucleation rate and growth rate heavily depend on viscosity. Using viscosity data compiled in the supplemental information of Dehaoui et al. we noticed that $\ln((\ln(\eta))$ displays asymptotic linearity as temperature decreases, thus a super-exponential fit (2.93) is appropriate. We propose a combined power law and super exponential functional form for the temperature dependent viscosity of water (2.94), giving a description much more accurately than the power law alone, while also eliminating the divergent behavior of the power law near T_s, see Figure 2.5.

$$\eta(T) = \eta_0 \left(\frac{T}{T_s} - 1\right)^{\gamma} \tag{2.92}$$

$$\eta(T) = \exp(\exp(-aT + b)) \tag{2.93}$$

$$\eta(T) = \frac{1}{1+\exp\big(\xi(T-T_0)\big)} \left[\exp(\exp(-aT+b)) + \eta_0 \left(\frac{T}{T_s} - 1\right)^{\gamma} \exp\big(\xi(T-T_0)\big)\right] \tag{2.94}$$

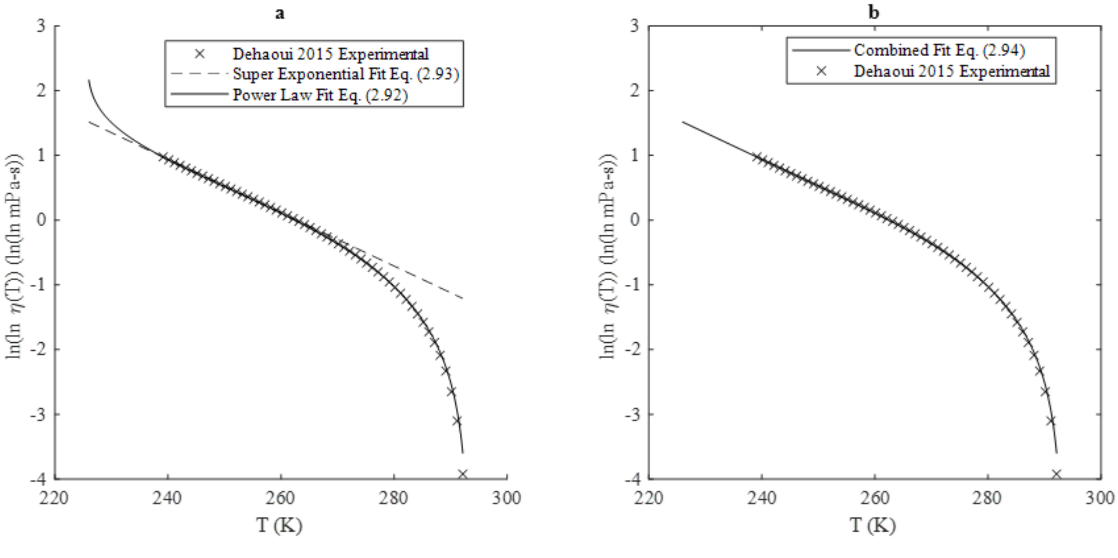

Figure 2.5. Temperature dependent viscosity $\eta(T)$ from the model and experimental data for (a) the power law model (2.91) vs super exponential model (2.92), and combined power law and super exponential fit (2.93).

2.3.4 *Simulation results for water crystallization*

The functional forms of the crystal growth rate and the nucleation are taken from classical theory and discussed above. By using data from the literature we estimated the ice crystal growth rates and homogeneous nucleation rates for supercooled water from CNT, given in Figure 2.6, which agree quite well with measurements from the literature. Additionally, the model parameters used in calculating the nucleation and growth rates of ice are given in Table 2.1.

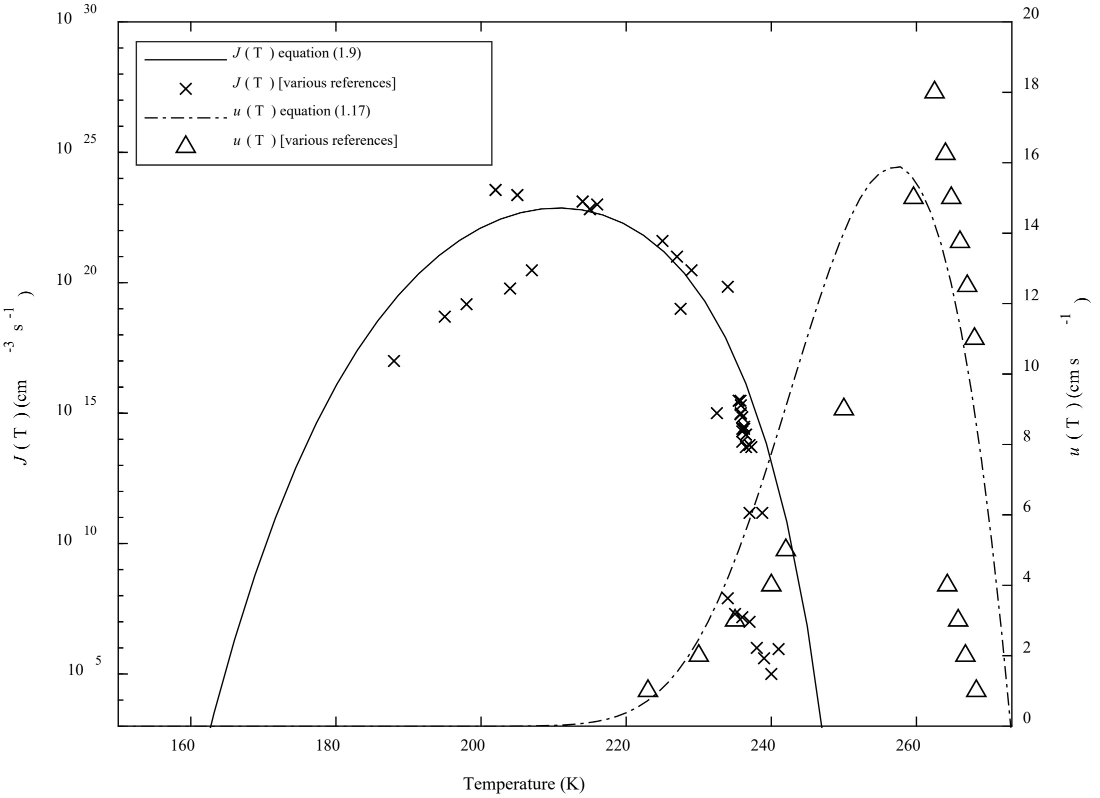

Figure 2.6. The temperature dependent growth and nucleation rates from CNT given the properties above Table 2.1 below, as well as measurements made in the literature.[28,59–64]

Table 2.1. Table of parameter values used in the crystallization model for pure water.

PARAMETERS	DESCRIPTION	VALUE
T_m	melting temperature	273.15 K
T_g	glass transition temperature	135 K
$\dot{T}$	cooling rate/warming rate	varies
ΔH_m	melting enthalpy	6.01 kJ/mol
a_0	mean interatomic distance	0.31 nm[65]
η_0	power law viscosity fit parameter	.13788 mPa-s
T_s	power law viscosity fit parameter	225.66 K
γ	power law viscosity fit parameter	1.6437
a	super exponential viscosity fit parameter	.04121 K^{-1}
b	super exponential viscosity fit parameter	10.82920
ξ	combined viscosity fit parameter	100 K^{-1}
T_0	combined viscosity fit parameter	257.66 K
ρ_i	number density of water molecules	3.35×10^{22} cm^{-3}
i_*	Number of molecules on the surface of a critical nucleus	20 (Estimated from n_*)
n_*	Number of molecules in a critical nucleus	100[66]
d_0	Diameter of water molecule	.27 nm[67]
R_*	Radius of critical nucleus	1.20 nm[68]

Figure 2.7 shows how the solution to equation (2.72) the PDE governing phase size distribution of ice crystals, behaves. Specifically, Figure 2.7(a) depicts a hypothetical initial distribution of crystals at 135 K (the glass transition temperature, T_g) formed via homogeneous nucleation at a cooling rate of 10^6 K/s. Figure 2.7(b) depicts the evolution of

this size distribution as the system is rewarmed at a rate of 10^6 K/s at a temperature of 225 K. The dashed vertical line $r = U(t)$ separates the portion of the phase size distribution due to nucleation and the portion due to the initial distribution present from cooling; both are simply calculable using equation (2.78). Figure 2.8 expands on these results, showing how a small initial distribution of ice crystals in water grows with time as the temperature is increased from T_g to T_m (273 K) at different rates, as well as the results for the transformed fraction for each simulated condition.

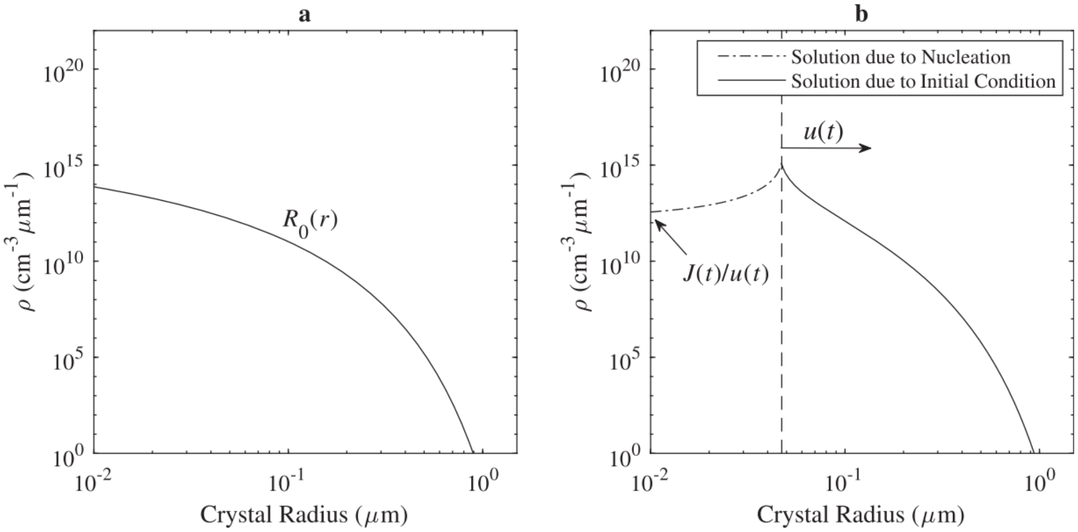

Figure 2.7. Solutions to the partial differential equation (2.78) for water given the temperature-dependent nucleation rate $J(T)$ (1.9) and crystal growth rate $u(T)$ (1.16) predicted from CNT. (a) An initial crystal distribution resulting from cooling at 10^6 K/s from 273 to 135 K without an initial distribution. (b) The evolution of $\rho(r,t)$ from (a) when warmed at 10^6 K/s at the instant of T = 225 K.

Some characteristics of the curves in Figure 2.8 are worth discussing. We observe that the peak value of $\rho(r,t)$ does not change with time, but only shifts in position. This is a consequence of the definition of $\rho(r,t)$, the assumption of uniform temperature throughout the volume, and radially independent growth. This means that all the spherulites throughout the domain grow at the same rate, irrespective of size and position. Thus, the number of spherulites with radii in the interval $[r_1, r_1 + u(t)]$ is constant, and the maximum value of

$\rho(r,t)$ is constant in Figure 2.8. Additionally, the growth rate changes exponentially with time, and it is convenient to show $\rho(r,t)$ over a large window of radii. It is this log-scale representation of crystal radius in Figure 2.8 that appears to shrink the width of $\rho(r,t)$ as time progresses.

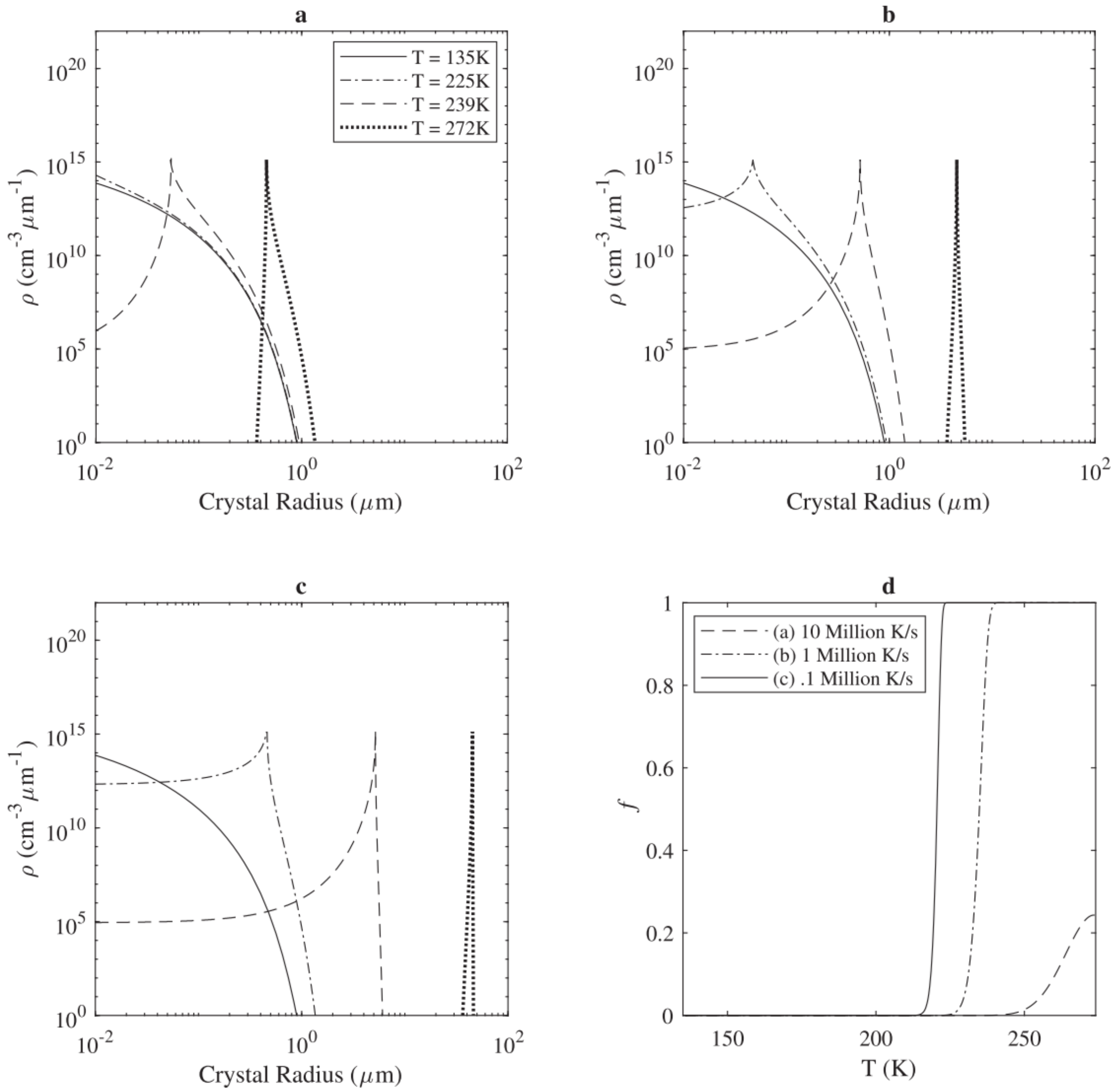

Figure 2.8. Solutions to the partial differential equation (2.78) and the GNA equation (2.33) for water and an initial crystal distribution formed from cooling 10^6 K/s from 273 to 135 K. Starting with the initial crystal distribution, the system was warmed from 135 to 273 K at (a) 10^7 K/s, (b) 10^6 K/s, and (c) 10^5 K/s. (d) The resulting fraction crystallized as a function of temperature during warming for each of the three cases.

To demonstrate the importance of applying the non-isothermal approach, we also compare to predictions applying the Avrami equation for the transformed fraction at different cooling rates, seen in Figure 2.9(a). The Avrami solution in Figure 2.9 was obtained by directly inserting $u(t)$ and $J(t)$ into equations (2.11) and (2.16) for water being cooled from 273K to 135K at various cooling rates, with the temperature history $T(t)$ determining $u(t)$ and $J(t)$. Examining the temperature difference in Figure 2.9(b) between the Avrami and full solution at ice fractions of $f = 0.5$, we notice that the temperature difference increases exponentially with cooling rate, with the two solutions becoming identical as cooling rate approaches zero. Not only does this demonstrate that the non-isothermal theory recovers the isothermal result, but also that it is particularly important for studying systems that undergo crystallization while experiencing rapid changes in temperature, such as cryobiological systems, rapid quenching in materials synthesis, and rapid calorimetry.[69,70]

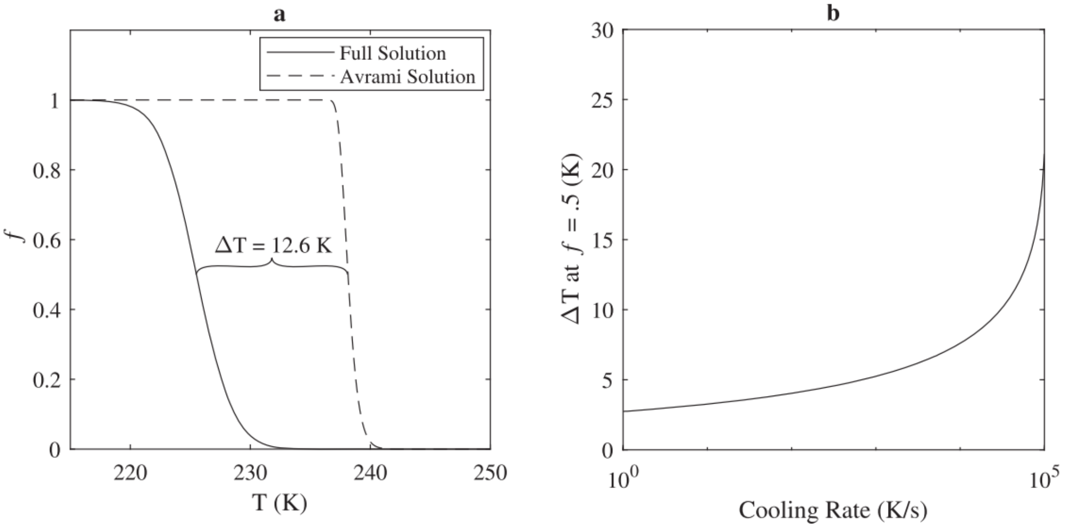

Figure 2.9. (a) The transformed fraction predicted using the full, non-isothermal solution and the Avrami solution for a cooling rate of 5.5×10^4 K/s. (b) Temperature difference at a crystal fraction of 0.5 between the Avrami equation applied to nonisothermal systems and the full solution to the differential equation for water being cooled from 273 to 135 K at 1–10^5 K/s.

Figure 2.10 displays the model results for ice fraction as a function of cooling rate considering homogeneous nucleation (zero transformed fraction at T_m). Denoted in the

Figure 2.10 is the experimentally inferred critical cooling rate of water from capillary tube x-ray diffraction (diamond) and capillary tube optical detection (denoted range). Since XRD is sensitive to crystal fractions of approximately one part in one hundred, the XRD experiments of liquid nitrogen quenched glycerol dilutions suggest that cooling rates of approximately 320,000 K/s in pure water correspond to a crystal fraction of $f = .01$.[69] This is almost exactly the model result. Similarly, with optical detection, quartz capillary quenching measurements place the critical cooling rate of water between 100,000-1,000,000 K/s.[70] Additionally, the non-isothermal theory predicts that the critical warming rate necessary to achieve apparent vitrification, i.e., $f = .01$, is approximately 100 million K/s.

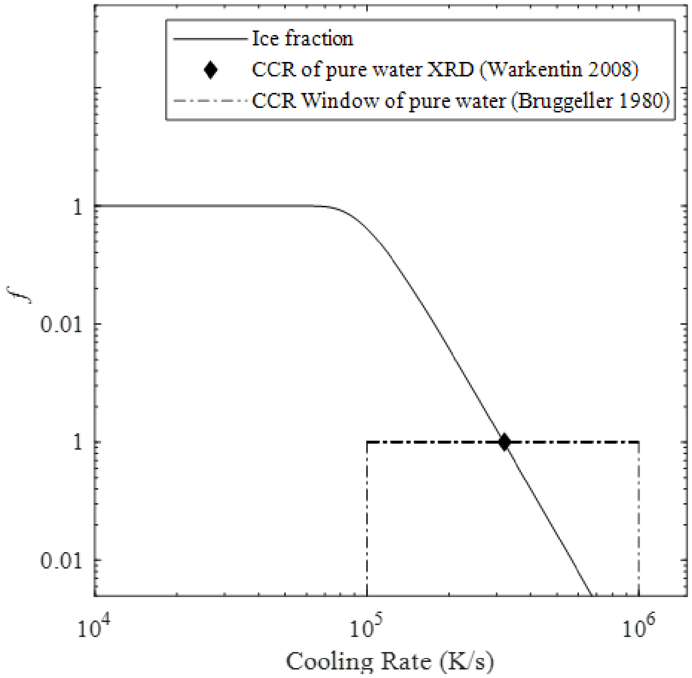

Figure 2.10. Transformed (ice) fraction as a function of cooling rate, predicted from the non-isothermal theory, by cooling from the melting temperature to the glass transition temperature of 135 K of supercooled water. Experimentally inferred vitrification cooling rates are noted near $f = .01$.

In developing the theory throughout this chapter, we have specifically assumed uniform, though time-varying, temperature in the domain of interest. Problems may arise when applications are made to systems with appreciable spatial gradients in temperature. If these gradients are sufficiently small, such that the temperature across the largest phase inclusion in $\rho(r,t)$ can be considered constant, then the domain may be partitioned into separate regions that do not interact with each other in terms of nucleation and growth, with traditional heat transfer equations (including latent heat release) used to monitor spatial and temporal temperature evolution. If, however, there are thermal gradients on or below the size scale of the largest inclusions of phase, other methods will be needed to resolve the phase change in these regions.

2.4 Critical Cooling Rates and Critical Warming Rates

Let us now consider the critical cooling rate (or critical warming rate) in light of the GNA equation (2.33). Let us now define $K(t) = -\ln\big(1 - f(t)\big)$, then by integrating 2.33 four times with respect to time we get

$$K(t) = 8\pi \int_0^t u(t_1) \int_0^{t_1} u(t_2) \int_0^{t_2} u(t_3) \int_0^{t_3} J(t_4) dt_4 dt_3 dt_2 dt_1 \tag{2.95}$$

We can also consider the case where the temperature decreases at a constant rate $\dot{T}$ between the melting point T_m and the glass transition T_g. By the chain rule, we have

$$T(t) = T_m - \dot{T}t \Longrightarrow \frac{d}{dt} = \frac{d}{dT}\frac{dT}{dt} = -\dot{T}\frac{d}{dT} \tag{2.96}$$

Thus, equation (2.33) becomes

$$J(T) = \frac{\dot{T}^4}{8\pi}\frac{d}{dT}\left[\frac{1}{u(T)}\frac{d}{dT}\left[\frac{1}{u(T)}\frac{d}{dT}\left[\frac{1}{u(T)}\frac{df(T)}{dT}\frac{1}{f(T)-1}\right]\right]\right] \tag{2.97}$$

Integrating equation (2.97) gives us $K(T,\dot{T})$, a function of both temperature and cooling rate

$$K(T,\dot{T}) = \frac{8\pi}{\dot{T}^4} \int_{T_m}^{T} u(T_1) \int_{T_m}^{T_1} u(T_2) \int_{T_m}^{T_2} u(T_3) \int_{T_m}^{T_3} J(T_4) dT_4 dT_3 dT_2 dT_1 \tag{2.98}$$

We can now express the transformed fraction as a function of temperature and cooling rate

$$f(T,\dot{T}) = 1 - \exp\left(-K(T,\dot{T})\right) \tag{2.99}$$

Now suppose we consider the transformed fraction of the substance at the glass transition temperature, its final transformed fraction as crystallization ceases at T_g. Then we now only have the transformed faction as a function of cooling rate.

$$f(\dot{T}) = 1 - \exp\left(-\frac{A}{\dot{T}^4}\right) \tag{2.100}$$

$$A = 8\pi \int_{T_m}^{T_g} u(T_1) \int_{T_m}^{T_1} u(T_2) \int_{T_m}^{T_2} u(T_3) \int_{T_m}^{T_3} J(T_4) dT_4 dT_3 dT_2 dT_1 \tag{2.101}$$

Thus, for some critical fraction f_{ccr} which we consider to be the threshold of the critical cooling rate, we have the critical cooling rate $\dot{T}_{ccr}$ as

$$\dot{T}_{ccr} = \left(\frac{-8\pi A}{\ln(1 - f_{ccr})}\right)^{\frac{1}{4}} \tag{2.102}$$

For crystallization where the crystals are not spherical, we look to equation (2.65). Thus, for a crystal of dimensionality $D + 1 = n$ (Avrami parameter), we have

$$f(\dot{T}) = 1 - \exp\left(-\frac{A}{\dot{T}^n}\right) \tag{2.103}$$

$$\dot{T}_{ccr} = \left(\frac{-8\pi A}{\ln(1 - f_{ccr})}\right)^{\frac{1}{n}} \tag{2.104}$$

For these cases, A is not easily determined through the methods shown thus far. We will expand on the origins and meaning of the Avrami parameters and their relationship to the nucleation rate, growth rate, and fractal dimension of growth in the next chapter.

2.5 Conclusion

We developed a theory that clearly established the relationship between the transformed fraction, phase size distribution, nucleation rate, and growth rate for arbitrary temperature–time history and arbitrary initial phase size distribution. This theory can be contrasted with the isothermal Avrami equation; at infinitesimal cooling rates, the two approaches converge in predictions, and at increasing cooling rates, the Avrami equation predictions for the transformed fraction increasingly deviate from the non-isothermal theory prediction. We demonstrate the applicability of the non-isothermal theory by comparing predictions for the critical cooling rate of water to measurements, yielding strong agreement between the two. We argue for future implementation of this approach in predicting not only phase size distributions and transformed fractions in non-isothermal systems, but also to infer nucleation rates and growth rates from phase size distribution and transformed fraction measurements.

ADAPTED FROM

Kangas, J., Bischof, J. C. & Hogan, C. J. Kinetics of nonisothermal phase change with arbitrary temperature-time history and initial transformed phase distributions. *J. Chem. Phys.* **155**, (2021)

AKNOWLEDGMENTS

This work was supported by the National Science Foundation, Grant No. 1941543, NSF Engineering Research Center for Advanced Technologies for Preservation of Biological Systems (ATP-Bio).

Chapter 3

Unraveling Avrami—Extracting Nucleation and Growth Rates from Calorimetry Curves

3.1 Introduction

The Avrami equation is a simple relationship describing the time evolution of the fraction of transformed phase in a system undergoing phase change, i.e., nucleation and growth of a new phase in a pre-existing phase.[45–47] It finds application in a diversity of fields, including, but not limited to, metallurgy[71–74], polymer science[75,76], food science, pharmacology[77], and cryobiology[78,79]. It is perhaps of greatest utility in analyzing differential scanning calorimetry (DSC) measurements; such measurements enable inversion of transformed phase fraction versus time. A common data interpretation approach in DSC is to fit the parameters k and n in the modified Avrami equation, which is given as:

$$f(t) = 1 - \exp(-kt^n) \tag{3.1}$$

Where $f(t)$ is the fraction of transformed phase. The traditional Avrami equation, derived for constant spherically symmetric growth under isothermal conditions, yields exactly $n = 4$ and $k = \pi u^3 J/3$, where u is the growth velocity and J is the nucleation rate. However, a variety of measurements in both pure substances and mixtures yield non-integer values of n and therefore also distinct values of k, as it must correspondingly change in dimension.[80,81] Prior studies have identified that the non-integer time-exponents (n values) are linked to the shape of the growing inclusions of transformed phase, i.e. the growing nuclei.[82,83] In this chapter, we show that by considering newly formed nuclei as growing fractals with an arbitrary shape and dimensionality, we can use this unique growth velocity in the population balance equation to recover the Avrami equation, and thus explain k and n for arbitrary values.

DSC, an important tool in analyzing phase change processes, measures the associated heat release during a prescribed temperature-time trajectory imposed on a system. In DSC, a small sample is placed in a pan of known mass, which is placed in the DSC device. The pan is then altered in temperature according to predefined specifications. Through a series of temperature measurement devices connected to the pan, along with an empty pan of known mass, the heat released from the sample can be calculated. This allows for measurements of specific heat as a function of temperature. Additionally, it provides a heat release curve that can be analyzed and converted to the transformed fraction. This also requires knowledge of the enthalpy of fusion of the sample material, though this is also easily measurable on DSC. We will show later on in this chapter how DSC can be utilized to extract the dimensionality (or fractal dimension) of growing phase, and the associated changes in the nucleation and growth rate accompanying a change in temperature.

3.2 Avrami Exponents in Terms of Fundamental Parameters

The three key fundamental parameters characterizing many phase change processes are the nucleation rate J, growth rate u, and dimensionality D of the newly formed phase. These define the rate of formation of new phase nuclei, their growth rate, and growth geometry, respectively. Under idealized circumstances, when the growing nuclei geometry is easily expressible, such as a sphere, rod, or disk, the Avrami parameters k and n have been derived from first principles, and for constant nucleation and growth rates, the parameter n, is $D + 1$. However, aside from these idealized cases, such as in most applications, the growing nuclei geometries are complex and thus k remains ill-defined. In application, k and n are calculated by curve fitting, typically of calorimetry curves, and thus are easily extractable from experiments when appropriate. However, the Avrami equation has also been shown to fail under a variety of circumstances, but the extent to which it is applicable and under what conditions it breaks down remains unclear. This can likely be attributed to the lack of theory underpinning its usage aside from the noted idealized circumstances. Throughout this chapter we will demonstrate under what conditions equation (3.1) is valid and how k and n are related to the fundamental parameters J, u, and D. For the duration of this chapter, we will consider crystallization, but the discussed theory holds equally true for many other phase change processes involving nucleation and growth.

In this chapter, we treat the growth of complex geometries, in fact arbitrarily complex geometries, as spheres of equal volume. In this fashion, the growth rate of the true geometry has a corresponding spherical growth rate, which is radially dependent, that is, it changes with the radius of the sphere. The method outlined in Kangas et al. (2021) for deriving the set of equations used in this paper stems from probabilistic treatments of transformed spaces lying inside a larger untransformed space. Geometry of the growing transformed spaces plays no part in the derivation and the only required assumption is that the spaces form uniformly within the greater transformed space.

3.2.1 *Radial dependence and equivalent volume*

In this section we examine various crystal geometries and their effect on the growth rate u discussed in the previous chapters.

Rods ($n = 2$)

For simple geometries some solutions for n and k in terms of the fundamental parameters are known. Let us consider the case of where the growing solid is a rod of radius r_{rod} and length L growing at rate v_0. Instead of treating the rod as a rod, let us treat it as a sphere with an equivalent volume to the growing rod, meaning the effective spherical volume will grow at a rate u dependent on the radius and not at a constant rate like the rod does. The growth rate u is dependent on the radius r_s in the following fashion:

$$u = \frac{v}{r_s^m} \tag{3.2}$$

Where v is some velocity scaling constant that is a function of the shape of the crystal, and m is related to the fractal dimension of the growing crystal. The origins of this functional form will be explained later in this section. Let us now compare the volumes of the equivalent sphere of radius r_s and the rod of length L.

$$V_{rod} = \pi r_{rod}^2 L \tag{3.3}$$

$$V_{sphere} = \frac{4\pi}{3} r_s^3 \tag{3.4}$$

Setting $V_{rod} = V_{sphere}$ we have

$$\pi r_{rod}^2 L = \frac{4\pi}{3} r_s^3 \tag{3.5}$$

$$L = \frac{4 r_s^3}{3 r_{rod}^2} \tag{3.6}$$

$$\frac{dL}{dt} = \frac{4 r_s^2}{r_{rod}^2} \frac{dr_s}{dt} \tag{3.7}$$

$$v_0 = \frac{4 r_s^2}{r_{rod}^2} u(r_s) \tag{3.8}$$

Here we see that the growth rate of the sphere of equivalent volume can be written in the form

$$u(r) = \frac{v}{r^m} \tag{3.9}$$

Thus, we can express the denominator v in terms of the other geometrical properties

$$u(r_s) = \frac{v_0 r_{rod}^2/4}{r_s^2} \tag{3.10}$$

$$v = \frac{v_0 r_{rod}^2}{4} \tag{3.11}$$

$$m = 2 \tag{3.12}$$

Discs $(n = 3)$

We now examine a disc of growing radius r_{disc} and thickness h

$$V_{disc} = \pi h r_{disc}^2 \tag{3.13}$$

$$\pi h r_{disc}^2 = \frac{4\pi}{3} r_s^3 \tag{3.14}$$

$$r_{disc} = \sqrt{\frac{4}{3h} r_s^3} \tag{3.15}$$

$$\frac{dr_{disc}}{dt} = \frac{dr_s}{dt} \sqrt{\frac{3}{h} r_s} \tag{3.16}$$

$$u(r_S) = \frac{v_0 \sqrt{\frac{3}{h}}}{r_s^{\frac{1}{2}}} \tag{3.17}$$

$$v = v_0 \sqrt{\frac{3}{h}} \tag{3.18}$$

$$m = \frac{1}{2} \tag{3.19}$$

Spheres $(n = 4)$

A growing sphere is a trivial case that is worth mentioning. Since the effective spherical volume of a sphere is identical to the volume of the sphere itself, then there is no radial dependence of the growth of the effective sphere, thus

$$u = v \tag{3.20}$$

$$m = 0 \tag{3.21}$$

Arbitrary Geometry

We consider a crystal with an arbitrary geometry which grows at a constant velocity v_0. Then the volume V of this crystal with length scale L, dimensionality D, and scaling term A is

$$V = AL^D \tag{3.22}$$

Comparing this to the effective spherical volume of radius r we get

$$\frac{4}{3}\pi r^3 = AL^D \tag{3.23}$$

Isolating L yields

$$L = \sqrt[D]{\frac{3Ar^3}{4\pi}} \tag{3.24}$$

We can introduce the volume scaling factor α to relate the velocity of the sphere $u(r)$ to the velocity of the crystal v_0:

$$\alpha = \frac{3}{D}\left(\frac{4\pi}{3A}\right)^{\frac{1}{D}} \tag{3.25}$$

$$\frac{dL}{dt} = \alpha r^{\frac{3}{D}-1}\frac{dr}{dt} \tag{3.26}$$

$$\frac{dr}{dt} = u, \quad \frac{dL}{dt} = v_0, \quad v = \frac{v_0}{\alpha} \tag{3.27}$$

$$u(r) = \frac{v}{r^{\frac{3}{D}-1}} \tag{3.28}$$

We now see that for an arbitrary geometry with area scaling term A, characteristic length L growing at constant velocity v_0, and fractal dimension D, we recover

$$v = \frac{v_0}{\frac{3}{D}\left(\frac{4\pi}{3A}\right)^{\frac{1}{D}}} \tag{3.29}$$

$$m = \frac{3}{D} - 1 \tag{3.30}$$

The relationship between dimensionality D, Avrami parameter n, and our model parameter m is summarized in Table 3.1 below. The question now arises on how we define v since its dimensionality is not m/s. Suppose we have disc growth so $n = 3$, and thus $m = 0.5$. Then we have $u(r) = \frac{v}{\sqrt{r}} \equiv ms^{-1}$. Thus $[v] \equiv\ m^{3/2}s^{-1}$.

Table 3.1. Equivalent values for the fractal dimension of the growing solid D, the radial growth parameter m, and the Avrami parameter n.

D	m	n
3 (sphere-like growth)	0	4
2 (disc-like growth)	.5	3
1 (rod-like growth)	2	2

3.2 *Linking the crystal nucleation and growth rates to the Avrami parameters*

To establish a link between k and n, we first need to introduce the phase size distribution $\rho(r,t)$, the number density function per unit radius for the distribution of spherically equivalent crystals of radius r. Recall that given $\rho(r,t)$, the number of crystals N per unit volume that have radii between r_1 and r_2 is:

$$N = \int_{r_1}^{r_2} \rho(r,t)dr \tag{2.71}$$

The governing equations for the time evolution of $\rho(r,t)$ given an initial distribution $R_0(r)$, nucleation rate $J(t)$, and growth rate $u(t)$are:

$$\frac{\partial\rho(r,t)}{\partial t} + \frac{\partial}{\partial r}\big(u(r,t)\rho(r,t)\big) = 0 \tag{2.72}$$

$$\rho(r,0) = R_0(r) \tag{2.73}$$

$$\rho(0,t) = \frac{J(t)}{u(0,t)} \tag{2.76}$$

We will now examine the change in $\rho(r,t)$ when the growth velocity has no time-dependence (under isothermal conditions) and there is no initial distribution of transformed phase $R_0(r) = 0$. In chapter 2, we presented a general solution to equation (3.32), which in this isothermal instance, is expressed bellow.[59]

$$\rho(r,t) = \frac{J\theta\big(t-\xi(r)\big)}{u(r)} \tag{3.31}$$

Where θ is the Heaviside step function and ξ is:

$$\xi(r) = \int \frac{dr}{u(r)} \tag{3.32}$$

Linking transformed fraction to $\rho(r,t)$ while accounting for overlap in transformed phase yields the equation:

$$-\ln\big(1-f(t)\big) = \int_0^\infty \frac{4\pi r^3}{3}\rho(r,t)dr \tag{2.81}$$

We then equate right hand sides of equations (2.81) and (3.1) with (3.31) to show the link between n and k and the fundamental values of u, J, and m, defining nucleation and growth:

$$kt^n = \int_0^\infty \frac{4\pi J r^{3+m}}{3v}\theta\left(t-\frac{r^{m+1}}{(m+1)v}\right)dr \tag{3.33}$$

For isothermal conditions, we have $u(r)$ described by equation (3.2). Since temperature is constant, we will refer to $v(T)$ and $m(T)$ as simply v and m. By applying the following substitutions $z = \frac{r^{m+1}}{(m+1)v}$ and $dz = dr\frac{r^m}{v}$ we arrive at:

$$kt^n = \frac{4\pi}{3}J\big((m+1)v\big)^{\frac{3}{m+1}}\int_0^\infty z^{\frac{3}{m+1}}\theta(t-z)dz \tag{3.34}$$

$$kt^n = \frac{4\pi(1+m)}{3(4+m)}J\big((m+1)v\big)^{\frac{3}{m+1}}t^{\frac{4+m}{1+m}} \tag{3.35}$$

This solution can conveniently be separated into two parts; there is a constant portion corresponding to k and time exponential portion corresponding to t^n. This yields:

$$k = \frac{4\pi(1+m)}{3(4+m)}J\big((m+1)v\big)^{\frac{3}{m+1}} = \frac{4\pi J}{3n}\left(\frac{3v}{n-1}\right)^{n-1} \tag{3.36}$$

$$t^n = t^{\frac{4+m}{1+m}} \tag{3.37}$$

$$n = \frac{4+m}{1+m} = D+1 \tag{3.38}$$

Equations (3.36) and (3.37) demonstrate a clear link between the time-exponent in the modified Avrami equation and the radial-dependent growth exponent.

3.3 Solid-Phase Growth and Nucleation Rates from Calorimetry Curves

3.3.1 *Extracting the Avrami parameters from DSC curves*

Extracting the Avrami parameters from a calorimetric curve is a well-established experimental method.[84] The transformed fraction $f(t)$ can be found by integrating the baseline corrected heat flow per unit mass $q(t)$ between the onset and offset times of solidification (t_{on} and t_{off} respectively) and dividing by the enthalpy of fusion ΔH°_{fus}.

$$f(t) = \frac{1}{\Delta H^{\circ}_{fus}} \int_{t_{on}}^{t \le t_{off}} q(t)dt \tag{3.39}$$

From equation (3.1) we can see that

$$\ln(-\ln(1 - f(t))) = \ln(k) + n\ln(t) \tag{3.40}$$

To find n and k, $\ln(-\ln(1 - f(t)))$ is plotted against $ln(t)$. The slope of this line is n, while $\ln(k)$ is the $\ln(t)$-intercept.

3.3.2 *Calculating the change in nucleation and growth rates via a step-change in temperature*

We consider a system in the liquid state that is rapidly brought to a temperature T_1, below its melting point, and thus begins to crystallize. Then, after a certain amount of time $t = s$ passes, the system is rapidly brought to a second temperature T_2, also below the melting point. We assume the temperature transitions are fast compared to the rate of crystallization, and thus crystallization during the temperature jumps can be ignored. The phase change kinetics of this system are outlined below. Given the PDE (2.72), we can rearrange the equation as follows:

$$\rho_t + u\rho_r = -u_r\rho \tag{3.41}$$

$$u(r,t) = \frac{v(t)}{r^m} \tag{3.42}$$

$$\rho_t + \frac{v(t)}{r^m}\rho_r = m\frac{v(t)}{r^{m+1}}\rho \tag{3.43}$$

We notice the following series of differentials are equal to one another.

$$\frac{dt}{1} = \frac{r^m dr}{v(t)} = \frac{r^{m+1}d\rho}{mv(t)\rho} \tag{3.44}$$

The first characteristic gives us

$$v(t)dt = r^m dr \tag{3.45}$$

$$A = \frac{r^{m+1}}{m+1} - V(t) \tag{3.46}$$

Where $V(t)$ is the antiderivative of v with respect to time.

The second characteristic gives us

$$m\frac{dr}{r} = \frac{d\rho}{\rho} \tag{3.47}$$

$$\rho = Br = f(A)r \tag{3.48}$$

Thus, $\rho(r,t)$ has the form

$$\rho(r,t) = r^m f\left(\frac{r^m}{m+1} - V(t)\right) \tag{3.49}$$

Via the method of characteristics, the solution to equation (3.49) has the form $\rho(r,t) = r^m g(r^{m+1} - (m+1)vt)$ for constant v, for some function g. Applying the initial and boundary conditions (2.73) and (2.76), along with the growth velocity from equation (3.2), we get:

$$\rho(r,t) = \theta(r^{m+1}(m+1)vt)\frac{r^m R_0\left((r^{m+1}-(m+1)vt)^{\frac{1}{m+1}}\right)}{(r^{m+1}-(m+1)vt)^{\frac{m}{m+1}}} + \theta\left(vt - \frac{r^{m+1}}{m+1}\right)\frac{J}{v}r^m \tag{3.50}$$

We then consider equation (3.2) at two different temperatures T_1 and T_2.

$$u_1(r) = \frac{v_1}{r^{m_1}}, \qquad u_2(r) = \frac{v_2}{r^{m_2}} \tag{3.51}$$

At time $t = s$, the system transitions from temperature T_1 to T_2 instantaneously, thus we can use equation (3.50) to see what happens to the solution. We will use the previous solution for T_1 as the initial condition for the T_2 problem. For the T_1 case, we have no initial crystallization, so the solution is:

$$\rho_1(r,t) = \theta\left(v_1 t - \frac{r^{m_1+1}}{m_1+1}\right)\frac{J_1}{v_1} r^{m_1} \tag{3.52}$$

At time $t = s$, we change the temperature from T_1 to T_2, so $\rho_1(r,s) = R_0(r)$ is used as the initial condition for the T_2 case, with the new time $t-s$. We can ignore the term equating to the nucleation of new solids at the new temperature for small times after the temperature jump.

$$\begin{gathered}\rho_2(r,t) = \\ \frac{J_1}{v_1} r^{m_2}\theta\big(r^{m_2+1} - (m_2+1)v_2(t-s)\big)\theta\left(v_1 s - \frac{\big(r^{m_2+1} - (m_2+1)v_2(t-s)\big)^{\frac{m_1+1}{m_2+1}}}{m_1+1}\right)\big(r^{m_2+1} - (m_2+1)v_2(t-s)\big)^{\frac{m_1-m_2}{m_2+1}}\end{gathered} \tag{3.53}$$

In what follows, we will show how the difference in the solution before and after the temperature jump can be used to extract information about the change in growth velocity and nucleation rate. Recall equation (2.81), the transformed fraction is

$$-\ln\big(1 - f(t)\big) = \int_0^\infty \frac{4\pi r^3}{3}\rho(r,t)dr \tag{3.54}$$

Now we will consider how the system solidifies shortly after the temperature jump. Since there has not been sufficient time for phase change due to the growth of newly nucleated solids after the temperature jump, then we can focus solely on the growth of the previously formed solids. We compare the time derivative of the transformed fraction immediately before the temperature jump at $t = s$, f_1, to immediately after the temperature jump, f_2. Since

$$\frac{\partial}{\partial t}(-\ln\big(1 - f_1(t)\big)) = \frac{\partial}{\partial t}\int_0^\infty \frac{4}{3}\pi r^3 \rho_1(r,t)dr \tag{3.55}$$

Given a velocity of $u_1(r)$, we know that at time $t = s$ we arrive at a maximum crystal radius R_{max} of:

$$R_{max} = \big(v_1 s(m_1+1)\big)^{\frac{1}{m_1+1}} \tag{3.56}$$

We can thus ignore all values of $r > R_{max}$. Next, by combining equations (3.53) and (3.54) we have

$$\frac{\partial}{\partial t}\Big(-\ln\Big(1 - f_1(s)\Big)\Big) = \frac{4}{3}\pi \int_0^{R_{max}} r^3 \frac{\partial \rho_1(r,s)}{\partial t} dr \tag{3.57}$$

From equation (3.57) we have

$$\frac{d\rho_2(r,s)}{dt} = v_2 \frac{J_1}{v_1}\left[\delta\left(s\,v_1 - \frac{r^{m_1+1}}{m_1+1}\right) r^{2m_1-m_2} + \theta\left(s\,v_1 - \frac{r^{m_1+1}}{m_1+1}\right)(m_2 - m_1) r^{m_1-m_2-1}\right] \tag{3.58}$$

$$\frac{\dot{f}_2(s)}{f_2(s) - 1} = \frac{4\pi}{3}\int_0^\infty r^3 \frac{\partial \rho(r,s)}{\partial t} dr \tag{3.59}$$

$$\frac{\dot{f}_2(s)}{f_2(s) - 1} = \frac{4\pi v_2}{3}\frac{J_1}{v_1}\int_0^\infty \delta\left(sv_1 - \frac{r^{m_1+1}}{m_1+1}\right) r^{3+2m_1-m_2} + \theta\left(sv_1 - \frac{r^{m_1+1}}{m_1+1}\right)(m_2 - m_1) r^{2+m_1-m_2} dr \tag{3.60}$$

$$\frac{\dot{f}_2(s)}{f_2(s) - 1} = I_1 + I_2 \tag{3.61}$$

First integral

$$I_1 = \frac{4\pi v_2}{3}\frac{J_1}{v_1}\int_0^\infty \delta\left(sv_1 - \frac{r^{m_1+1}}{m_1+1}\right) r^{3+2m_1-m_2} dr \tag{3.62}$$

$$y = v_1 - \frac{r^{m_1+1}}{m_1+1} \tag{3.63}$$

$$r = \big((v_1 s - y)(m_1+1)\big)^{\frac{1}{m_1+1}} \tag{3.64}$$

$$dy = -r^{m_1} \tag{3.65}$$

$$I_1 = \frac{4\pi v_2}{3}\frac{J_1}{v_1}\int_0^{sv_1} \delta\,(y)\big((v_1 s - y)(m_1+1)\big)^{\frac{3+m_1-m_2}{m_1+1}} dy \tag{3.66}$$

$$I_1 = \frac{4\pi v_2}{3}\frac{J_1}{v_1} R_{max}^{3+m_1-m_2} \tag{3.67}$$

Second integral

$$I_2 = \frac{4\pi v_2}{3}\frac{J_1}{v_1}\int_0^\infty \theta\left(sv_1 - \frac{r^{m_1+1}}{m_1+1}\right)(m_2 - m_1) r^{2+m_1-m_2} dr \tag{3.68}$$

$$I_2 = \frac{4\pi v_2}{3}\frac{J_1}{v_1}\int_0^{R_{max}} (m_2 - m_1) r^{2+m_1-m_2} dr \tag{3.69}$$

Taking the sum of I_1 and I_2 we get

$$\frac{\dot{f}_2(s)}{f_2(s)-1} = \frac{4\pi v_2}{3}\frac{J_1}{v_1}R_{max}^{3+m_1-m_2}\left[\frac{3}{3+m_1-m_2}\right] \tag{3.70}$$

We can substitute $m_1 = m_2$ and $v_1 = v_2$ to get $\dot{f}_1$ at $t = s$:

$$\frac{\dot{f}_1(s)}{f_1(s)-1} = \frac{4\pi v_1}{3}\frac{J_1}{v_1}R_{max}^{3} \tag{3.71}$$

Next, we can take the ratio of $\dot{f}_2$ and $\dot{f}_1$, noting that $f_1 = f_2$ at $t = s$:

$$\frac{\dot{f}_2(s)}{\dot{f}_1(s)} = \frac{v_2}{v_1}R_{max}^{m_1-m_2}\left[\frac{3}{3+m_1-m_2}\right] \tag{3.72}$$

$$\frac{\dot{f}_2(s)}{\dot{f}_1(s)} = \frac{v_2}{v_1}v_1^{\frac{m_1-m_2}{m_1+1}}\big(s(m_1+1)\big)^{\frac{m_1-m_2}{m_1+1}}\left[\frac{3}{3+m_1-m_2}\right] \tag{3.73}$$

$$\frac{\dot{f}_2(s)}{\dot{f}_1(s)} = \beta\frac{v_2}{v_1^M} \tag{3.74}$$

Where

$$\beta = \big(s(m_1+1)\big)^{\frac{m_1-m_2}{m_1+1}}\left[\frac{3}{3+m_1-m_2}\right] \tag{3.75}$$

$$M = \frac{m_2+1}{m_1+1} \tag{3.76}$$

Differentiating equation (3.39) with respect to time relates $\dot{f}(t)$ in terms of the heat flow $q(t)$ from DSC, the heat of fusion at temperature T, $\Delta H^{\circ}_{fus}(T)$.

$$\dot{f}(t) = \frac{q(t)}{\Delta H^{\circ}_{fus}(T)} \tag{3.77}$$

Since ΔH°_{fus} is a function of temperature we can now represent equation (3.74) in terms of the heat flow and heat of fusion at temperature T_1, just before the temperature jump ($q_1(s)$ and $\Delta H^{\circ}_{fus}(T_1)$) and the heat flow and heat of fusion at temperature T_2, just after the temperature jump, ($q_2(s)$ and $\Delta H^{\circ}_{fus}(T_2)$).

$$\frac{v_2}{v_1^M} = \frac{q_2(s)\Delta H^{\circ}_{fus}(T_1)}{\beta q_1(s)\Delta H^{\circ}_{fus}(T_2)} \tag{3.78}$$

Now we need the value for k and n, and thus m, for the system at T_2. This leaves us with a system of one unknown.

$$v_2 = \frac{v_1^M q_2(s)\Delta H^{\circ}_{fus}(T_1)}{\beta q_1(s)\Delta H^{\circ}_{fus}(T_2)} \tag{3.79}$$

Continuing in this fashion from T_2 to T_3, or even T_1 to T_3, we can get $v(T_i)$ in terms of $v(T_1)$. Finally, from equation (3.36), the nucleation rate $J(T)$ can be determined in terms of $k(T)$, $v(T)$, and $n(T)$

$$J(T) = \frac{3k(T)n(T)}{4\pi}\left[\frac{3v(T)}{n(T)-1}\right]^{1-n(T)} \tag{3.80}$$

3.3.3 *Two-dimensional analogue*

The following analysis consists of simulating crystal nucleation and growth, as well as the resulting heat release, in two dimensions. The equations in section 3.3.2 apply to three dimensions and should be applied in applications, the following was just for testing and verification of the new theory.

$$Ar^D = \pi R^2 \tag{3.81}$$

$$r = \left(\frac{\pi}{A}R^2\right)^{\frac{1}{D}} \tag{3.82}$$

$$\alpha = \frac{2}{D}\left(\frac{\pi}{A}\right)^{\frac{1}{D}} \tag{3.83}$$

$$\frac{dr}{dt} = \alpha R^{\frac{2}{D}-1}\frac{dR}{dt} \tag{3.84}$$

$$u(R) = \frac{v/\alpha}{R^{\frac{2}{D}-1}} = \frac{v}{R^{\frac{2}{D}-1}} \tag{3.85}$$

Where $v = v_0/\alpha$

Following the same methods for deriving the three-dimensional case, we can derive the two dimensional case for the ratio of $\dot{f}_1$ and $\dot{f}_2$ at $t = s$:

$$\beta_{2D} = \left(s(m_1+1)\right)^{\frac{m_1-m_2}{m_1+1}}\left[\frac{2}{2+m_1-m_2}\right] \tag{3.86}$$

$$M_{2D} = \frac{m_2+1}{m_1+1} \tag{3.87}$$

$$\frac{\dot{f}_2(s)}{\dot{f}_1(s)} = \beta_{2D}\frac{v_2}{v_1^{M_{2D}}} \tag{3.88}$$

Additionally, the two-dimensional Avrami parameters k and n can be re-scaled from the three dimensional version, equation (3.35)

$$n = \frac{m+3}{m+1} \tag{3.89}$$

$$k = \pi \left(\frac{1+m}{3+m}\right) J\big((m+1)v\big)^{\frac{2}{m+1}} \tag{3.90}$$

Thus, the two-dimensional analogue of equation (3.80) is

$$J(T) = \frac{k(T)n(T)}{\pi} \left[\frac{2v(T)}{n(T)-1}\right]^{1-n(T)} \tag{3.91}$$

3.4 Method for Extracting the Relative (and Non-Relative) Growth and Nucleation Rates from Calorimetry Curves

Below we outline a method that can be used to extract the temperature dependent growth rates, nucleation rates, and fractal dimensions during applicable phase change processes involving these phenomena such as crystallization.

3.4.1 *Interpreting and processing Calorimetry Curves*

Suppose we desire to know the temperature dependent growth and nucleation rates for a substance in some temperature interval $[T_0, T_f]$. First partition this interval into N temperature points $T_1, T_2, \dots, T_N$. Next, for each temperature, start the DSC run at some initial temperature above the melting temperature of the substance. From this temperature we rapidly (as fast as possible) decrease the temperature to T_1 and hold it until the substance solidifies and reaches equilibrium. Next, analyze this curve to calculate n_1 and k_1, also noting the time t_1 when half of the available sample solidifies, corresponding roughly to the peak location for the heat release $q_1(t)$. Repeat this for T_2 through T_N and ensure that the mass of each sample is identical. Next, run a series of jumps between these temperature points. For the first jump, run the sample at T_1 just as in the first trial, but now run this trial for t_1 seconds and then rapidly change the temperature to T_2. Continue this same method from

T_2 to T_3 and so on all the way through to T_N. Using the curves $q_i(t)$ generated from the DSC trials, apply equations (3.79) and (3.80) to get $v(T)$ and $J(T)$ in terms of $v(T_1)$. These temperature dependent velocities and nucleation rates can then be normalized to $v(T_1)$ and $J(T_i)$. If desired, one can measure the velocity $u(T_1)$ of a single growing crystal at T_1 (or one of the other temperature points), then, using its radius r and fractal dimension D (measured from DSC), can solve for $v(T_i)$, and thus know the temperature dependent (and radially dependent) velocities and temperature dependent nucleation rates in the temperature range from T_1 to T_N. We have now described a protocol to extract the temperature dependent solid phase growth and nucleation rates from a simple set of DSC curves. Next, we will demonstrate the validity of this protocol via crystal growth simulations.

3.4.2 *Interpreting and processing Calorimetry Curves*

Special care must be given to the DSC curves in experiments, especially near the temperature jump. In practice, one cannot jump infinitely quickly between two temperature points, so the analysis outlined in this chapter is limited to systems where negligible levels of phase change occur during the temperature jump process. This will depend on the sample material at hand, the achievable temperature rates of the DSC device, and the fidelity of the measurements. There will be a heat flow spike during the temperature jump that will need to be trimmed out in post processing by those familiar with the DSC device carrying out the measurements. Once this post processing has been completed, then the analysis from this work may be applied. Additionally, the start time of the entire process starts at the onset of crystallization, and not necessarily the start time the moment the sample reaches T_1. This onset time can be calculated by curve fitting of the DSC curves. Once time zero has been calculated, then proper measurements of s, the time between the onset of crystallization and the temperature jump, can be carried out. Finally, it should be noted that the nucleation rates J in this study are in fact homogeneous nucleation rates. Special care must be taken during the DSC process to ensure minimal contamination from the environment, including the pan itself, to limit heterogeneous nucleation. Additionally, the theory can be used to estimate the number of nucleation sites, and thus heterogeneous nucleation, by considering a step-change in J but not v, and then using equation (3.80), along with the associated change in k to solve for the change in J.

3.5 Time-Dependent Diffusion Limited Aggregation

To test the validity of the mathematical model developed for extracting nucleation rates and growth rates from calorimetric curves, we simulated an environment of growing diffusion limited aggregates to represent a system with complex growth geometry. For computational simplicity we have limited the simulation to two dimensions; however, the simulation may be extended easily into three dimensions. Additionally, the mathematics of the theory is easily generalized into any number of dimensions. An outline of the algorithms used can be found below.

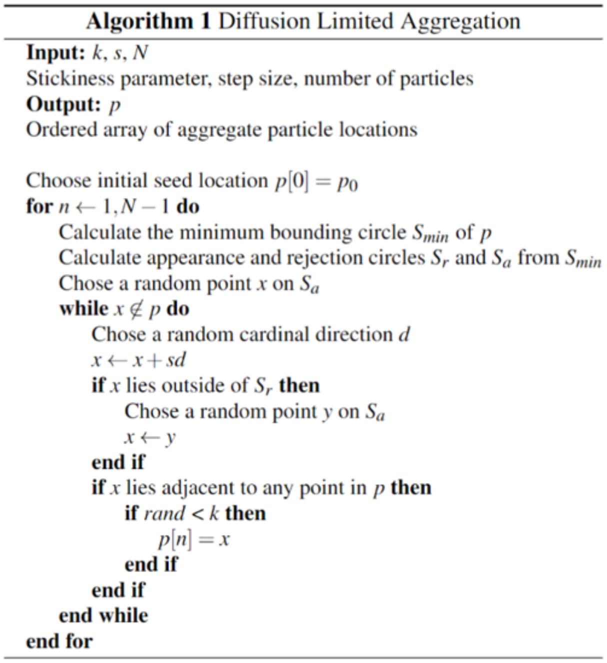

Algorithm 1 Diffusion Limited Aggregation

```
Input: $k$, $s$, $N$
Stickiness parameter, step size, number of particles
Output: $p$
Ordered array of aggregate particle locations

Choose initial seed location $p[0] = p_0$
for $n \leftarrow 1, N-1$ do
    Calculate the minimum bounding circle $S_{min}$ of $p$
    Calculate appearance and rejection circles $S_r$ and $S_a$ from $S_{min}$
    Chose a random point $x$ on $S_a$
    while $x \notin p$ do
        Chose a random cardinal direction $d$
        $x \leftarrow x + sd$
        if $x$ lies outside of $S_r$ then
            Chose a random point $y$ on $S_a$
            $x \leftarrow y$
        end if
        if $x$ lies adjacent to any point in $p$ then
            if $rand < k$ then
                $p[n] = x$
            end if
        end if
    end while
end for
```

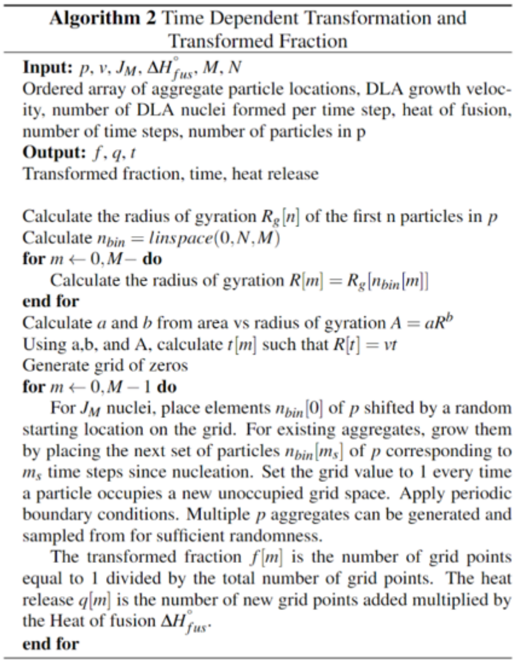

Algorithm 2 Time Dependent Transformation and Transformed Fraction

```
Input: $p$, $v$, $J_M$, $\Delta H^{\circ}_{fus}$, $M$, $N$
Ordered array of aggregate particle locations, DLA growth velocity, number of DLA nuclei formed per time step, heat of fusion, number of time steps, number of particles in p
Output: $f$, $q$, $t$
Transformed fraction, time, heat release

Calculate the radius of gyration $R_g[n]$ of the first n particles in $p$
Calculate $n_{bin} = linspace(0, N, M)$
for $m \leftarrow 0, M-$ do
    Calculate the radius of gyration $R[m] = R_g[n_{bin}[m]]$
end for
Calculate $a$ and $b$ from area vs radius of gyration $A = aR^b$
Using a,b, and A, calculate $t[m]$ such that $R[t] = vt$
Generate grid of zeros
for $m \leftarrow 0, M-1$ do
    For $J_M$ nuclei, place elements $n_{bin}[0]$ of $p$ shifted by a random starting location on the grid. For existing aggregates, grow them by placing the next set of particles $n_{bin}[m_s]$ of $p$ corresponding to $m_s$ time steps since nucleation. Set the grid value to 1 every time a particle occupies a new unoccupied grid space. Apply periodic boundary conditions. Multiple $p$ aggregates can be generated and sampled from for sufficient randomness.
    The transformed fraction $f[m]$ is the number of grid points equal to 1 divided by the total number of grid points. The heat release $q[m]$ is the number of new grid points added multiplied by the Heat of fusion $\Delta H^{\circ}_{fus}$.
end for
```

To test the newly derived theory, we simulated the nucleation and growth of a system of "pseudo-crystals" via a novel time-dependent diffusion limited aggregation (TD-DLA) algorithm, outlined above, based on the classic algorithm and its more computationally efficient derivative from the 1980s.[85,86] First, a series TD-DLA structures were generated which would grow by a specified number of particles at each simulation time step. For each generated aggregate, at each simulation time step, the number of particles added to each aggregate increased the radius of gyration by $v_0\Delta t$. The aggregates were placed randomly on a grid and allowed to grow according to this new time scaling at a constant rate of v_0. Additionally, at each time step, new aggregate nuclei were added, corresponding to a predefined nucleation rate J and time step Δt. For each new particle added to the growing crystal, heat was released according to a prescribed heat of fusion ΔH°_{fus} at the simulation temperature. Intersection between pseudo-crystals was ignored and boundary crossing was handled with periodic boundary conditions. For this simulation, 10 diffusion limited aggregates were grown, each consisting of 50,000 particles. A step size of 5 grid spaces and a stickiness value of 1.0 were chosen to maintain fractal growth but remain spatially dense. Figure 3.1 shows the pseudo-crystals at two time points, demonstrating nuclei formation and how they exhibit fractal, crystal-like growth. The fractal dimension D of the pseudo-crystals increased as the number of particles was added to them, falling between 1.69-1.81. When comparing the simulated transformed fraction to theoretical predictions using equations (3.1) and (3.35), it was determined that the best fit was to take the root-mean-square of the D and apply it to equation (3.35), since there was a distribution of fractal dimensions for the pseudo-crystals composing the transformed phase. We found a near perfect agreement between the predicted and actual transformed fraction, with an $R^2 =$ .999, shown in Figure 3.2.

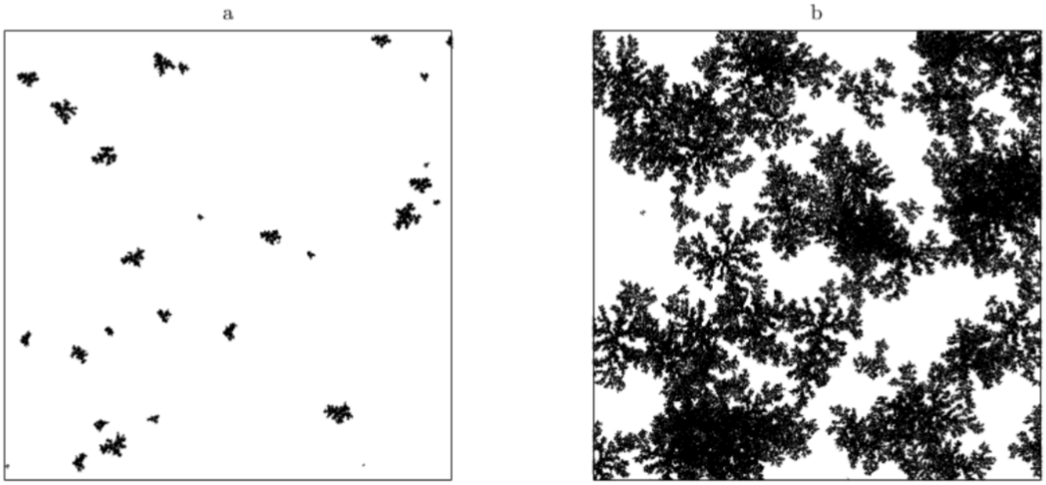

Figure 3.1. An image of the crystallization process for the simulation of nucleating and growing diffusion limited aggregates at $t^* = .12$ (a) and $t^* = .48$ (b)

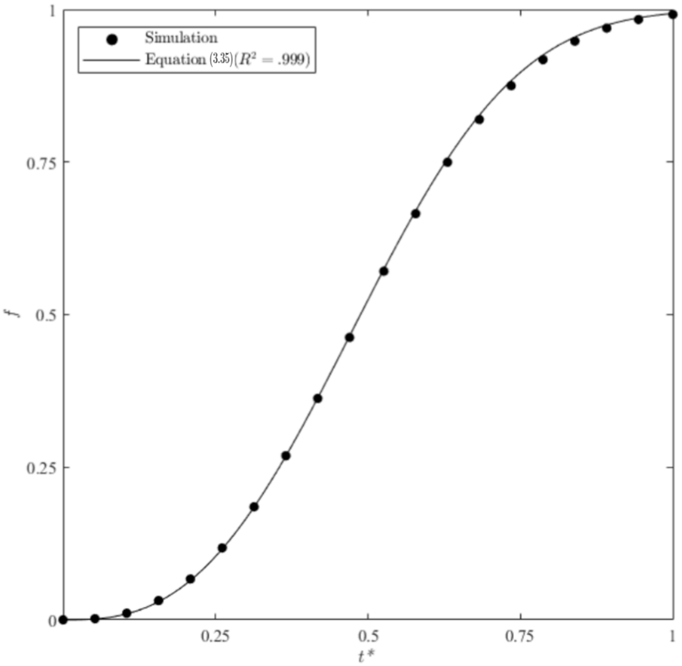

Figure 3.2. Transformed fraction f vs time t^* for isothermal crystallization from the diffusion limited aggregate simulation and the model of phase change from equation (3.35).

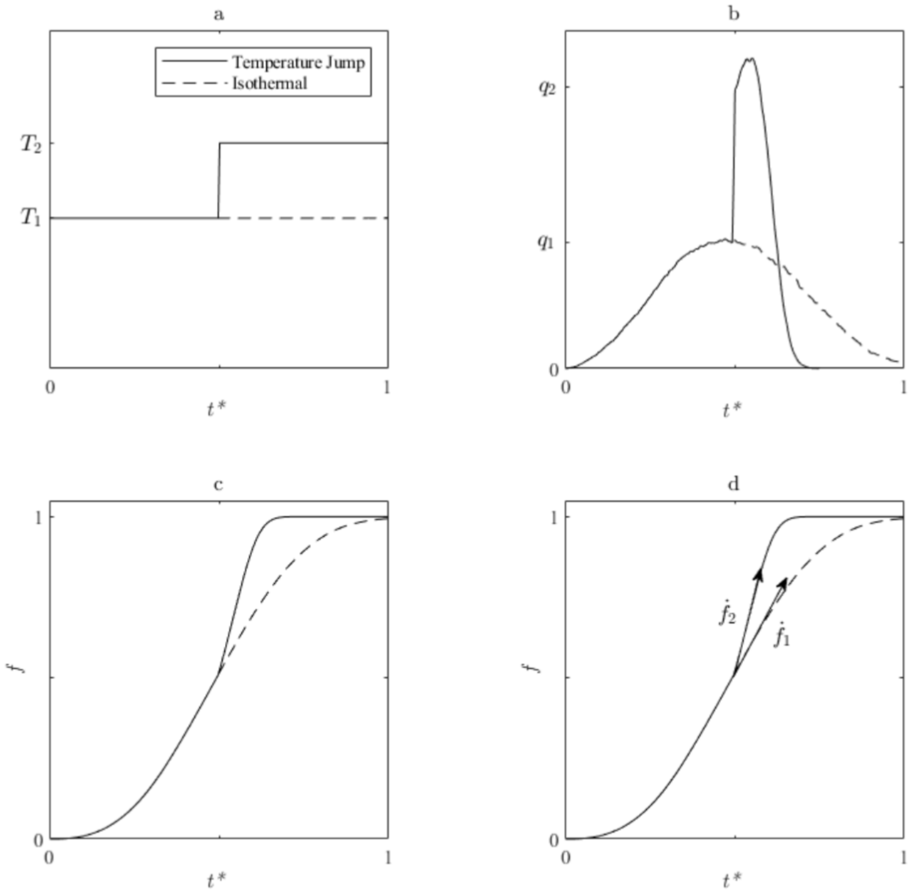

Figure 3.3. TD-DLA nucleation and growth simulation results from both an isothermal crystallization process (constant properties) as well as a crystallization process resulting from a temperature jump (step change in properties) at $t^* = 0.5$ between T_1 and T_2. (a) Temperature T vs time t^* for simulations of crystal growth for the isothermal case and the temperature jump case. (b) Heat release q vs time t^* for both the isothermal and temperature jump TD-DLA growth simulations. The change in heat release from q_1 to q_2 is related to the change in the following temperature dependent properties: growth rate, nucleation rate, heat of fusion, fractal dimension, and pre-exponential factor. The values for these properties at temperatures T_1 and T_2 are given in Table 3.3. (c) Transformed fraction f vs time t^* for the isothermal and temperature jump TD-DLA growth simulations. (d) Figure 3.3(c) is shown with the time derivatives $\dot{f}_1$ (Isothermal case) and $\dot{f}_2$ (Temperature jump case) at the jump time $t^* = 0.5$. This shows how the time derivative of transformed fraction changes from before and after a temperature jump between isothermal holds. The ratio between $\dot{f}_1$ and $\dot{f}_2$ infers information about the ratio between the growth velocities, and thus nucleation rates, at the two temperatures T_1 and T_2.

Table 3.1. Values of the actual vs predicted growth rate v, nucleation rate J, and fractal dimension D at temperatures T_1 and T_2. The values of the parameters are given in dimensionless units.

Parameters	T_1	$T_1(predicted)$	T_2	$T_2(predicted)$
v	156.5	N/A	313	316.4
J	.000250	.000267	.0025	.0026
D	1.69-1.81	1.734	1.69-1.81	1.734

Table 3.2. The extracted Avrami parameters k and n, heat flow q_s immediately before and after the temperature jump, and the heat of fusion ΔH°_{fus} at T_1 and T_2. The uncertainty shown represents 95% confidence bounds on the parameters. The values of the parameters are given in dimensionless units.

Parameters	T_1	T_2
k	$4.842 \pm .022$	161.6 ± 1.700
n	$2.734 \pm .007$	$2.734 \pm .006$
q_s	4.120	1.854
ΔH°_{fus}	1.0	1.1

We then sought to test the validity and applicability of equations (3.74) and (3.79), which relate the change in the temperature dependent fractal dimension, growth velocity, and nucleation rate to the change in heat released by the system. This required us to simulate the growth of TD-DLA pseudo-crystals under conditions emulating a step-change in temperature. To accomplish this, we defined the system at two temperatures, T_1 and T_2, with associated temperature dependent growth rates u_1 and u_2 (thus v_1 and v_2), nucleation rates J_1 and J_2, and heat of fusions $\Delta H^{\circ}_{fus,1}$ and $\Delta H^{\circ}_{fus,2}$. The values for these parameters are given in Table 3.1 and Table 3.2. During the simulation, the transformed fraction was calculated so that when half of the system was transformed, the temperature was changed from T_1 to T_2, changing the growth velocity by a factor of two and the nucleation rate by an order of magnitude. The temperature profiles and associated heat release curves are shown in Figure 3.3(a) and (b) respectively, showing the difference between the case with a temperature jump, and one simply held isothermally. Integrating these heat release curves yielded the transformed fraction, shown in Figure 3.3(c) and (d). The analysis of these heat release curves yielded nearly identical velocities and nucleation rates to those used in the simulation, shown in Table 3.1. It is important to note that the values of the calculated nucleation and growth rates are in terms of v_1, which means we know the relative change in these values and not their absolute value. To determine the absolute values, one needs only one data point, v_1 or J_1 will suffice, to determine the values of these parameters at all temperatures T_i, given a series of heat curves resulting from jumps between T_1 and T_2, T_2 and T_3, etc. After testing the new theory on simulated TD-DLA pseudo-crystals, we have confidence that implementation of this method for extracting relative growth rates and nucleation rates from a system undergoing liquid-solid phase change will quantitatively yield the true growth velocities, nucleation rates, and growth geometries in that system relative to some baseline. This is only contingent on the accuracy of the measurements in the first place, and that the DSC instrument can maintain temperature rates sufficiently faster than the phase change at hand.

3.5 Gas phase PDE and the Rayleigh–Plesset Equation

We can extend the theory presented in earlier sections to the gas phase, that is, considering gas nucleating and growing from a liquid. This complicates the previous problem by allowing the density of the nucleated phase to vary, since the gas is compressible. We start by considering Figure 3.4 below alongside the introduction of the classic Rayleigh-Plesset equation, (3.92) and (3.93), which is an ordinary differential equation that governs the growth dynamics of bubbles in an incompressible fluid.[87,88]

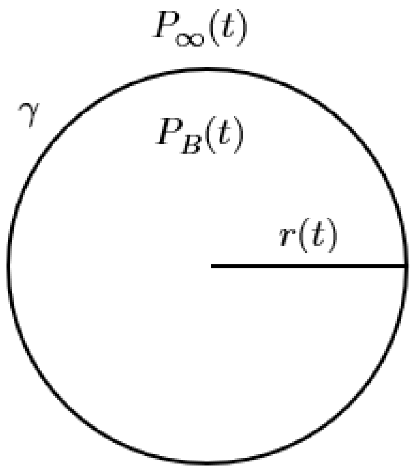

Figure 3.4. Schematic of a bubble subject to pressure and surface tension.

$$r\frac{d^2r}{dt^2}+\frac{3}{2}\left(\frac{dr}{dt}\right)^2+4\frac{\mu_L}{\rho_L}\frac{dr}{dt}+\frac{2\gamma}{\rho_L r}+\frac{P(t)}{\rho_L}=0 \tag{3.92}$$

$$P(t,r)=P_\infty(t)-P_B(t,r) \tag{3.93}$$

Where ρ_L is the surrounding liquid density, P_∞ *and* P_B are the exterior and interior bubble pressures. γ is the liquid surface tension, μ_L is the liquid dynamic viscosity.

Now let us consider the PDE described by equations (2.72) and (2.73) but extended into an additional dimension described by P in equation (5.93). We now have a phase size distribution that is a function of both the pressure difference across the local gas bubble, as well as the size of the bubble itself. We must have two dimensions here as two bubbles may have identical radii but different pressure differences across their boundaries, which will lead to different growth dynamics. Extending equation (2.72) into this new two dimensional domain gives:

$$\frac{\partial\rho}{\partial t}+\frac{\partial}{\partial r}(u\rho)+\frac{\partial}{\partial P}(v\rho)=0 \tag{3.94}$$

$$v=\frac{dP}{dt} \tag{3.95}$$

$$u=\frac{dr}{dt} \tag{3.96}$$

Where ρ, u, v are functions of $r, t, P(t,r)$ and N is the number of bubble spheres per unit volume that have radii between r_1 and r_2 and pressures between P_1 and P_2.

$$N = \int_{r_1}^{r_2} \int_{P_1}^{P_2} \rho(r,t,P) dP dr \tag{3.97}$$

Now the initial condition is the essentially the same as before, with D_0 is the initial distribution of phase as a function of r and P:

$$\rho\big(r, 0, P_0(r)\big) \quad = D_0\big(r, P_0(r)\big) \tag{3.98}$$

To determine the boundary conditions for this PDE we consider that $I(r,t)$ gives us the density distribution of radii of the bubbles disregarding pressure. This is key, because at the moment of nucleation, there should only be one P values for all the bubbles at that given time. Thus, at the point $r \; = \; r_0$ we have

$$I(r_0, t) = \int_{-\infty}^{\infty} \rho(r_0, t, P) dP \tag{3.99}$$

$$I(r_0, t) = \int_{-\infty}^{\infty} g(r_0, t, P) \delta\big(P(t)\big) dP \tag{3.100}$$

$$I(r_0, t) = \frac{J(t)}{u(t)} \tag{3.101}$$

$$\frac{J(t,P)}{u(t)} = \int_{-\infty}^{\infty} g(r_0, t, P) \delta\big(P(t)\big) dP \tag{3.102}$$

$$g(r_0, t, P) = \frac{J(t,P)}{u(t)} \tag{3.103}$$

$$\rho(r_0, t, P) = \frac{J(t,P)}{u(t)} \delta\big(P(t)\big) \tag{3.104}$$

So, the compete equations are

$$\frac{\partial \rho}{\partial t} + \frac{\partial}{\partial r}(u\rho) + \frac{\partial}{\partial P}(v\rho) = 0 \tag{3.94}$$

$$\rho(r_0, t, P) = \frac{J(t,P)}{u(t)} \delta\big(P(t, r_0)\big) \tag{3.105}$$

$$\rho(r, 0, P) \quad = D_0(r, P) \tag{3.98}$$

$$r\frac{d^2r}{dt^2}+\frac{3}{2}\left(\frac{dr}{dt}\right)^2+4\frac{\mu_L}{\rho_L}\frac{dr}{dt}+\frac{2\gamma}{\rho_L r}+\frac{P(t)}{\rho_L}=0 \tag{3.92}$$

$$P(t,r)=P_\infty(t)-P_B(t,r) \tag{3.93}$$

In the case of driven growth due to mass transfer across the bubble boundary we have, where m is the mass of gas inside the bubble.

$$P_B(t,r)=\frac{m}{V}\overline{R}T \tag{3.106}$$

$$P_B(t,r)=\frac{4m}{3\pi r^3}\overline{R}T \tag{3.107}$$

If we consider mass flux from the liquid to the bubble, we have.

$$\frac{dm}{dt}=f(P_g,P_B) \tag{3.108}$$

Where P_g is the partial pressure of gas in the liquid and f is some flux function determining the flux of gas across the bubble boundary. We outline a general solution procedure for this problem but leave the in depth analysis of these equations to future research, as it is beyond the scope of this thesis in its current form.

A rough solution can be determined by first solving the bubble radius as a function of time and pressure by solving the Rayleigh-Plesset. This will give closed loop curves on the rP plane for different initial conditions. Then, equation (3.94) can be converted into a one dimensional problem by considering it only on a single closed curve solution to the Rayleigh-Plesset equation. This PDE can then be solved in the same fashion as in chapter 2, for each closed curve. The superposition of these solutions across all closed curves will give the phase size-density distribution $\rho(t,r,P)$.

3.6 Conclusion

In this chapter we described the theory linking a system undergoing phase change, its nucleation rate, growth rate, and growth geometry for arbitrary geometries. Next, we described a method whereby utilizing the theory presented, we were able to devise a protocol for extracting relative growth rates, nucleation rates, and growth geometries from calorimetric curves. We then simulated an arbitrary crystallization event by simulating time-dependent diffusion limited aggregates nucleating and growing in a periodic system. We then showed that applying our devised protocol we were able to recover the nucleation rate, growth rate, and geometry. We will expand on applications in the next chapter by analyzing rapid crystallization in low concentration cryoprotective agents (CPAs) to determine the critical cooling and critical warming rates of various CPAs.

ADAPTED FROM

Manuscript in preparation for publication

AKNOWLEDGMENTS

This work was supported by the National Science Foundation, Grant No. 1941543, NSF Engineering Research Center for Advanced Technologies for Preservation of Biological Systems (ATP-Bio).

Chapter 4

Analyzing Glass Forming Tendency of Cryoprotectant Solutions Via Laser Calorimetry

4.1 Introduction

Cryopreservation allows for long-term storage because the chemical activity normally associated with functioning cells effectively ceases at low cryogenic storage temperatures such as liquid nitrogen boiling point, or -196 ºC. In fact, the only source of damage to biological material at this temperature is from direct ionization from background radiation, making storage durations on the order of millennia possible.[9] Under normal circumstances, cooling biological materials to these temperatures leads to widespread cell death due to the damaging effects of ice crystallization; however, cryoprotective agents (CPAs) can be introduced to mitigate some of these effects. These CPAs work to preserve biomaterials by modulating the viscosity, glass and melting transition temperatures, and other physical properties to limit the scale and scope of ice formation.[34,89,90] Ice formation, both intracellular and extracellular, can lead to cellular damage and death, with intracellular ice formation linked directly to cell membrane damage.[91–94] However, many CPAs are not well tolerated by cells, and so proper cryopreservation requires achieving a delicate balance between the CPA toxicity and the damage caused by ice formation. Toxic effects have been shown to occur at different concentrations for different CPAs, and these effects also vary widely between cell and tissue types.[95] In general, high-concentration CPAs exhibit strong ice-suppressing properties but unfortunately have been shown to be more cytotoxic than low-concentration CPAs and are capable of damaging or destroying cells via osmotic affects.[96,97] This limitation suggests that it is important to use the lowest possible concentration of CPA to prevent toxicity to the biological system, which thereby necessitates high rates of cooling and warming. For microliter systems, one common approach is to bring the system to a vitrified state, transforming the biomaterial into an amorphous glass while eliminating the damage caused by ice crystal formation and its accompanying osmotic shock. Slow freezing is an alternative approach to systems at this scale, where by cooling slowly, ice is restricted to the extracellular space; however, this is often accompanied by larger osmotic gradients and volume changes vs vitrification and will not be further pursued here.[98]

The successful vitrification of biological systems in microliter-sized droplets is dependent on the concentration of CPA used, with each concentration having a corresponding critical cooling rate (CCR) needed to achieve vitrification on cooling and critical warming rate (CWR) to avoid devitrification on warming. To limit the toxic effects of CPAs while also mitigating ice formation at the cooling rates (~10^4 °C/min) experienced at this scale, microliter-scale cryopreservation requires CPA concentrations of roughly 30 wt%, which can vary by as much as 10 wt% depending on the CPA used. The CWRs at these low concentrations can be several orders of magnitude larger than the CCRs, requiring warming rates in excess of 10^6 °C/min. This difference largely occurs because the temperature at which peak crystal growth occurs is near the melting temperature, whereas the temperature of peak nucleation occurs well below the melting point. This means that during cooling, one passes through the temperature window in which crystal growth is maximal before much nucleation has occurred, whereas during warming, the majority of nuclei form prior to the period of maximal crystal growth, causing much more ice to form relative to during cooling at the same rate. Additionally, to measure the CWR, one must first cool the sample down. This inherently leads to some crystallization and nucleation, effectively seeding and boosting ice growth once warming commences and thereby inflating the CWR measurement. Current practice is to minimize this affect by cooling at rates far above the CCR, but this practice works in only the high-concentration regime. Note that the elimination of all ice crystallization during cooling or warming is impossible without infinite temperature rates or infinite time, and in the absence of either of these, some fraction of the sample will crystalize regardless of the cooling or warming rate.[45–47,99] Thus, instead of using ideal vitrification as a marker for success, it is often more practical to use “apparent vitrification”. An ice fraction threshold commonly used to define apparent vitrification is less than 0.2% ice by mass.[35] Throughout the remainder of this paper, use of the word *vitrification* implies *apparent vitrification.* Understanding the relationship between the cryoprotectant concentration and ice formation is paramount for successful cryopreservation and rewarming.

Currently, determining the necessary CCRs and CWRs of CPAs, especially in the low-concentration regime, remains a challenge, with a summary of the current techniques in Table 4.1. For instance, conventional CCR and CWR measurements have relied on differential scanning calorimetry (DSC), but conventional machines can only attain rates up to roughly 100 °C/min in the cryogenic range, though DSC has the advantage of quantitative ice detection.[100–102] A promising new technology, termed nanocalorimetry, being developed at several institutions including the National Institute of Standards and Technology may allow DSC to be carried out at millions of degrees per minute for extremely small samples.[103,104] Unfortunately, to get rates of millions of degrees per minute requires samples on the order of a picolitre, which without special care, will quickly evaporate (especially for CPAs containing volatiles like alcohols), necessitating precise environmental control to measure CWR of CPAs with nanocalorimetry above 10^6 °C/min.[105,106]

Table 4.1. Current methods for analyzing CWR with rates, benefits, and drawbacks

	CONVENTIONAL DSC	**CONVECTIVE WARMING**	**NANO-DSC**	**LASER CALORIMETRY**
Cooling Rates (C/min)	0.1-50	10^3-10^5	10^3-10^7	10^3-10^5
Warming Rates (C/min)	0.1-100	10^3-10^6	10^3-10^7	10^2-10^{8+}
Sample Size	1 - 10 μL	1 nL - 100 μL	1 pL - 1 nL	1 nL - 100 μL
Benefits	Highly sensitive. Quantitative phase change detection.	Low cost. Simple implementation.	Highly sensitive. Quantitative phase change detection. Large rate regime.	Large rate regime and arbitrarily large warming rates. Volumetric warming.
Drawbacks	Slow rates, especially on cooling. Difficult to maintain cooling rates in the cryogenic temperature range.	Volume limited rates. Qualitative ice detection.	Expensive. Evaporation. Appreciable surface nucleation.	Qualitative ice detection. Limited by achievable cooling rate.

The volume dependence of nucleation in water droplets near the homogeneous nucleation temperature, primarily due to surface nucleation effects on the droplet, has been shown to become significant for droplet diameters less than 50 microns and to dominate for diameters of less than 10 microns.[107] This means even if the barriers to evaporation are overcome for nanocalorimetry, droplets of less than 100 pL will experience appreciable surface nucleation, thus any CWR measurements will not be meaningful when applied to larger systems. It remains unclear the total contribution to crystallization surface nucleation has when cooling over a large temperature regime, as well as in CPAs.

An additional method used to measure CCR and CWR is by directly quenching a droplet with a thermocouple inside it into liquid nitrogen for cooling or hot oil for warming, then imaging the subsequent process to determine if ice formation occurred. CWRs of up to 10^6 °C/min have been measured via direct quenching into hot oil.[33] CCR on the other hand have not been directly measured much above 10^5 °C/min due to a combination of factors making the achievable rates lower than convective warming. First, convective cooling involves quenching into a cold fluid, typically liquid nitrogen, so the maximum temperature difference between the bath and sample is about 200°C whereas convective warming can have temperature differences of 400°C or larger using hot oil. Additionally, quenching into liquid nitrogen introduces the Leidenfrost effect, where upon quenching a thin layer of liquid nitrogen vapor blankets the sample and reduces heat transfer, and thus cooling rate.[108] Depending on the size and temperature of the sample being plunged heat transfer coefficients for liquid nitrogen vary from less than 1000 W/(m^2 °C) up to 10^6 W/(m^2 °C).[109,110] Measuring CWRs above 10^5 °C/min requires nanoliter-scale droplet volumes, which in turn require extremely fine-gauge thermocouples to measure the warming rate without introducing uncertainty due to the thermal mass of the thermocouple. Due to these problems, CWRs in excess of 10^6 °C/min have yet to be measured; however, with the advent of the laser nanowarming of small specimens (cells, embryos, and larvae) in dilute CPAs, calorimetric data in this regime are becoming increasingly important.[111,112] The use of a high-power laser and highly absorbent nanoparticles has been demonstrated to attain uniform warming rates in excess of 10^7 °C/min in microliter-scale droplets, providing an excellent framework upon which an ultra-rapid laser calorimeter can be used to detect the CWRs of cryoprotectants in regimes previously unattainable, thereby allowing for the decoupling of cooling rate and CWR measurements.

In this study, a high-power pulsed laser, high-speed camera, and gold nanoparticles (GNPs) were used to create a laser calorimeter to measure the CWRs of low concentrations of propylene glycol (PG), trehalose, and glycerol and mixtures of glycerol and PG with trehalose in the 10^6-10^7 °C/min warming rate range (20-40 wt%). CCRs were also measured via direct quenching to determine how the relationship between CCR and CWR changes with CPA concentration. In addition to these experiments, a theory for determining the CCR and CWR of mixtures of CPAs was developed and tested. To help understand the thermal gradients and warming rates measured by laser calorimetry, Monte Carlo (MC) simulations of photon transport and finite element heat transfer modeling were carried out.

4.2 Model development

A vast amount of experimental evidence indicates that the CCR and CWR of a CPA have an exponential relationship with concentration.[37,69] By taking advantage of this property, we can create a model that describes what happens to CCR or CWR of mixtures of CPAs, given knowledge of the CPAs in the mixture. For brevity, only the CCR will be considered in the following analysis, though it is also valid for CWR as well.

4.2.1 *Single species CCR estimation*

Since CCR depends exponentially on concentration, it can be expressed in the form

$$R = Ae^{-\alpha c} \tag{4.1}$$

where A and α are constants, c is the weight fraction concentration, and R is the CCR. In principle, the CCRs of all CPAs should have identical A values since at zero concentration they are all identically water. Consider a mixture of two CPAs at concentrations c_1 and c_2 whose individual CCRs can be expressed by the equations

$$R_1 = Ae^{-\alpha_1 c_1}, \qquad R_2 = Ae^{-\alpha_2 c_2} \tag{4.2}$$

4.2.2 *Two-species CCR estimation*

The CCR of the mixture of these two CPAs must take the form of $R_{1,2}$ equation (4.3), which is further discussed in the supplemental material. This reduces to R_1 and R_2 for $c_2 = 0$ and $c_1 = 0$ respectively, where f is some unknown function

$$R_{1,2} = Ae^{-\alpha_1 c_1} e^{-\alpha_2 c_2} e^{-f(\alpha_1,\alpha_2,c_1,c_2)c_1 c_2} \tag{4.3}$$

The function f cannot be determined a priori; however, experimental evidence may provide insights into its functional form. The relationship between exponential factors, shown in Figure 4.13 for the CCR, was determined to be a linear average of their respective concentrations based on analysis of the data in Figure 4.8 and Figure 4.9. Since the exponential factors of a unary trehalose solution and a unary glycerol solution are almost identical, the exponential factor of glycerol-trehalose mixtures has almost no concentration dependence. Using this linear relationship, we arrive at a functional form for f and thus an expression for $R_{1,2}$.

$$f = \frac{(\alpha_2 - \alpha_1)}{\chi_1} \tag{4.4}$$

$$R_{1,2} = Ae^{-\alpha_1 c_1} e^{-\alpha_2 c_2} e^{-\frac{\alpha_2 - \alpha_1}{\chi_1} c_1 c_2} \tag{4.5}$$

In this equation, χ_1 is the concentration weight fraction for species 1 at saturation in water. For trehalose, this value is roughly 0.4, corresponding to a solubility of 69g per 100g of water.

2.3 Multi-species CCR estimation

From this expression, we can apply the same argument for a mixture of n CPAs.

$$R_n(c_1, \dots, c_n) = A \prod_{i=1}^{n} e^{(-\alpha_i c_i)} \prod_{1 \leq i < j \leq n} e^{-\frac{\alpha_j - \alpha_i}{\chi_i} c_i c_j} \tag{4.6}$$

In summary, equation (4.6) can be applied to both CCR and CWR experimental results in single and mixture CPA solutions. Additional discussion for when the leading preexponential constant A varies between CPAs can be found in the section 4.4.

4.3 Methods for CCR and CWR Attainment

4.3.1 *Critical cooling rate measurements*

Two CPA mixtures were considered for this study: a PG-trehalose-water solution and a glycerol-trehalose-water solution, and the concentration fractions of the individual CPA chemicals were varied. A cryotop consisting of an 80-µm-thick strip of polypropylene adhered to a 5-mm-diameter wooden rod was constructed to hold the sample.[113,114] Next, a 25-µm-diameter Type T unsheathed fine-gauge thermocouple was fastened to the cryotop with cyanoacrylate so that the junction of the thermocouple resided near the leading edge of the cryotop. For data acquisition, a StingRay DS1M12 from EasySync Ltd connected the thermocouple directly to a laptop. This method of thermocouple data acquisition with a cryotop builds directly from methods outlined in Kleinhans 2010.[115] The thermocouple-cryotop assembly was then attached to a mechanical jig that controlled its height. This design feature allowed for the controlled plunging of the sample into liquid nitrogen (LN_2), thereby increasing the repeatability between trials, shown in Figure 4.1. A micropipette was used to place a droplet of the CPA solution on the cryotop so that the thermocouple junction was directly in the center of the hemispherical droplet. Then, the droplet was plunged into LN_2, allowed to reach thermal equilibrium with the LN_2, and then raised up to assess ice formation by visual assay. Samples with any traces of ice were classified as not vitrified. Figure 4.2 provides a demonstration of the vitrification criterion used. The temperature data gathered were then labeled as either vitrified or not vitrified.

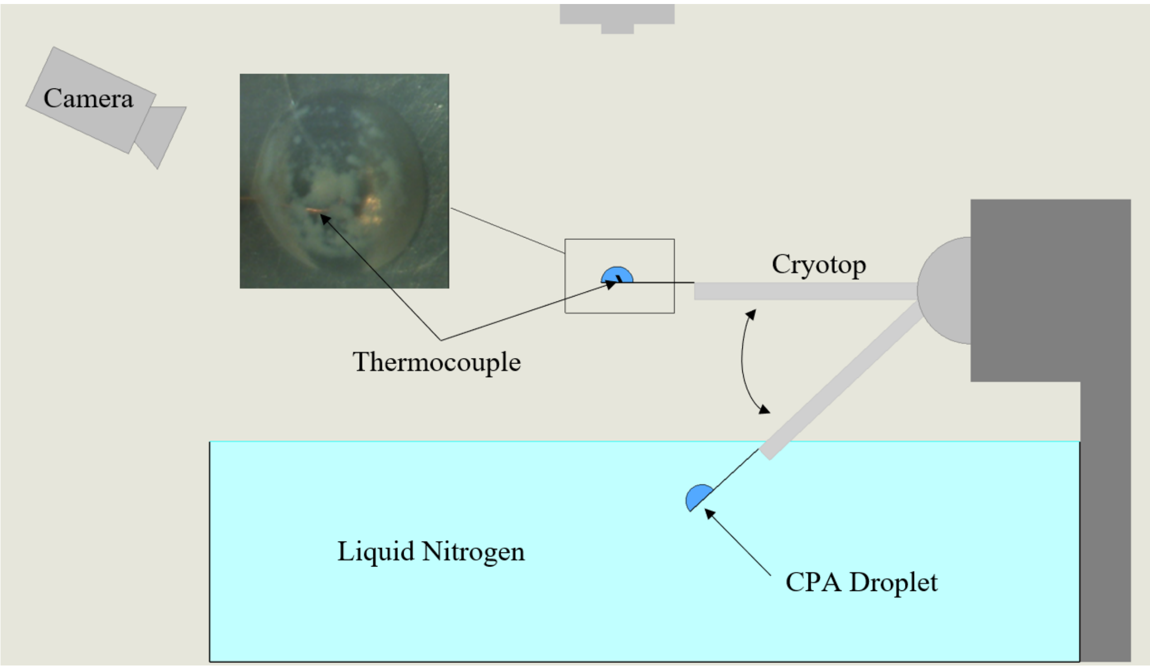

Figure 4.1. Schematic of CCR experimental setup

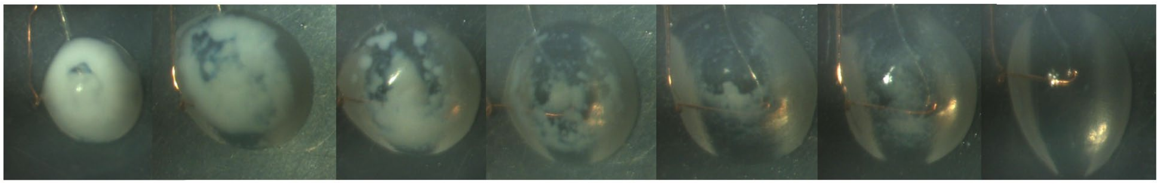

Figure 4.2. Visual assay to assess ice formation. Images show a gradually increasing concentration of PG from left to right and its effect on the amount of ice detected. The right-most image is the only image we classified as vitrified.

Temperature data were then exported to MATLAB for analysis. A best fit line of temperatures between -20 °C and -190 °C was used to determine the cooling rate in the droplet, as shown in Figure 4.4. The temperature profiles were approximately linear in this range of temperatures for droplets smaller than 10 µL. The cooling rate was controlled in this experiment through volume modulation of the droplet, shown in Figure 4.5. There are some differences between the measured data in Figure 4.5 and the data gathered in this study. Wowk and Baudot used DSC to extract kinetic parameters to estimate the CCRs using Boutron's model P. Boutron, Cryobiology 23, 88–102 (1986). Warkentin uses x ray diffraction of quartz capillary tubes which show high variability in CCR. Their data also follows roughly the same trend as ours but is offset. This may be due to several factors. First, they used XRD to validate vitrification, which may be less sensitive than visual detection, making their measurements lower than ours. Additionally, they had difficulty measuring cooling rate as it was not linear for many of their samples, due to film vs nucleate boiling during cooling in liquid propane and liquid nitrogen, likely causing the large uncertainty in measurement.

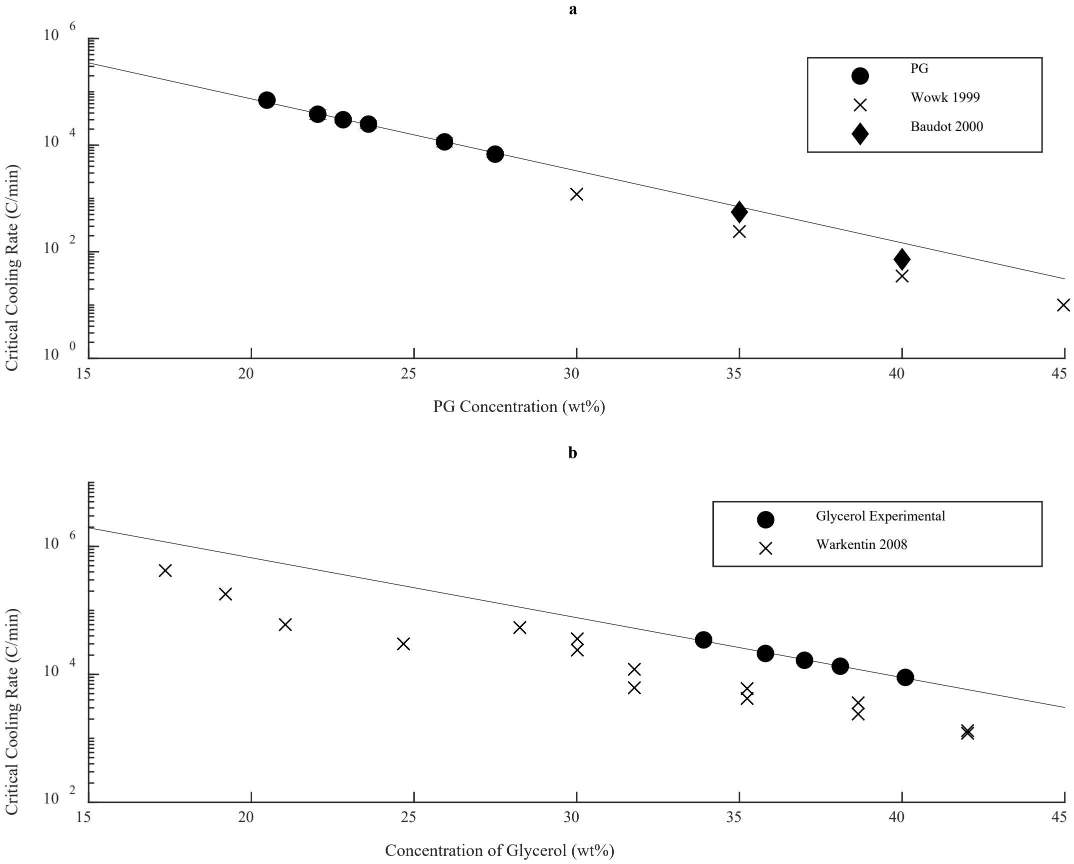

Figure 4.3. CCRs attained via measurement by thermocouple and LN_2 quenching compared with the critical cooling data available in the literature for PG (a) and glycerol (b). Error bars represent the difference between the lowest measured cooling rate that achieved vitrification and the largest measured cooling rate that did not achieve vitrification.

To determine the CCRs of the CPAs, the following technique was employed. First, a 5-µL droplet of CPA was plunged into LN_2, and its cooling rate was recorded. Droplets larger than 5 µL gave inconsistent cooling rates due to cracking, so the starting volume for the CCR experiments was limited to 5 µL. If this solution vitrified, the CPA concentration was too high for the CCR to be measured by this particular method, and the CPA concentration was simply lowered until the 5 µL droplet did not vitrify. The droplet volume was then decreased until no ice could be visually detected after plunging the droplet in LN_2. The cooling rate measured at this point was called the CCR. Using this method, CCRs between 5,000 and 100,000 °C/min were attainable.

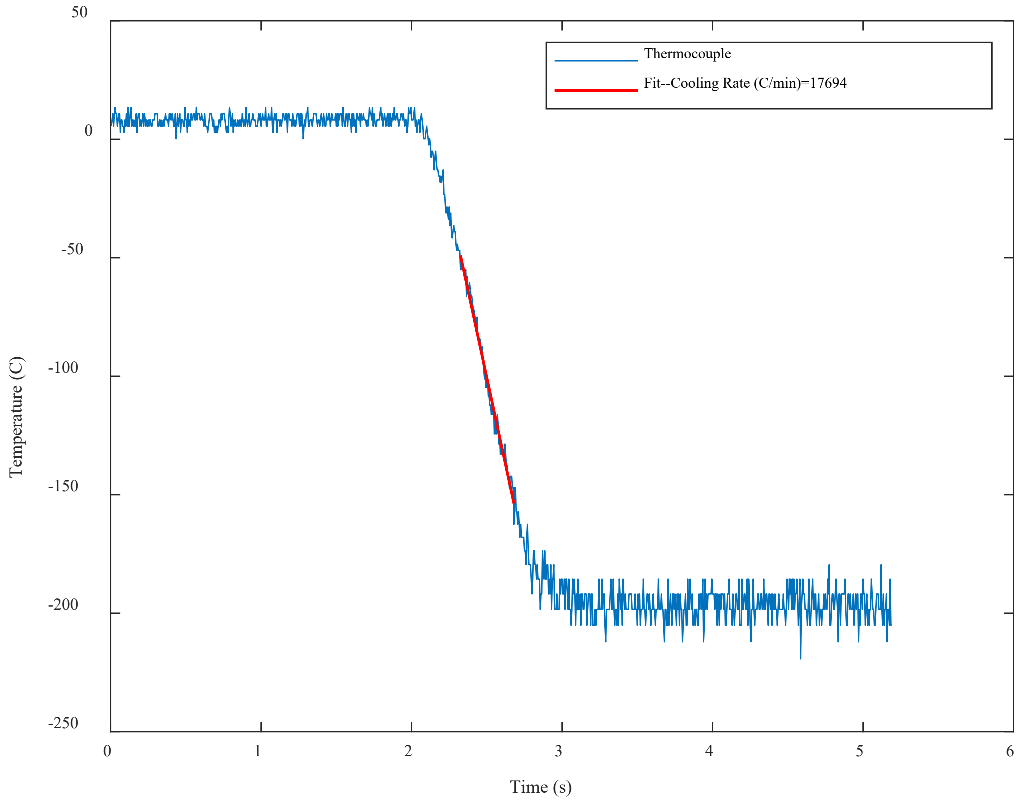

Figure 4.4. Thermocouple data obtained from LN_2 quenching of a 0.9-µL droplet of PG.

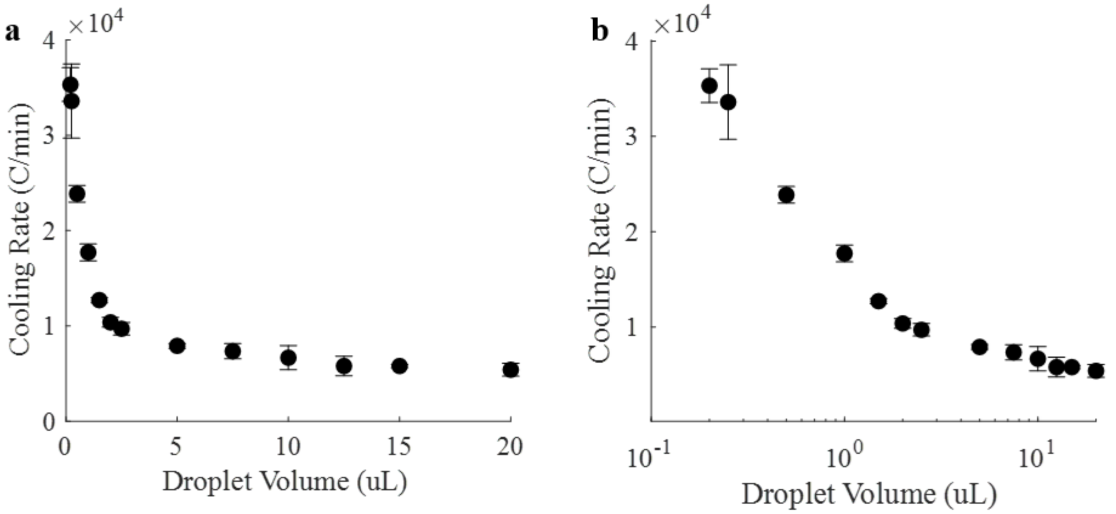

Figure 4.5. Dependence of the cooling rate on droplet volume for cryotop quenching into LN$_2$, (a) linear and (b) log-scale concentration.

4.3.2 *Laser calorimetry*

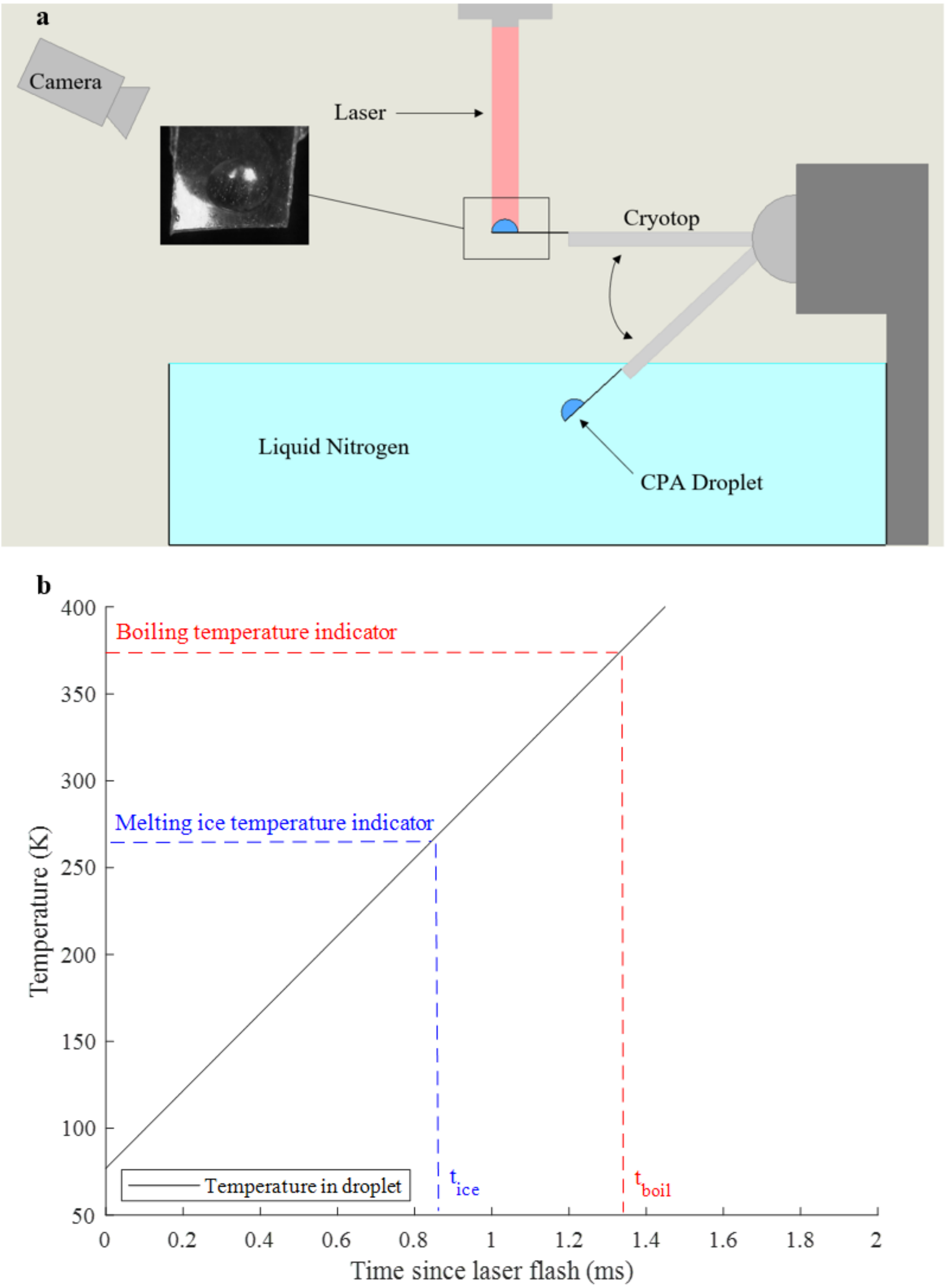

Figure 4.6 (a) Schematic of Laser Warming. (b) Plot showing how warming rates are calculated from temperature indicators in high-speed videos of laser warming.

Microliter droplets (0.1-0.5 µL) of a CPA and gold nanorod (GNR) solution were placed on the tip of a cryotop and plunged into LN_2. Droplet solutions were chosen so that the cooling rate of plunging was sufficiently above the CCR of the CPA to minimize crystallization during cooling. Next, a 2-mm-diameter unpolarized 1064 nm pulse laser with a peak power of 10 kW (LaserStar, Model Number 585-986-080) was fired vertically on the top of the hemispherical droplet, initiating plasmonic heating facilitated by the presence of GNRs, allowing for ultra-rapid warming of the droplet. The concentration dependent absorption coefficient for the GNR solution was measured via UV-Vis spectroscopy, see Figure 4.17. From this data, the GNR concentration (1.65×10^{16} - 6.83×10^{16} nps/m^3) was chosen so that the absorption coefficient was between 0.5 cm^{-1} and 2.0 cm^{-1}, corresponding to a transmittance of 80-95% through the microliter-(mm) scale droplets assuming Beer's law, allowing for warming rates between 4.0×10^5 and 10^7 °C/min given the energy of the laser,[116] Since the transmittance was large, there was negligible attenuation of the laser throughout the droplet, thus leading to relatively uniform warming rates. During warming, a high-speed camera (MEMRECAM Qv1) with an adjustable lens (Nikon ED 200 mm 1:4D) was used to record the changes in the droplet. Frame rates between 4,000 and 15,000 frames per second (fps) were used over the course of this study. The maximum frame rate of the camera is 84,000 fps, which corresponds to a maximum detectable rate on the order of 10^8 ºC/min, assuming 10 frames are needed to resolve the warming rate. Dynamic ice detection was performed by visually identifying the occurrence of ice (i.e., a white opaque regions) in droplets using high-speed video footage. Image processing tools that adjusted the contrast aided in the detection of ice near the visual limit of detection. Figure 4.7 shows the difference between a vitrified droplet and one with ice during warming. Due to the high-speed camera's ability to detect some near infrared light, there was a bright flash at the moment the laser fired. This flash allowed for the synchronization of the high-speed camera and laser pulse, thus determining the exact time the laser fired.

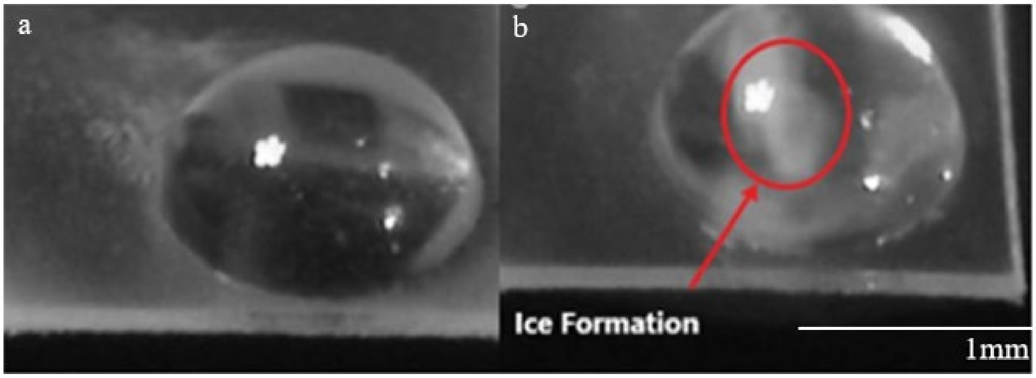

Figure 4.7. The figure above shows a vitrified droplet (a) and a droplet mid-pulse during laser warming (b). The opaque areas in the middle of the droplet on the right correspond to ice formation during warming, indicating that the warming rate was lower than the CWR. The opaque areas in the vitrified droplet on the left are reflected images of the laser chamber interior. One characteristic of the nucleated ice is that it moves within the droplet during laser warming (see videos of laser warming in the supplemental material), providing a distinction between these artifacts and ice.

The CWR of the CPA was detemined by modulating the laser energy in the following fashion. First, the droplet was warmed at the lowest laser setting (4.92×10^{7} W/m^{3}) and assessed for ice. If no ice was detected, the concentration of GNRs in the droplet was decreased until a concentration that led to ice formation was identified. Once a sufficiently low GNR concentration that led to ice formation was identified, the laser voltage was increased by increments of 5 V, which increased the warming rate slightly. This procedure of increasing the laser voltage was continued until no ice was detected during warming. The warming rate observed when any further increase in laser voltage led to no detectable ice was identified as the CWR. The warming rates were attained through analysis of the high-speed video, from which the times at which the laser fired, ice formed, ice completely melted, and the sample boiled were detemined. By assuming that the temperatures of the droplet when the ice melted and liquid boiled are the melting and boiling temperatures of the CPA solution, respectivly, and that the initial temperature of the droplet is -196 degrees °C (LN$_2$ temperature), the high-speed camera data can be used to arrive at two different values for the average warming rate in the droplet. The laser was fired just prior to the residual liquid nitrogen evaporating, so we are confident that the initial temperature of the droplet is -196 degrees °C. The internal droplet temperature after leaving the LN_2 bath was measured and showed the droplet temperature remains at LN_2 temperature until the boiling of adjacent LN_2 has ceased. Since the laser was fired once the residual LN_2 evaporated, we are confident in the assumption that the droplet is at LN_2 temperature the moment the laser fires. The final warming rate was determined by averaging the warming rates estimated based on the temperature indicators of ice melting and liquid boiling, assuming ice was detected. In the cases where no ice was detected, the boiling temperature indicator was used alone. These scenarios allowed for more accurate upper bound error estimation. Figure 4.15 shows high-speed videos of under-warmed and critically warmed droplets.

4.4 Results and discussion

4.4.1 Validity of visual assay to determine CCR and CWR

Visual detection of melting and boiling is key for this analysis to be valid. By warming below the CWR we are able to see ice form and then subsequently melt as the droplet temperature increases. The time at which all ice has melted (disappeared) is noted and corresponds to the droplet being at the melting temperature. Thus, by using the frame data we can then calculate the warming rate since we know the time at two temperature points (LN2 and melting). We slowly increasing warming rate until no ice was formed on warming. This was the critical warming rate calculated from ice melting. For boiling, we used pulses that were longer than necessary to bring the droplet up to room temperature, thus causing the droplet to boil. When boiling bubble formation encompassed the entire droplet, the temperature was assumed to be the boiling temperature. Incidentally, the rates from boiling warming rate and melting warming rate were similar, which makes sense as the temperature increased linearly due to the laser. This gives us confidence that both temperature indicators are satisfactory.

When considering CCR and CWR measurements, it is important to interpret the data with respect to the method with which it was gathered. For example, measurements made with DSC examine heat flow associated with crystallization and may give different results than convective methods that rely on the visual detection of ice, which itself is subjective. Even CCR and CWR data gathered by the same method, DSC for example, may differ simply from the use of different sample sizes or pans of different roughness, which can alter nucleation in the sample. A separate problem arises in convective methods that rely on visual detection, where differences in lighting, image resolution, and experimenter subjectivity all can lead to different measurements of CCR and CWR. Figure 4.3 shows that the CCRs of glycerol and PG exhibit the same trends, or have roughly the same slopes, with changing concentration as those reported in the literature.[69,117,118] DSC in general agreed better with our CCR data than convective cooling in capillary tubes; however, there was considerable variability in CCR data gathered via capillary tubes for glycerol than the data gathered here with freely exposed droplets. Additionally, extrapolations of CCRs of PG and glycerol to zero concentration give a CCR for pure water on the order of 10^7 °C/min, consistent with a meta-analysis of CCR data in the literature. The degree of offset between the measured values and those from the literature differ between PG and glycerol, which is to be expected, as the data from the literature were gathered via DSC for PG and via capillary quenching for glycerol. However, the exponential trend for CCR and concentration should be mostly independent of characterization method, as was observed, with the magnitude of the offset between methods governed by the detection threshold of crystallization for vitrification. In both cases, since the offset appears to be constant with concentration and the exponential factor is roughly the same, the offset between methods can likely be attributed to differences in the thresholds for the visual detection of ice, where the cryotop quenching method for attaining CCRs likely has a lower threshold than DSC and capillary quenching. One explanation for this difference in detection threshold is the small size of the capillary tubes, which makes the visual assessment of crystallization difficult. It is also possible that the cryotop induces more heterogeneous nucleation than the capillary tube and DSC, requiring larger CCRs to compensate for increased nucleation. Note that in both Figure 4.8 and Figure 4.3, no data obtained by convective methods go beyond 10^6 °C/min. The ultimate limit of detection for convective warming has not been explored, but given the thermocouples currently available on the market, 10^6 °C/min is likely approaching this limit (see further discussion in SM).

There were larger uncertainties in the CWR experiments than in the CCR experiments, with generally better fitting data in the latter, see Figure 4.8. This difference can be attributed to several causes. First, the droplets in the CCR experiments were at LN_2 temperature when analyzed, which provided a static view of the degree to which the droplet was crystalized and allowed for the use of high-quality imaging to aid ice detection. In the CWR experiments, the high-speed video frames were less resolved than the images taken in the CCR experiments, making ice detection more difficult. Bubble formation from laser warming also made ice detection difficult in some cases by obscuring the ice underneath. The most prominent source of error was likely the temperature gradients within the warming droplet itself, with parts of the droplet warming faster than others. The source of these gradients and the implications for the CWR measurements are discussed in more detail below. It should be noted, though, that these temperature gradients also exist in convectively warmed and cooled droplets, so the relative magnitude of the gradients is important when considering error in the measurements. Future studies may incorporate more advanced image processing techniques to quantitatively determine the amount of ice in droplets systems, such as those used in the measurement of ice growth rates in thin films of CPAs.[119]

4.4.2 *Concentration dependence of CCR and CWR*

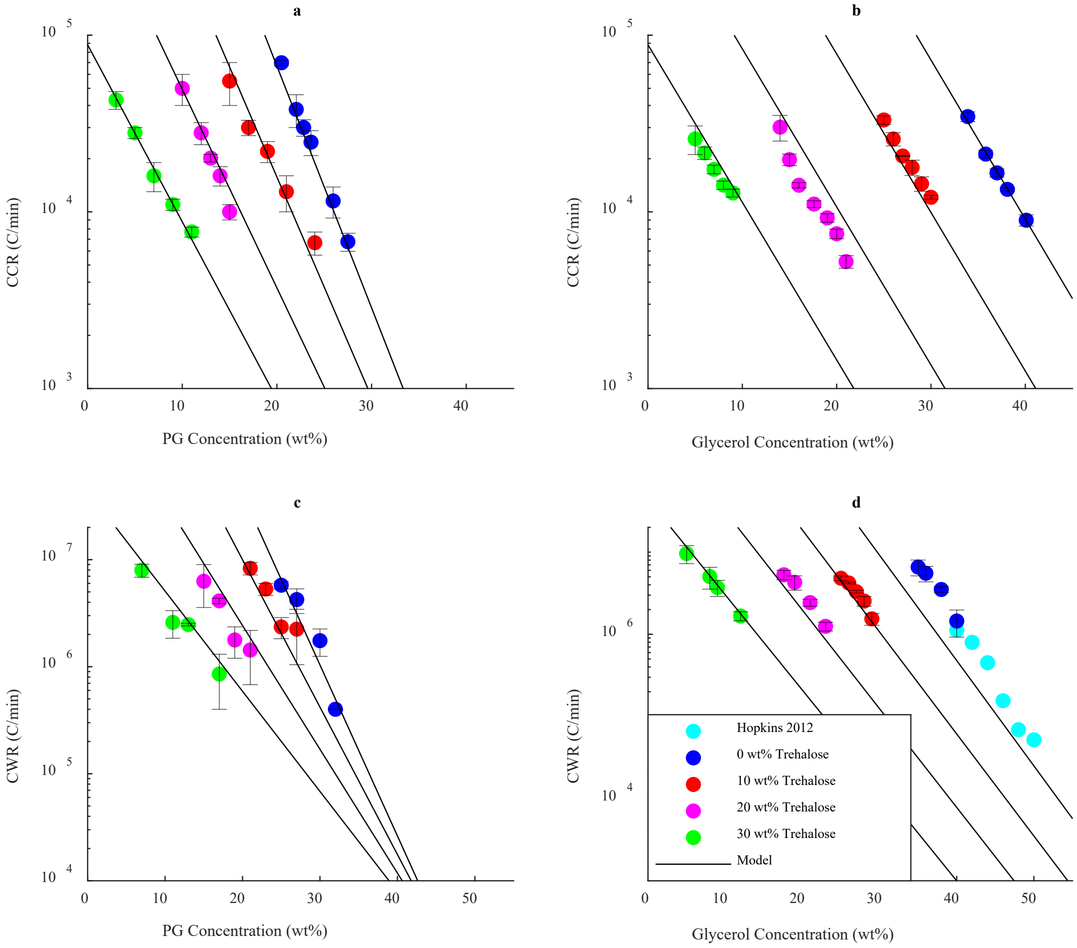

Figure 4.8. Measured CCRs and CWRs of CPA solutions. Plots show CCR of (a) PG-trehalose solutions and (b) glycerol-trehalose solutions; and CWRs of (c) PG-trehalose solutions and (d) glycerol-trehalose solutions. Each plot includes the two-species model equation (4.6) for the CCR/CWR based off the CCR/CWR measurements of single-species solutions of trehalose, PG, and glycerol.

Table 4.2. Exponential and pre-exponential factors for the cooling and warming rate dependence of the CCR and CWR, respectively.

	A Pre-exponential factor CCR (°C/min)	***A*** Pre-exponential factor CWR (°C/min)	**α** Exponential factor CCR (wt%$^{-1}$)	**α** Exponential factor CWR (wt%$^{-1}$)
Trehalose	3.64E7	6.42E10	0.207	0.243
PG	5.22E7	7.26E10	0.325	0.368
Glycerol	4.96E7	2.18E11	0.216	0.295

The CCRs measured for PG-trehalose and glycerol-trehalose solutions both showed a strong exponential dependence on concentration (Figure 4.8). The CCR and CWR data for unary solutions of glycerol, PG, and trehalose in Figure 4.8 and Figure 4.9, along with equation (4.6), allowed for calculations of the CWRs and CCRs of the mixtures of these solutions, which are shown as the model lines in Figure 4.8. This calculation was contingent on the data in Figure 4.13, which indicate the functional form of the concentration dependence of the exponential factor from equation (4.4). Figure 4.13 shows how the exponential factor changes as the concentration of trehalose is altered, indicating that a linear relative concentration averaging of exponential factors is appropriate for a two-species solution, e.g., a constant change in concentration fraction leads to a constant change in the exponential factor. This result allows for a simple calculation of the changes in the CCR or CWR of a solution as the concentrations of its constituents are altered, provided that the exponential and pre-exponential factors for the individual constituents are known. Using this relation, one can identify better CPA mixtures by analyzing the effects of changes in the component concentrations on the CCR and CWR without requiring cumbersome and slow characterization. The exponential and pre-exponential factors for glycerol, PG, and trehalose are given in Table 4.2. We see some deviation from this model, but the general trends seem to be captured quite well. In Figure 4.8c, we see that the model-predicted lines converge towards a singular point near 50 wt% concentration of PG. Of course, in reality, this convergence does not occur and is simply the consequence of uncertainty being compounded with further extrapolation. In other words, the multi-species mixing model for CWR and CCR works best in the regime that the data were measured in barring some low-error measurement method that can measure across large sections of the concentration regime. Another option is to drastically lower the uncertainty in the concentration regime that the measurements were made in, thereby allowing for more confident extrapolations both forward and backward. The CCRs and CWRs for trehalose were measured for higher concentrations of 35-40 wt% while at lower concentrations they were then estimated by taking the exponential fit data for trehalose-glycerol and trehalose-PG mixtures in Figure 4.8 and extending them to zero concentration for PG and glycerol. This data was used in combination with the measured values for trehalose to derive the exponential fit parameters for trehalose, which are shown in Table 4.2 along with those for PG and glycerol. The low-concentration extensions for both the CCRs and CWRs of trehalose line up with the measured data, implying that the estimation of the CCRs and CWRs for lower concentrations of trehalose is accurate, assuming that the exponential dependence on concentration behaves similarly at low concentrations as it does at moderate concentrations. Additionally, it was shown that trehalose has a larger effect on the CCR and CWR of glycerol than on those of PG, though the exact mechanism causing this is unclear. One proposed mechanism is that added sugars affect the CPA glass transition temperature, thereby altering the vitrification properties.[120] It is also possible that the large difference in viscosity between PG and glycerol plays a role. We offer an additional explanation based on equation (4.6). If we compare two solutions of equal weight percent trehalose and glycerol/PG, we see that the only differing parameter is α_j. Since we have already determined that PG-water solutions have a higher α_j that glycerol-water solutions, it follows directly that the addition of trehalose, or for that matter, any other CPA, will affect the

CCR and CWR of the glycerol solutions more than those of the PG solutions with respect to concentration.

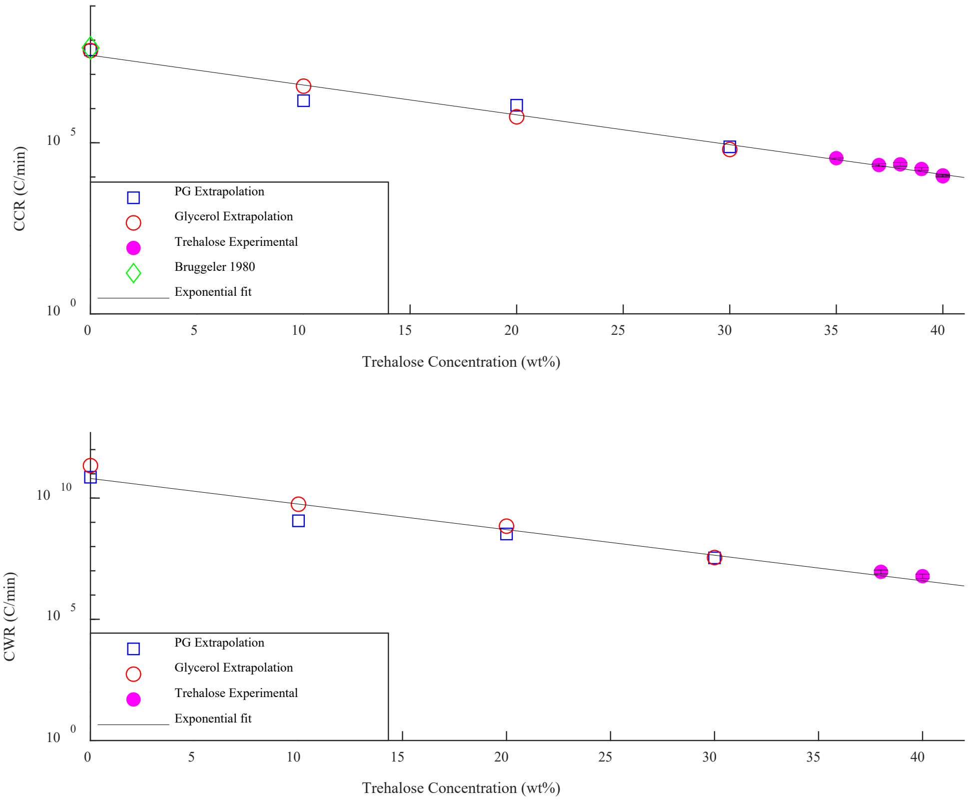

Figure 4.9. (a) CCRs of trehalose gathered by direct measurement and extrapolation of the CCRs from glycerol-trehalose and PG-trehalose solutions. Also shown is the predicted CCR of pure water. (b) CWRs of trehalose gathered via laser calorimetry of trehalose solutions and extrapolations from the laser calorimetry of glycerol-trehalose and PG-trehalose solutions.

Table 4.3. Estimated values of the CCR and CWR of pure water from the experimental values attained from LN_2 quenching and laser calorimetry of PG, glycerol, and trehalose solutions.

Rates	Experimental
CCR	3.64 –5.22E7 (°C/min)
CWR	0.64– 2.18E11 (°C/min)

The CCRs and CWRs of CPAs are known to depend exponentially on concentration in several different concentration regimes. Unfortunately, due to the constraints on the methods for measuring the CCR and CWR, one method cannot be used over the entire concentration regime, as shown in Figure 4.10. That is to say, it is not that data collected by different methods cannot be directly compared but that some discrepancies are to be expected when comparing CCRs and CWRs from different methods. Thus, we cannot be certain that the exponential relationship applies across the entire concentration regime or if the limitations of the methods themselves mask the true relation. As a result of the method constraints, measurements are made by DSC in the low-rate regime (<100 °C/min), by convective cooling/warming via quenching in the moderate-rate regime (10^3-10^6 °C/min), and by laser calorimetry for CWR measurements only in the high-rate regime (>10^6 °C/min). As of this date, there exists no method capable of volumetric cooling in this high-rate regime. Each method has unique limitations. DSC is limited by the ability to stably extract or add heat to a sample and by the sensor sensitivity. Convective methods rely on thermocouples, which inherently have a maximum detectable rate. The thermocouple also adds thermal mass and possible nucleation sites to a system, thereby altering the CCR or CWR measurement. The key downside of convective methods is that outside of the lumped regime (i.e., larger droplets) temperature gradients can be appreciable so that measured temperatures at one point are not representative of the whole system. Additionally, because the way to attain larger warming rates is to decrease the sample volume, different warming rates necessarily have different cooling rates prior to warming in convectively warmed systems.

The general question now arises as to how the CWR should be measured, for instance, whether all samples should be cooled at the same rate prior to warming or whether samples should be cooled as fast as possible prior to warming. At higher CPA concentrations, which correspond to lower warming rates, this requirement does not pose much of a problem, as cooling rates much larger than the CCR are easily attainable, but this is not true as the

CPA concentration is decreased. Laser calorimetry is still limited by size on cooling, but relatively uniform warming at arbitrary rates is achievable, allowing for a much more robust characterization of the CWR along with the ability to attain much larger warming rates. As the CPA concentration decreases and the CCR increases, temperature uniformity on warming becomes much more important, as conduction no longer smooths out the temperature gradients on the shorter timescales during warming. Future experiments involving less powerful lasers may make it possible to determine CWRs from 100 °C/min up to 10^8 °C/min, all being warmed uniformly with the cooling rate under precise control, thereby eliminating much of the error between characterization methods. It should also be noted that coupling high-power laser calorimetry with faster droplet cooling approaches will make possible the characterization of CWRs of CPAs in the 1-2 M regime (~10-20 wt%), with rates exceeding 10^8 °C/min.

In the literature, extrapolations of CWR data from moderate-concentration CPAs out to zero concentration yield extreme differences in the CWR of pure water, though the measured data follow exponential fits quite well in the regimes they were measured in. The estimated values of the CCR and CWR for water that are derived from the PG, glycerol, and trehalose data are shown in Table 4.3. The same treatment of the literature data for the CCR from moderate-concentration CPAs also yielded differences in the CCR of water but to a much lesser extent. These differences in the extrapolated CWRs and CCRs of water could be caused by errors in the measurement methods themselves or by the possibility that the CCR and CWR do not follow an exponential dependence on concentration throughout the entire concentration regime. The discrepancies between the extrapolated values from different CPAs are much more apparent in the CWR measurements than in the CCR measurements, possibly implying the presence of systemic errors in the measurement methods themselves. There is also evidence that the exponential relationship between CWR/CCR and concentration does not apply to the entire concentration regime, as it is known to break down at high concentrations; however, it is unclear whether this breakdown is due to the different characterization methods applied in the different regimes shown in Figure 4.10 or differences in sample volume or whether it is a fundamental property of CPAs.

Using the rotational correlation time for water, the time it takes for a water molecule to rotate one radian via diffusion, we can estimate an upper bound on the CWR for pure water. This correlation time has been measured at 1.7 ps,[121] which means that if water is warmed from its glass transition temperature to the melting temperature faster than 1.6×10^{15} °C/min, the water molecules will not have enough time to rotate and align in the new crystal formation, assuming a maximum necessary rotation of 180 degrees. This of course is an overestimate, as the rotational correlation time for supercooled and vitrified water is certainly larger than that of room-temperature liquid water. Therefore, we can infer that extensions of CWRs beyond 10^{15} °C/min are erroneous and that either the exponential model breaks down or there is error in the measurement.

The ratio of CWR to CCR was also shown to be exponentially dependent on concentration based on the multi-species model developed and data gathered throughout the experiments (*see* Figure 4.9 and Figure 4.14). This dependence is to be expected, as both the CCR and CWR are exponentially dependent on concentration. It was found that the lower the concentration is, the larger the difference between the CWR and CCR, with estimates of the difference for pure water being a factor of roughly 3000-3500. This result has unfortunate implications for cryopreservation. As the concentrations of CPAs are lowered to avoid CPA toxicity, not only does the CCR rise, but the CWR rises at an even faster rate, meaning that extremely fast warming rates on the order of 10^9 °C/min are required to rewarm CPA concentrations under 15 wt%, at least for the CPAs studied. Unless CPAs that have a much lower CWR/CCR ratio exist, it seems unlikely that the current methods will successfully rewarm samples with CPA concentrations much under 15 wt% without appreciable ice formation.

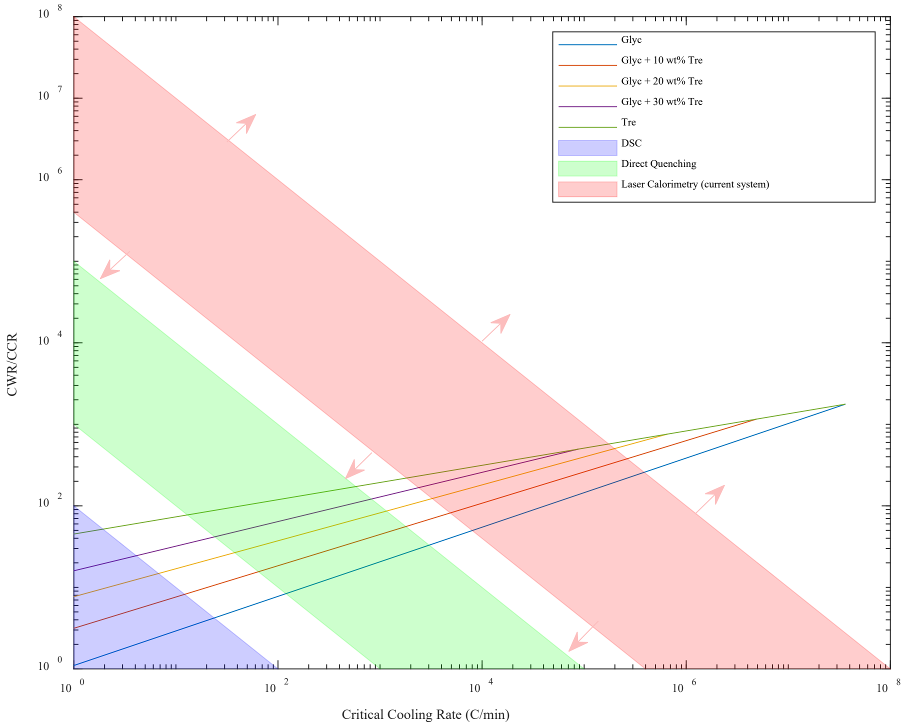

Figure 4.10. Effect of trehalose on the relationship between CWR/CCR and CCR of glycol-trehalose solutions. The CWRs and CCRs were determined from the two-species model based on the quenching and calorimetry experiments. The shaded regions show the different CWR measurement regimes corresponding to conventional DSC, direct quenching, and laser calorimetry with our current system. Different laser powers and high-speed cameras allow the boundaries of the laser calorimetry region to be extended.

Figure 4.9 illustrates this difference with a plot of CWR/CCR vs CCR. One can see that in a two-species solution of glycerol and trehalose, the CWR/CCR curves of the individual species form upper and lower bounds to the CWR/CCR curves of mixtures of the two species. This feature arises because the exponential factors of a unary trehalose solution and a unary glycerol solution are almost identical, and so the exponential factor of glycerol-trehalose mixtures has almost no concentration dependence. In contrast, for PG-trehalose, shown in Figure 4.14, these lines cross, which can be attributed to the concentration dependence of the exponential factor between PG and trehalose. Since the minimum warming rate of the laser was 400,000 °C/min, a line taken from 400,000 °C/min on the y-axis to 400,000 °C/min on the x-axis in Figure 4.9 arrives at the lower bound of the red-shaded laser calorimetry region. This red-shaded region could be broadened with the implementation of lasers of higher or lower power as well as faster high-speed cameras. The volume of the sample is also a limiting factor in laser calorimetry. In principle, much smaller droplets than were used in the study could be constructed and measured via laser calorimetry; however, this measurement would require an additional focusing lens for the high-speed camera. Additionally, it should be noted that this upper limit on the warming rate measurement was not reached in this study and that vitrification on cooling was actually the limiting factor.

4.4.3 *Mixture Model*

We come across the relation for a mixture of two CPAs by this simple method. We know that at $c_1 = 0$ the $R_{1,2} = R_2$ since it is no longer a mixture but a unary solution, likewise for $c_2 = 0$. Then the following function maintains both these constraints.

$$R_{1,2} = Ae^{-\alpha_1 c_1}e^{-\alpha_2 c_2}e^{-f(\alpha_1,\alpha_2,c_1,c_2)c_1 c_2} \tag{4.7}$$

We notice in Figure 4.11 that this formula for mixing comes naturally from the graphical representation of how the mixture of two CPAs should affect CCR or CWR, so that $R_{1,2}$ contains both R_1 and R_2, and that the mixing terms is some function of the individual components, all while maintaining exponential dependence on concentration.

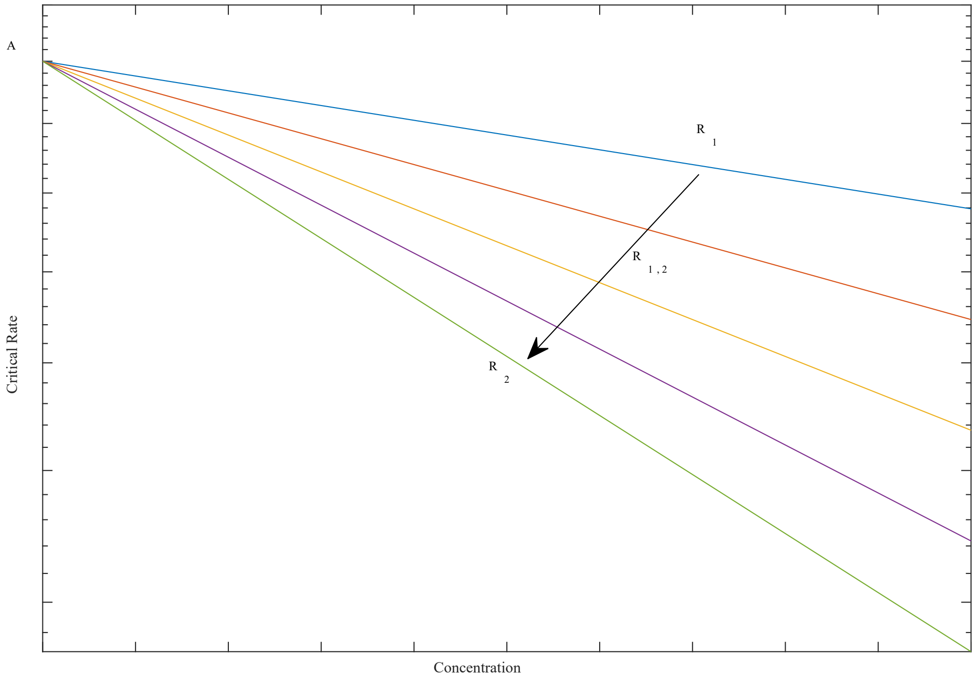

Figure 4.11. Shows how the CCR or CWR is changed when two CPAs are mixed together (assuming equal pre-exponential factors), where concentration simply refers to the total concentration of all components of the CPA.

In theory, the preexponential factor should be the same for all cryoprotectants, but in actuality, there will be differences due to error and uncertainty, and breakdowns in the exponential trend. To combat this variation, the pre-exponential factor can be considered to be the average of those for each individual species i in the mixture.

$$A_{avg} = \frac{1}{N}\sum_{i=1}^{N} A_i \tag{4.8}$$

So, equation (4.6) for $t$hen becomes

$$R_n(c_1, \ldots, c_n) = A_{avg}\prod_{i=1}^{n} e^{(-\alpha_i c_i)} \prod_{1\le i<j\le n} e^{-\frac{\alpha_j-\alpha_i}{\chi_i}c_i c_j} \tag{4.9}$$

For CPA mixtures with constituents that have pre-exponential factors that vary considerably, a similar treatment must be applied to the pre exponential factor as was done in equation (4.4). For a mixture of two species if the linear concentration average that applied for the exponential factor also applies to the pre-exponential factor, we arrive at equation (4.10).

$$A_{mix} = A_1 + \frac{A_2 - A_1}{\chi_2} c_2 \tag{4.10}$$

At this moment it is not known if equation (4.10) is valid. Verification is left to a future study, though we hypothesize this behavior which is seen in Figure 4.12.

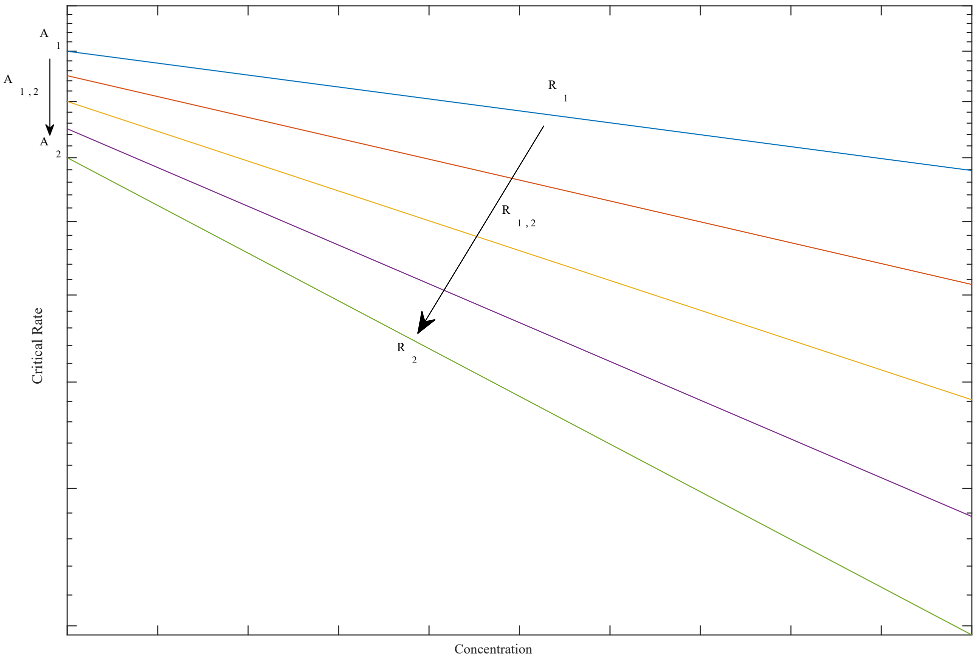

Figure 4.12. Shows how the CCR or CWR is changed when two CPAs are mixed (assuming mixing of pre-exponential factors), where concentration simply refers to the total concentration of all components of the CPA.

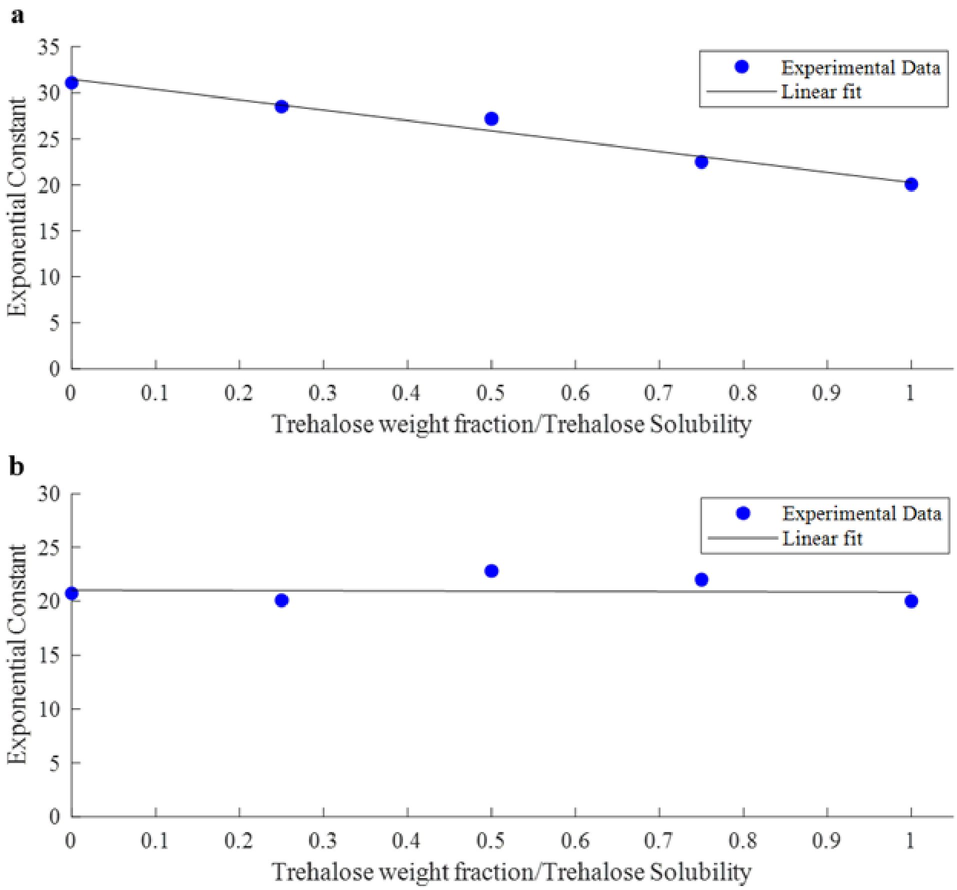

Figure 4.13. Concentration dependence of the exponential factor for a PG-trehalose mixture (a) and a glycerol-trehalose mixture (b).

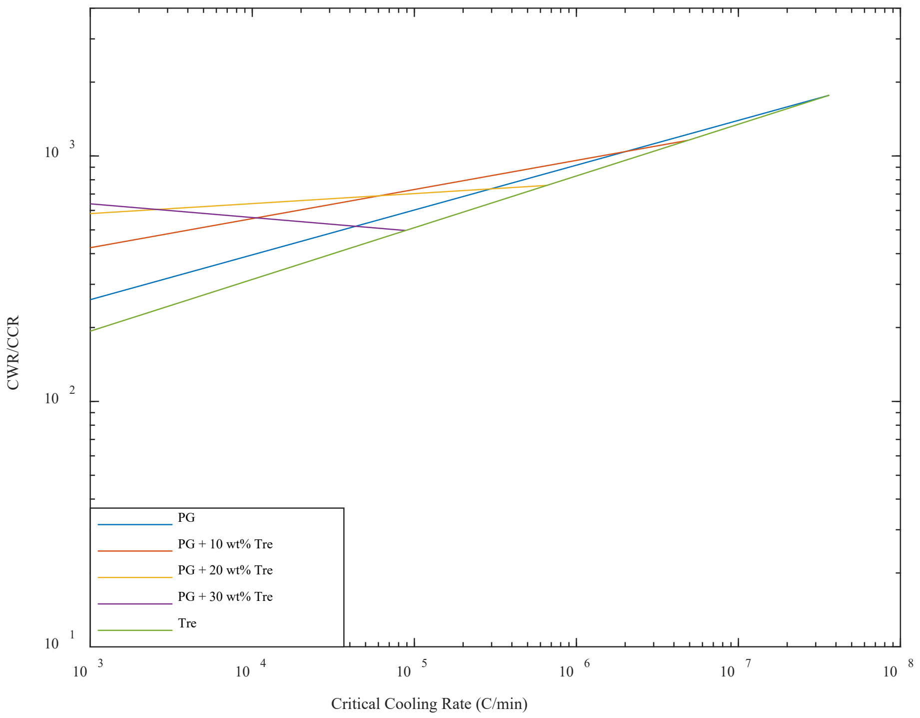

Figure 4.14. Effect of trehalose on the relationship between CWR/CCR and CCR of PG-trehalose solutions. The CWRs and CCRs were determined from the two-species model based on the quenching and calorimetry experiments.

4.5 Warming Rate Estimation

4.5.1 *Warming rate estimation via highspeed camera*

The high-speed camera had the ability to pick up near-infrared radiation, which was advantageous for synchronizing the camera with the laser pulse, allowing for accurate estimation of the start of the laser pulse. By using this time point with temperature indicators at the melting point and boiling point of the CPA, we could predict the warming rate in the droplet during laser warming. This treatment is contingent on an absence of substantial superheating of the liquid and solid phases in the droplet. If this superheating were to occur, we would expect major differences in the warming rates calculated from melting and boiling. Fortunately, there was not a significant difference between these two metrics, at least with respect to the error in the system. That is, the inter-droplet variability outweighed any differences between warming rates calculated with these two metrics.

VIDEO LINKS IN CAPTION

Figure 4.15. Videos of laser warming for a droplet warmed below the critical warming rate (a) https://www.youtube.com/watch?v=TY5WjSFbjsw and above the critical warming rate (b) https://www.youtube.com/watch?v=q4aM0Ekpiq8

The two most substantial sources of error in the laser calorimetry experiments are thought to be the droplet shape and random scattering due to bubble and crystal formation, both of which affect the absorption profile in the droplet and induce thermal gradients. In some cases, a ring of ice formed around the base of the droplet at the beginning of a set of experiments. This ice formation was due to the curvature of the droplet being too large and causing lensing of the laser, as seen in Figure 4.18. Over the course of a set of experiments, residue from the droplets would build up on the cryotop and increase the effective hydrophilicity of the cryotop surface, leading to flatter droplets and a reduction in the number of droplets with this ring feature. Warming rates taken from droplets with an apparent ice ring at the base were simply ignored. The droplet shape also changed during warming, which altered the absorption profile in the droplet by changing how the droplet bent the incoming laser over the duration of the pulse. Due to the random nature of this phenomenon, it is difficult to quantify its overall effect on the warming rate measurement variability. Bubble and crystal formation in the droplet during warming also induce laser scattering, but the extent to which it affects the measurement variability and thermal gradients is also unknown and would make an interesting topic for future study.

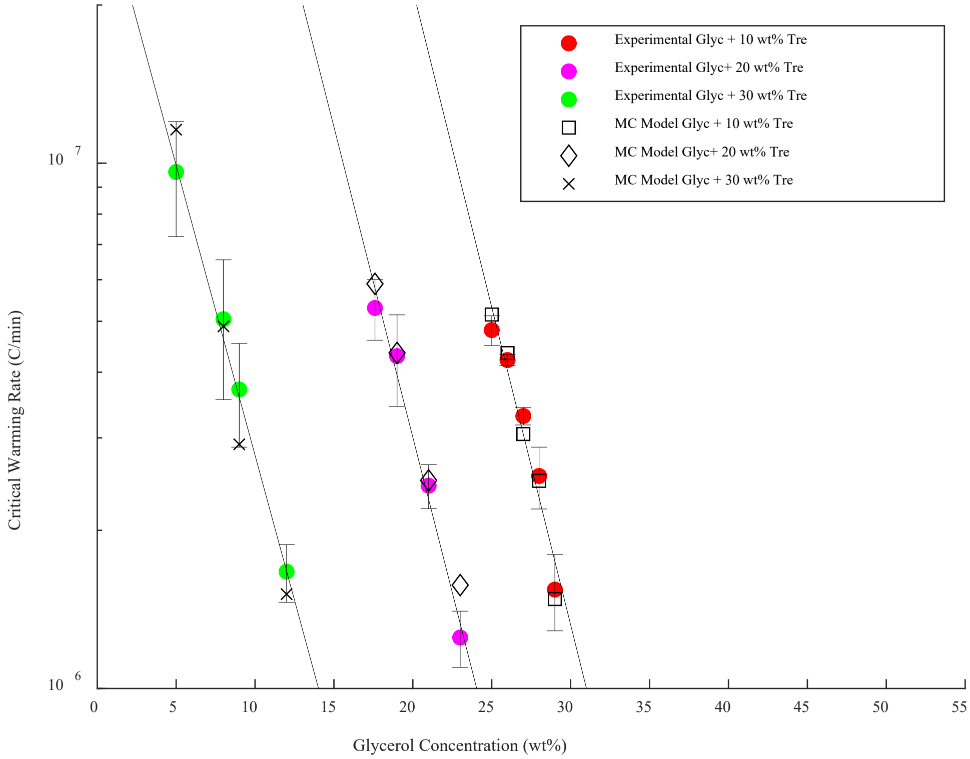

Figure 4.16. Comparison of the CWRs measured via laser calorimetry and the warming rates calculated from the MC model based on the laser settings and gold concentrations in the CWR experiments.

The MC model also provided an independent metric for the warming rate calculations in the laser calorimetry experiments. Figure 4.16 shows the measured warming rates and the predicted warming rates calculated based on the absorption properties of the GNR solution, shown in Figure 4.17, and the laser energy settings used on samples warmed at the CWR. Most of the model-predicted rates are within the error bars of the CWR data gathered via laser calorimetry. This agreement in the data leads us to believe that the warming rates measured in the laser calorimetry experiments are reasonable approximations of the true values, since two independent methods gave similar results. The MC model was also able to accurately predict the ice ring that forms along the outer edge of the droplet in cases of high droplet curvature. The success of the MC model in accurately predicting the warming rates and temperature gradients in the droplets suggests that it is a powerful tool for studying warming in warming regimes not yet attainable with current technology (>10^8 °C/min) as well as at scales that are invisible to the current high-speed camera, such as on the cellular level.

4.5.2 *Modeling warming rates via Monte Carlo light transport simulation*

The validity of the CWR measurements made via laser calorimetry is contingent on the uniformity of the temperature profile during warming. If large gradients exist throughout the droplet, the calculated warming rate may not be accurate. Temperature uniformity during the plasmonic heating of GNPs has been studied via MC modeling previously in Liu et al. 2020. [116,122] That MC model of laser warming was adapted to the laser calorimetry setup used in this study, which incorporated the scattering, absorption, reflection, and refraction interactions of laser photons with droplets. First, a photon path Γ through the system consisting of linear segments of length s_i was constructed, where s_i is a function of the absorption coefficient μ_a, scattering coefficient μ_s, and a uniform random variable $U_{[0,1]}$ between 0 and 1.

$$s_i = -\frac{ln(U_{[0,1]})}{(\mu_a + \mu_s)} \tag{4.11}$$

Each of these segments can be thought of as a photon path prior to a scattering event. The polar angle θ and azimuth angle φ between subsequent segments s_i and s_{i+1} are governed by equations (4.12) and (4.13), respectively, where g is the scattering anisotropy coefficient.

$$cos(\theta) = \frac{\left(1 + g^2 - \left(\frac{1 - g^2}{1 - g + 2gU_{[0,1]}}\right)^2\right)}{2g} \tag{4.12}$$

$$\varphi = 2\pi U_{[0,1]} \tag{4.13}$$

Photons that cross the droplet boundary are reflected via Snell's law with respect to the normal direction at the point of intersection. Upon reflection, photon energy is diminished according to the Fresnel equations. By applying the expected value to Beer's law along Γ , we note that the photon energy before and after photon scattering is given by equation (4.14), while the energy absorbed is given by equation (4.15).

$$E_{i+1} = \frac{\mu_s}{\mu_a + \mu_s} E_i \tag{4.14}$$

$$E_{absorbed} = \frac{\mu_a}{\mu_a + \mu_s} \tag{4.15}$$

After a sufficient number of scatterings, absorptions, and reflections to cause the photon energy to fall below some small threshold, the photon trajectory will be terminated. After simulating millions of photons in the environment, we can generate an accurate approximation of the heat source function or specific absorption rate (SAR). Once the SAR is calculated, it can then be used as input into a COMSOL model of heat transfer within the droplet to determine the spatial-temporal temperature profile via finite element analysis.

$$\rho c_p \frac{\partial T}{\partial t} - \nabla \cdot (k \nabla T) = SAR \tag{4.16}$$

$$T(\boldsymbol{x}, 0) = T_{LN_2}, \quad x \in \Omega \tag{4.17}$$

$$-k\Delta T(\boldsymbol{x}, 0) = h\big(T_a - T(\boldsymbol{x}, 0)\big), \quad x \in \partial\Omega \tag{4.18}$$

Where Ω consisted of a hemisphere with diameter 1.24 mm, corresponding to a .5 µL droplet, T_{LN2} was liquid nitrogen temperature 77K, T_a was ambient temperature 273K, and the heat transfer coefficient was taken to be 100 $Wm^{-2}K^{-1}$.[123] To verify that there is not extreme local heating around each nanoparticle, causing a breakdown of the global heating assumptions, we reference the solution to the transient heat equation around a nanoparticle.[124]

$$T(r,t) - T_\infty = \frac{dQ_{nano}}{4\pi r k \Delta t}\left[erfc\left(\frac{r - r_p}{2\sqrt{\alpha t}}\right) - \exp\left(\frac{r - r_p}{r_p} + \frac{\alpha t}{r_p^2}\right) \operatorname{erfc}\left(\frac{r - r_p}{2\sqrt{\alpha t}} + \frac{\sqrt{\alpha t}}{r_p}\right)\right] \tag{4.19}$$

Where dQ_{nano} is the power generated by a single nanoparticle, r_p is the nanoparticle diameter, Δt is the pulse duration of the laser, k is the thermal conductivity, and α is the thermal diffusivity. We note that at the nanoparticle surface, the steady state temperature difference between the nanoparticle and its surroundings is:

$$\Delta T_{nano} = T(r,t) - T_{\infty} = \frac{dQ_{nano}}{4\pi r k \Delta t} \tag{4.20}$$

For the pulse energy of 60 joules, pulse duration of 1 ms, nanoparticle density 5×10^{16} np/m^3, and droplet volume of .5 µL, we estimate the ΔT_{nano} = .006 K. Thus, we can be confident that localized heating around the nanoparticles is inconsequential, and that the global heating approximation is valid. Additionally, an alternate rational for validating bulk heating in laser warmed nanoparticles is given by analyzing thermal confinement.[125]

For each critical warming measurement, the MC model was used to predict the warming rate of the droplet by using the optical properties of the GNR concentration used in that droplet as well as the laser settings at the determined CWR. The thermal properties of PBS+2M glycerol were used in the finite element modeling for all CPA concentrations modeled, as this mixture provided the closest temperature-dependent data to the CPAs used in this study.[126] To adequately describe laser warming, the optical properties of the GNPs need to be measured. A linear relation between the absorption coefficient and concentration of the GNR solution was determined via UV-VIS spectroscopy, as shown in Figure 4.17. The scattering coefficient and scattering anisotropy coefficient were estimated via the relation found in Liu et al. 2020. The droplet in the COMSOL modeling had a contact angle of 90 degrees, making it a perfect hemisphere. In reality, the droplet spread out more, eliminating the large degree of lensing that occurred at the edges. Regardless, the warming rates from the COMSOL model of the perfect hemisphere were essentially identical to those with a slightly flatter shape. Due to this lack of difference, the hemispherical droplet shape was used in the modeling for ease of defining the boundary.

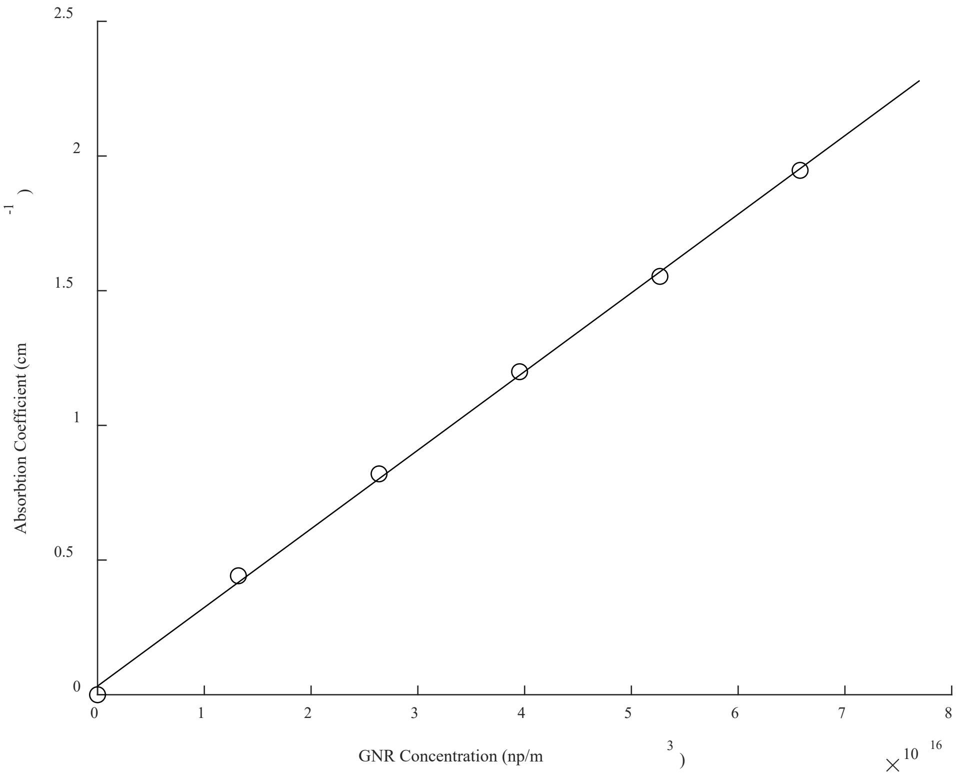

Figure 4.17. Absorption coefficient vs concentration of GNR solution measured via UV-VIS spectroscopy.

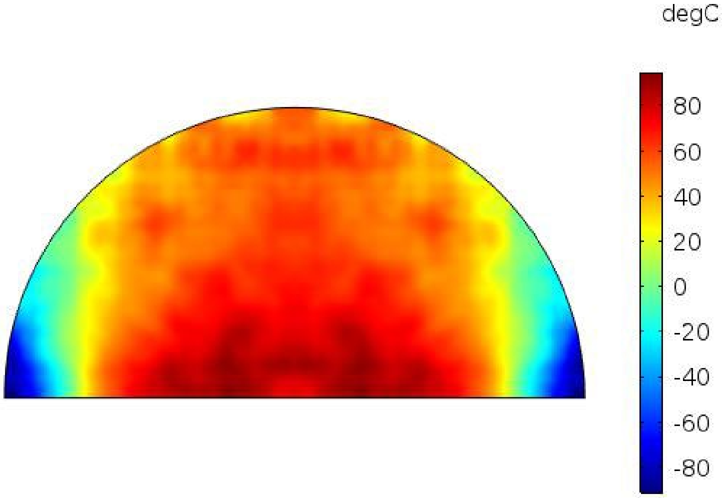

Figure 4.18. Temperature profile in a droplet of GNR solution right at the end of the laser pulse.

4.6 Conclusion

The CWRs ranging from 0.4×10^5-10^7 of glycerol-trehalose and PG-trehalose solutions were measured via laser calorimetry, the fastest such rates measured to date. The CCRs of these same CPAs were also measured via direct quenching into LN_2. The data for CCR and CWR both were consistent with extrapolations from literature data measured at higher concentrations. Additionally, by measuring the CWR and CCR dependence of PG and glycerol for varying concentrations of trehalose, a model describing CCRs and CWRs for CPA mixtures was developed and verified, allowing for calculations of the CCR and CWR of CPA mixtures given only their constituent solutions' individual CCRs or CWRs through the use of equation (4.6). This model allows for the analysis of CPA cocktails without the need to make and characterize them, making CCR and CWR optimization much more efficient. The data as well as model parameters for fitting the data for PG, glycerol, and trehalose were provided. We now provide a framework, through laser calorimetry, for measuring the CWRs of CPAs in not only the low-concentration regime but throughout the concentration regime by simply altering the laser power, eliminating much of the uncertainty that arises when comparing CWRs measured by different techniques at different size and rate scales. Together, this work reported new experimental and theoretical results linking the CWR and CCR for a given CPA within an otherwise inaccessible low-concentration measurement regime (20-40 wt%).

ADAPTED FROM

Kangas, J. *et al.* Ultra-Rapid Laser Calorimetry for the Assessment of Crystallization in Low-Concentration Cryoprotectants. *J. Heat Transfer* **144**, 1–9 (2022).

ACKNOWLEDGEMENTS

This work was supported by the National Science Foundation, Grant No. 1941543, NSF Engineering Research Center for Advanced Technologies for Preservation of Biological Systems (ATP-Bio), NIH/NHLBI R01HL135046-01, NIH/NHLBI R44MH122118, NIH/NIDDK R01DK117425-01, and Minnesota Sea Grant.

Chapter 5

Monte Carlo Modeling of Light Transport in Cryopreserved Systems

5.1 Introduction

Understanding light transport in media that absorb and scatter is of vast importance in a diversity of fields in science and engineering. Many imaging techniques, such as optoacoustic imaging, rely on photon absorption and scattering, as well as the theory that underlies it, to adequately generate 3D images of biological systems.[127] Modeling photon migration in systems has been used to analyze time-resolved Raman spectroscopy to predict the extent of scattering in light-opaque systems.[128] Proper understanding of absorption and scattering in a system can also be used to engineer warming rate profiles resulting from photon scatting and absorption. For example, cancer photothermal therapies using gold nanorods as a means to control spatial absorption profiles have been shown to be an effective method for destroying cancer cells when warmed locally by high intensity light.[129] Perhaps most bizarre of all is the applicability of light transport modeling in cryopreservation, where wavelength-tuned nanoparticles are used in conjunction with a high-powered pulse laser to rapidly rewarm cryopreserved specimens from cryogenic temperatures, outpacing ice formation on warming.[130]

Though light propagates as both a wave and a particle, from a modeling standpoint it is much easier to treat as a discrete particle. Boltzmann provides an exact description for a particle formulism of light transport. Unfortunately, the Boltzmann transport equation is an integrodifferential equation which yields no analytic solutions outside of trivial cases. This is further complicated when coupling the transport equation to other phenomena which may be at play in the system, such as boundary conditions involving reflectance and refraction between media of different constitutions. Several attempts have been made to explain light transport in systems outside of Boltzmann's formulism. One such attempt derives itself from a simplified solution to Boltzmann's equation. The Bhatnagar–Gross–Krook equation contains a solution when simplified to be in the semi-infinite domain, in the absence of scattering, and a constant refractive index. This solution is commonly known as the Beer-Lambert law, discussed later in this chapter.[131] A second approximation comes from considering the case where scattering dominates absorption, derived from functional expansion methods: the standard diffusion approximation (SDA). The SDA reduces the complexities of light transport in scattering media to a diffusion problem, and thus a relatively simple partial differential equation, that under further simplifications, can be linked to an exponential decay solution akin to the Beer-Lambert law. Unfortunately, these methods fail when considering the full problem of light transport, absorption, scattering, reflection, and refraction, in arbitrary domains. Even finite element approaches are unstable and thus unsuitable for solving these types of problems due to inconsistencies in discretizing the computational domain. Monte Carlo methods ultimately have shown to be the most accurate and effective method for simulating light propagation in tissue.

Monte Carlo simulations use probabilistic sampling and statistical modeling to calculate either the mathematical functions that solve systems of equations or mimic the nature of the laws governing the system to generate the solutions based off probabilistic interpretations of the governing equations. These types of simulations arise necessarily in areas of science and engineering involving systems of coupled linear and nonlinear partial differential equations, quantum mechanics, and even mathematical finance. The earliest known utilization of the Monte Carlo method was in the 18th century, when Georges Louis LeClerc, Comte de Buffon tossed a large number of needles onto a number of lines on the ground to estimate the value of π as a rational number. He showed that, given that the needles were tossed randomly, had a probability of landing on a line that was $2/\pi$. He even reportedly tested this by tossing baguettes over his shoulder onto a tile floor.[132] In these studies, we use Monte Carlo simulations to analyze the way that light propagates in cryopreserved systems, interacting with the system to generate heat and bring the preserved specimen out of the cryopreserved state. We study the effects of changing various optical properties such as absorption, scattering, scattering anisotropy, refractive index, and the domain geometry to better understand spatial control of light absorption profiles.

Successful vitrification, and thus cryopreservation, of biological systems – i.e., putting them in an amorphous glassy state at -140 ºC for indefinite storage – demands rapid cooling rates, ultra-rapid warming rates, and chemicals known as cryoprotective agents (CPAs). Each CPA has its own critical cooling rate (CCR) and critical warming rate (CWR), which are the rates necessary to avoid damaging phase change of water (i.e., formation of ice). Understanding these rates, especially the CWR, cannot be understated, as nonuniform warming it can lead to cracking due to buildup of thermal stresses, and suboptimal warming may simply fail to rewarm a sample at rates necessary to avoid devitrification.[133] Convective warming is most commonly used to rewarm samples with somewhat high levels of CPA (>6M), since this approach is not sufficiently rapid or uniform to rewarm larger organ and tissues at rates necessary to avoid devitrification or cracking.

Recently two novel warming approaches have individually demonstrated their capabilities to rapidly and uniformly rewarm both larger milliliter sized tissues and smaller microliter scale systems of cells and embryos. For larger sized tissues, high concentration CPAs (8-10M) are used along with RF assisted magnetic nanoparticle heating to achieve uniform warming rates on the order 100 °C/min.[42] For smaller systems such as embryos low concentration CPA (2-3M) and gold nanoparticle assisted laser heating is used to generate the necessary rapid rates on the order of 10^7 °C/min.[134] The primary innovation of laser based approach is the use of gold nanoparticles as ultra-efficient transfer agents for laser heating.[135] Injected gold nanoparticles within systems like embryos or droplets allow warming at rate of millions of degrees/min, thus outrunning damaging ice formation and other thermal effects during warming. The gold nanoparticles have a size and a shape that is engineered to strongly interact with specific wavelengths of incident light. Due to the particle's plasmon resonance (a collective oscillation of free electrons that strongly couples to the incident radiation) the absorption cross section of the particles is extremely large.[136] To better engineer a system to rewarmed cryopreserved specimens we must first build a model to derive the laser induced warming profiles. This laser warming profile, or specific absorption rate (SAR) profile, generated via the Monte Carlo simulation is the output used to analyze not only warming profile uniformity, but the warming rate itself, and thus is the key element of this study.

5.2 Monte Carlo Overview

In systems involving light propagation in scattering and absorbing media there are several phenomena to consider. First, absorption, whereby a photon is absorbed by the media and converted into heat in the form of kinetic vibrations. Scattering is a process by which the photon interacts with the media and is not absorbed, but has its trajectory changed instead through interactions with the electron clouds around media particles in its vicinity. The degree to which it is scattered, that is, its deflected angle, can be characterized by the scattering anisotropy g. Other relevant parameters and nomenclature can be seen below in Table 5.1.

Table 5.1. A table of some of the most used parameters involving Monte Carlo photon transport simulations used throughout this chapter.

PARAMETER NAMES	**DESCRIPTION**	**UNITS**
n	Index of refraction	1
I_o	Laser energy density	$\frac{W}{m^2}$
E_p	Laser photon energy	J
E_s	Simulation photon energy	J
f_s	Energy scale factor	1
N_p	Photon volumetric flux	$\frac{\#}{m^3 s}$
μ_a	Absorption coefficient	$\frac{1}{cm}$
μ_s	Scattering coefficient	$\frac{1}{cm}$
μ_t	Attenuation coefficient	$\frac{1}{cm}$
r	Reflectance	1
g	Scattering anisotropy	1
c	Speed of light	$\frac{m}{s}$
h	Planck constant	Js
φ	Fluence rate	$\frac{W}{m^2 s}$
J_p	Laser photon flux	$\frac{\#}{m^2 s}$
s	Photon step size	cm
$X_{[0,1]}$	Uniform random number between 0 and 1	1

An overview of how Monte Carlo light transport can be seen in the flowchart below. First a photon is generated at a random position on the boundary of the domain which is in the cross section of the laser beam. Then the photon's trajectory into the domain is calculated based of the laws of refraction. From that point its energy is updated to accommodate for reflective loss at the boundary. Next the photon steps through the domain in steps determined probabilistically based off the absorption and scattering coefficients of the medium. At the end of this step some of the photon's energy is stored in the domain at the point of absorption. The photon then changes direction according to the scattering anisotropy of the medium. This process continues until the photon energy is below a certain threshold at it is "killed." The laws of reflection and refraction occur at boundaries of the domain if the photon encounters it.

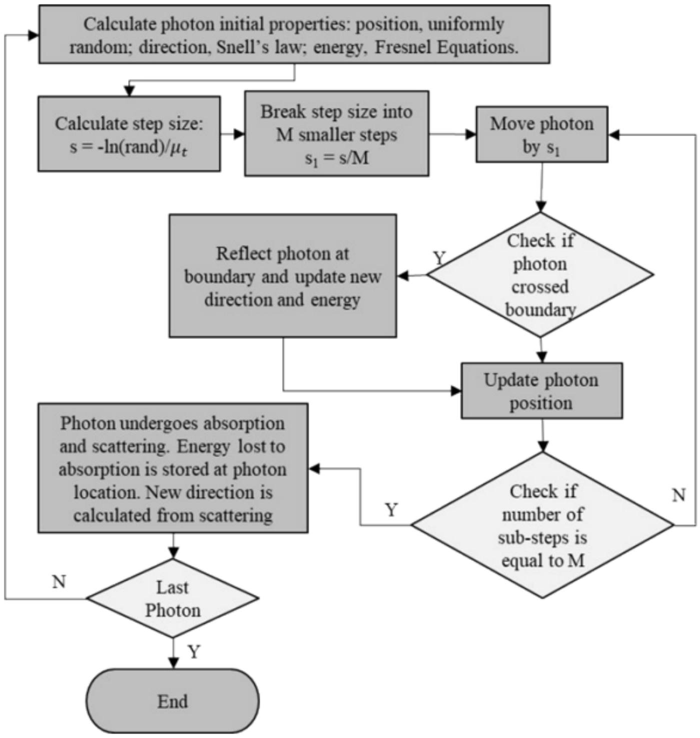

Figure 5.1. The above figure shows the flowchart for a basic Monte Carlo photon transport algorithm. Variants of this algorithm are used throughout this chapter, as well as in chapter 4.

5.2.1 *Photon Step Size and Absorption*

The two key fundamental parameters governing Monte Carlo simulations of light transport in media are the absorption coefficient μ_a and scattering coefficient μ_s. The absorption coefficient can be thought up as the reciprocal of the absorption mean-free path of the photon, that is, $1/\mu_a$ gives the expected value for the distance a photon travels before being absorbed. At absorption the photon is converted to thermal energy, which propagates via conduction through the medium, or is reemitted as an infrared photon to likely be reabsorbed by the media. For our purposes, we only consider the first case. The scattering coefficient likewise gives the scattering mean-free path, whereby the photons trajectory is expected to change every $1/\mu_a$ length units the photon propagates. The combined effect of both absorption and scattering is characterized by the attenuation coefficient $\mu_t = \mu_a + \mu_s$, where $1/\mu_t$ is the mean free path length before either scatter or absorption occurs. This attenuation coefficient gives us a basis for calculating the step size a photon should take before interacting with the medium. Based on the definition of μ_t, the probability $P(s)$ of a photon either scattering or absorbing in a distance traveled s is:

$$P(s) = 1 - \exp(-\mu_t s) \tag{5.1}$$

Clearly, this is not a constant function of s, but if we assume a uniform probability distribution for $P(s)$ then we arrive at the following expression for s:

$$s = -\frac{\ln(\mathrm{X}_{[0,1]})}{\mu_t} \tag{5.2}$$

We now have a distribution to sample from for photon step size that follows the laws of optics. After taking this step, the photon may either be scattered or absorbed. One approach, the *binary approach*, would simply to either absorb the photon at the end of the step or scatter it so it then moves in a different direction. It would not be incorrect to carry out the simulation this way; however, it generates an undesirable amount of noise, requiring post-processing and excessive computational time generating extra photons to compensate for the noise. A more elegant approach is to consider the photon to have a *well* of energy from which loss from absorption can be taken from. In this approach, the photon both scatters and is absorbed at the end of each step, only losing a part of its energy to the surrounding environment. The proportion of energy lost after each absorption even is the ratio of the absorption coefficient and the attenuation coefficient. Thus, the photons energy before E and after E' the absorption event is:

$$E' = \frac{\mu_a}{\mu_t} E \tag{5.3}$$

5.2.2 *Photon Flux and Laser Profile*

The laser can be characterized by its fluence rate $\varphi(x, y, z)$, which gives the energy density of the laser in the beam as a spatial function, where the z-axis marks the propagation axis of the laser. In practice, the laser beam is usually collimated, or at least focused such that there is an insignificant change in fluence rate for changes in the sample being irradiated. Thus, we can ignore in $\boldsymbol{\varphi}$ over the z-direction. Additionally, laser beam is almost always radially dependent, and thus fluence rate can be reduced to a function of the radius of the beam, $\varphi(r)$. The functional form of the profile for $\varphi(r)$ may take a variety of forms based on filters applied to the laser; however, the most common beam profiles are either constant (top-hat) or gaussian (normal curve). We consider both types of profiles in this study but choose to focus on the top-hat profile, since there is the least number of unknowns when calculating what the average fluence rate should be. Since the Monte Carlo profile involves firing photons, we must convert the fluence rate into the photon flux $J_p(r)$ by using the energy, or wavelength via the Planck relation, of the photons being fired.

$$J_p(r) = \frac{\lambda \varphi(r)}{hc} \tag{5.4}$$

We can avoid using the refractive index n since the photons are propagating through air (n ~ 1) prior to entering the sample.

5.2.3 *Domain and Boundary*

The shapes of the samples being laser warming during cryopreservation are either spherical or hemispherical due to the symmetric nature of surface tension on the encompassing droplet of CPA. Typically, the wetting angle of the CPA on the surface it sits on is not 90 degrees and can vary depending on surface chemistry and CPA type. For other conditions the droplet may be modeled as a chord-area intersecting a sphere, a so-called *semisphere*. Due to the spherical nature of the boundary, it is convenient to represent the boundary in terms of spherical coordinate parameters. Additionally, for easy of computation, it is also convenient to represent the boundary as a vector function. The boundary $\overrightarrow{\Omega}$ can be represented by:

$$\overrightarrow{\Omega} = \langle Rsin(\varphi)cos(\theta), Rsin(\varphi)sin(\theta), Rcos(\varphi)\rangle \tag{5.5}$$

Where R, is the droplet raidus, while φ and θ are the azimuth and zenith parameters in spherical coordinates. We can also define the normal boundary function $\overrightarrow{\Omega}_n$:

$$\overrightarrow{\Omega}_{\mathrm{n}} = -\frac{\overrightarrow{\Omega}_{\varphi} \times \overrightarrow{\Omega}_{\theta}}{\sqrt{\|\overrightarrow{\Omega}_{\varphi}\|^2\|\overrightarrow{\Omega}_{\theta}\|^2 - \|\overrightarrow{\Omega}_{\varphi} \cdot \overrightarrow{\Omega}_{\theta}\|^2}} \tag{5.6}$$

Where $\overrightarrow{\Omega}_{\varphi}$ and $\overrightarrow{\Omega}_{\theta}$ are the partial derivatives of $\overrightarrow{\Omega}$ with respect to φ and θ.

5.2.4 *Photon Launch*

From the domain we now start to launch the photons into the system. A random point within the cross-section of the beam is chose and the photon is placed at that point on the boundary that intersects that point on the beam. To do this, special care should be taken to ensure that the point chosen is indeed randomly sampled over a disc.

Once the photon finishes its new step it then has a change in direction according to the scattering anisotropy. Given the radius of the droplet R, a random point (x, y, z) on the droplet can be determined.

$$\theta = 2\pi X_{[0,1]} \tag{5.7}$$

$$R_{rand} = R^2 X_{[0,1]} \tag{5.8}$$

$$x = \cos(\theta)\,\sqrt{R_{rand}} \tag{5.9}$$

$$y = \sin(\theta)\,\sqrt{R_{rand}} \tag{5.10}$$

$$z = \sqrt{R^2 - x^2 - y^2} \tag{5.11}$$

From here we must calculate the interaction with the boundary that causes the light to bend as it enters the droplet since the air and droplet have different indexes of refraction.

5.2.5 *Initial Photon Trajectory*

Due to the local curvature of the droplet, as well as the differences in the refractive indexes between the air and droplet, both the photon's energy and trajectory change as it enters the droplet. Given an incident trajectory $\vec{d}_i = \langle 0{,}0,-1\rangle$, since the photon is traveling straight down at the droplet, we can calculate the transformed trajectory $\vec{d}_t = \langle ux, uy, uz\rangle$.

$$\vec{d}_n = \overrightarrow{\Omega}_{\mathrm{n}}(x,y,z) \tag{5.12}$$

$$\theta_i = \mathrm{mod}(\arccos(\vec{d}_i \cdot \vec{d}_n), \pi/2) \tag{5.13}$$

$$\varphi_i = \arcsin\left(\frac{n_i}{n_t\, sin(\theta_i)}\right) \tag{5.14}$$

$$v = -\vec{d}_n \times \vec{d}_i \tag{5.15}$$

$$\vec{d}_t = -\vec{d}_n \cos(\varphi_i)\left[v \times -\vec{d}_n\right] + (1 - \cos(\phi_i))(v \cdot \vec{d}_n) \cdot \vec{d}_n \tag{5.16}$$

Where n_i and n_t are the refractive index of air and the droplet respectively.

Due to reflectance, there is also an associated energy loss with both passing through a boundary and reflecting internally off one. This loss is related to the reflectance and can be determine from the Fresnel Equations.

5.2.6 *Fresnel Equations*

The transmittance t and reflectance r can be determined by the Fresnel equations below. Given an angle of incidence θ_i and angle of transmittance θ_t, along with indexes of refraction n_i and n_t then from Snell's law we have

$$n_i \cos(\theta_i) = n_t \cos\,(\theta_t) \tag{5.17}$$

Then we can determine the reflectances and transmittances:

$$r_s = \frac{n_i \cos(\theta_i) - n_t \cos(\theta_t)}{n_i \cos(\theta_i) + n_t \cos(\theta_t)} \tag{5.18}$$

$$r_p = \frac{n_i \cos(\theta_t) - n_t \cos(\theta_i)}{n_i \cos(\theta_t) + n_t \cos(\theta_i)} \tag{5.19}$$

$$t_s = \frac{2n_i \cos(\theta_i)}{n_i \cos(\theta_i) + n_t \cos(\theta_t)} \tag{5.20}$$

$$t_s = \frac{2n_i \cos(\theta_i)}{n_i \cos(\theta_t) + n_t \cos(\theta_i)} \tag{5.21}$$

The subscripts s and p indicate the parameters for s-polarized and p-polarized light. Since we are considering an unpolarized laser, then we have the total transmittance and total reflectance:

$$t = t_s + t_p \tag{5.22}$$

$$r = r_s + r_p \tag{5.23}$$

Thus, the energy of the photon before E and after E' entering the droplet is

$$E' = tE \tag{5.24}$$

5.2.7 *Scattering and Updating Position and Trajectory*

After the photon is fired, it first enters the boundary and then calculates a new trajectory from its old trajectory due to scattering. The frequency of scattering is determined by the magnitude of the scattering coefficient while the angle of scattering is determined from a probability distribution based on the scattering anisotropy g. When a photon takes a new step, it updates its position and trajectory.

$$x = x + s\ ux \tag{5.25}$$

$$y = y + s\ uy \tag{5.26}$$

$$z = z + s\ uz \tag{5.27}$$

Since the trajectory vector $\langle ux, uy, uz \rangle$ is normalized this recovers a step size of s. After absorption a new trajectory is calculated corresponding to the scattering anisotropy g and scattering angle θ_s.

$$\theta_s = \arccos\left(\frac{1+g^2-\left(\frac{1-g^2}{1-g+2gX_{[0,1]}}\right)^2}{2g}\right) \tag{5.28}$$

Since scattering is inherently symmetric the azimuthal scattering angle φ_s is simply:

$$\varphi_s = 2\pi \mathrm{X}_{[0,1]} \tag{5.29}$$

The updated trajectory $\langle ux, uy, uz \rangle$ can now be calculated.

$$ux = \frac{\sin(\theta_s)\left(ux\ uz\cos(\varphi_s) - uy\ sin(\varphi_s)\right)}{\sqrt{1-uz^2}} + ux\cos(\theta_s) \tag{5.30}$$

$$uy = \frac{\sin(\theta_s)\left(uy\ uz\cos(\varphi_s) - ux\ sin(\varphi_s)\right)}{\sqrt{1-uz^2}} + uy\cos(\theta_s) \tag{5.31}$$

$$uz = \ -\sin(\theta_s)\cos(\varphi_s)\sqrt{1-uz^2} + uz\cos(\theta_s) \tag{5.32}$$

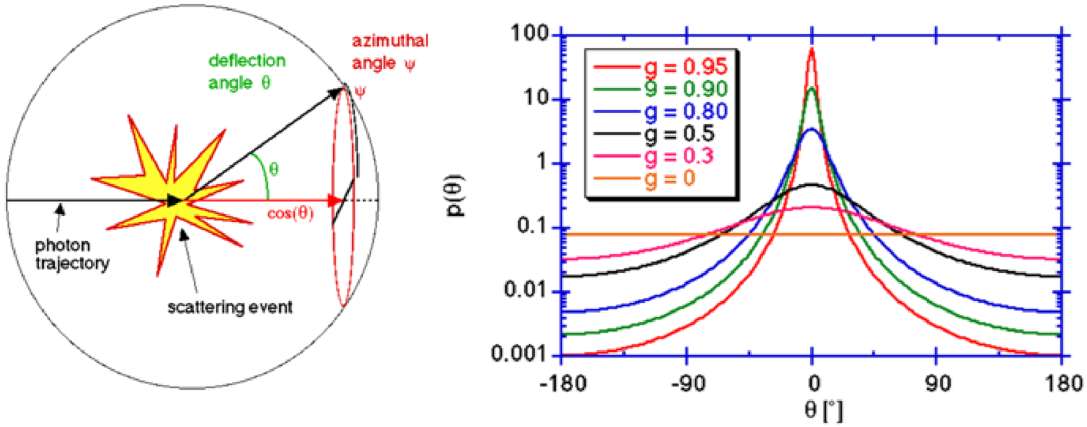

Figure 5.2. Diagram showing how scattering occurs during the photon transport simulation and how the scattering anisotropy factor affects the scattering angle.[137]

5.2.8 *Storing Energy and Photon Death*

So far, the photon will just keep propagating and loose more and more of its energy, so we must set some threshold where the photon is destroyed. This will inherently fail to conserve the energy of the photons since some energy will be lost, so we will employ a roulette method.

Given some threshold $w \ll 1$, we will randomly generate a new photon on average once every $1/w$ photons launched. This acts to recover the lost energy from apply the energy threshold in the first place.

To store photon energy the domain is discretized. Then at every absorption event the energy lost due to absorption was stored in the domain bin corresponding to the location of the absorption event. The initial energy of the photon is not necessarily the actual energy via the Planck relation, since the lasers in question have J_p on the order of $10^{25}\ m^{-2}s^{-1}$. Instead, we use the energy scale factor f_s to relate the laser photon energy E_p to the simulation photon energy E_s.

$$E_s = f_s E_p = \frac{f_s hc}{\lambda} \tag{5.33}$$

Thus, when the photon is fired it has an initial energy of E_s, and an initial weight of $w = 1$. At each absorption event the energy of the photon and the weight both drop by equation (5.3), likewise for other energy loss events such as boundary interactions.

5.2.9 *Interaction with Boundary*

At some point the photon will interact with the boundary as it did when it entered the droplet. For cases like this, the photon position suddenly transitions from within the domain to outside the domain. If $(x, y, z) \in \neg\Omega$, then calculate the point along the previous trajectory where the photon made contact with the domain. That is

$$\begin{aligned} &\text{if: } (x, y, z) \in \neg\Omega \\ &\text{then: } \textit{find } \{s' \mid (x + s'ux, y + s'uy, z + s'uz) \in \Omega\} \end{aligned}$$

Once s' is determined then the reflected trajectory $\vec{d}_e$ is.

$$\vec{d}_i = \langle ux, uy, uz \rangle \tag{5.34}$$

$$\vec{d}_n = \overrightarrow{\Omega}_n(x, y, z) \tag{5.35}$$

$$\vec{d}_e = -(\vec{d}_i \cdot \vec{d}_n)\vec{d}_n +\cdot\, \vec{d}_i \tag{5.36}$$

With the photon energy before E and after E' the reflection as

$$E' = rE \tag{5.37}$$

Where r is the reflectance (5.23) from 5.2.6.

The new photon position is

$$\langle ux', uy', uz' \rangle = \vec{d}_e \tag{5.38}$$

$$x = \ x + s'ux + (s - s')ux' \tag{5.39}$$

$$y = \ y + s'uy + (s - s')uy' \tag{5.40}$$

$$z = \ z + s'uz + (s - s')uz' \tag{5.41}$$

Finally,

$$\langle ux, uy, uz \rangle = \langle ux', uy', uz' \rangle \tag{5.42}$$

In summary, the photon took a step outside the boundary. So first, the distance to the boundary and point where the photon intersected it was calculated. Next, the new trajectory was calculated via spectral reflection off the boundary. Then, the loss due to partial transmittance was applied to the photon energy. Next, the photon continued for the remain portion of its initial step in the new reflected trajectory. Finally, the new trajectory and positions were updated.

5.2.10 *Adjusting Step Size for Multi-Boundary Systems*

It should be apparent at this point that the scheme above works well for large domains relative to the step size taken by photons. If, however, this is not the case, the algorithm does not properly simulate the environment. For example, consider Figure 5.3 below, where a photon takes a step between domains Ω_1 and Ω_3.

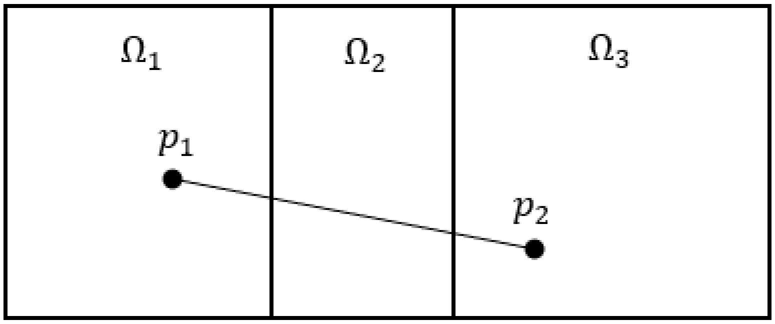

Figure 5.3. A photon traveling between domains Ω_1 and Ω_3 with a step size that is too large. This shows the error that can arise when the step size in a MC photon transport simulation is too large in a system with multiple domains.

It is clear that the step size was too large, in fact, the variable step size described by equation (5.2) is not appropriate. In these situations, there are a few choices. The first, is to choose a constant step size scheme, with step size $s_{constant}$, such that $s_{constant}$ is smaller than the minimum length scale in all of the domains.

$$s_{constant} < \text{minimum length scale in } \Omega_{\text{i}} \tag{5.43}$$

This scheme is prohibitively expensive though, a more reasonable scheme is to tag each photon with the domain it is currently in and determine if it crossed a boundary in the domain, i.e., the tag changed from one domain to another. If there is a crossing between domains, then the step size is reduced, and absorption values adjusted accordingly so that the true path of the photon is realized throughout the domain. This still has a flaw though. Depending on the geometry of the domain, it is possible that a photon skips over a domain entirely and arrives back it its original domain. In cases where this has a significant change of happening, a constant step size may be the most suitable choice for the simulation. For modeling multi-compartment zebrafish embryo laser nanowarming, this constant step size is used do to the complex and curved geometry.

5.2.11 *SAR and Generating Temperature Profiles*

The output of the Monte Carlo simulation is a three-dimensional heat source function (the specific absorption rate or SAR). This in its own can be used to assess a variety of characteristics about the laser warmed system such as SAR uniformity, hotspots, and boundary layers. Though this may be helpful, a proper understanding of the actual temperature profile in the laser warmed droplets gives a more complete picture. To calculate the temperature profile, we used the SAR profile as a heat source function to the heat equation (5.44) which was solved by the finite element software COMSOL, where the values of all parameters are temperature (and thus spatially) dependent.

$$\rho c_p \frac{\partial T}{\partial t} - \Delta \cdot (k \Delta T) = SAR \tag{5.44}$$

The geometry of the droplet was also built in COMSOL to match that used in the corresponding Monte Carlo simulation. Since we are modeling droplets of CPA and CPA loaded biological specimens, we need the temperature dependent values for the specific heat c_p, density ρ, and thermal conductivity k. We use the temperature dependent properties of 2M 1,2-propanediol, a common cryoprotectant, outlined by Choi et al (2008).[138] These parameters have values in the following ranges: c_p~$1768 - 4019 \frac{J}{kg\ K}$, k~$.35 - .5 \frac{W}{m\ K}$, and ρ~$900 - 1000 \frac{kg}{m^3}$.

5.3 Simulation Results

Several scenarios were simulated via Monte Carlo to gain insight into the laser warming process. Throughout this section we will go over the laser warming of millimeter-scale droplets and of cryoprotectant solution and gold nanoparticles (with or without biological specimens), showing how droplet shape, size, contents, and photothermal properties affect the SAR profile. In Chapter 4, we relate these simulations to laser calorimetry experiments to help validate both the model and the experimental methods.

5.3.1 *Laser Warming of a Hemispherical Droplet on a Cryotop*

A cryotop is a thin piece of low thermal mass plastic in which a droplet of CPA laden with or without biological samples is placed during some cryopreservation processes. The geometry of the cryotop-droplet system can be seen in Figure 5.4 below.

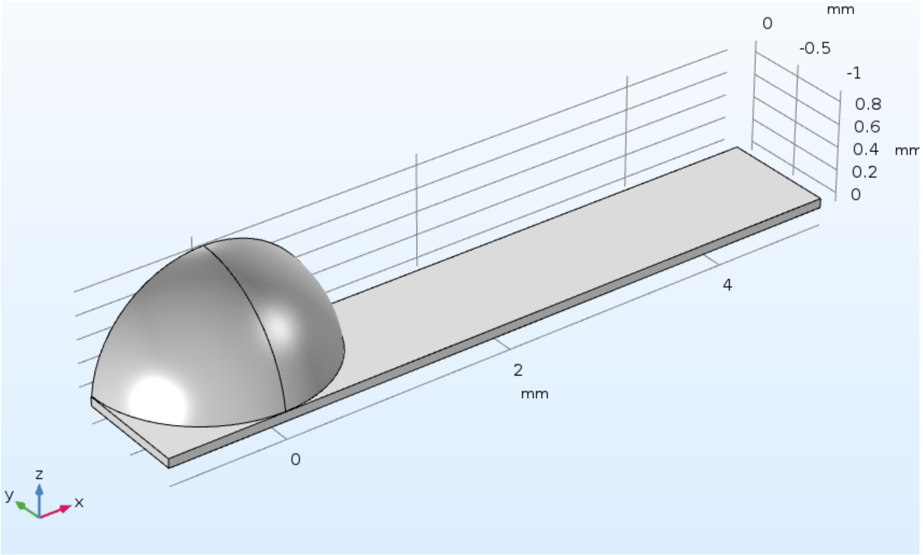

Figure 5.4. A symmetric cross-section of the geometry of a cryotop with a hemispherical 1 mm droplet on its end.

To test the validity of the model we first compared the simulations to known limiting cases of light transport, specifically to the Beer-Lambert law equation (5.45) and to the diffusion limited high-scattering approximation equation (5.46), Where A is some domain-specific constant relating to the reflectance, and thus the index of refraction. The indexes of refraction were matched between the droplet at the surrounding environment to eliminate any effects of reflectance.

$$SAR(z) = \mu_a \varphi \exp(-\mu_a z) \tag{5.45}$$

$$SAR(z) = \mu_a \varphi A \exp(-\sqrt{3\mu_a(\mu_a + (1-g)\mu_s)}z) \tag{5.46}$$

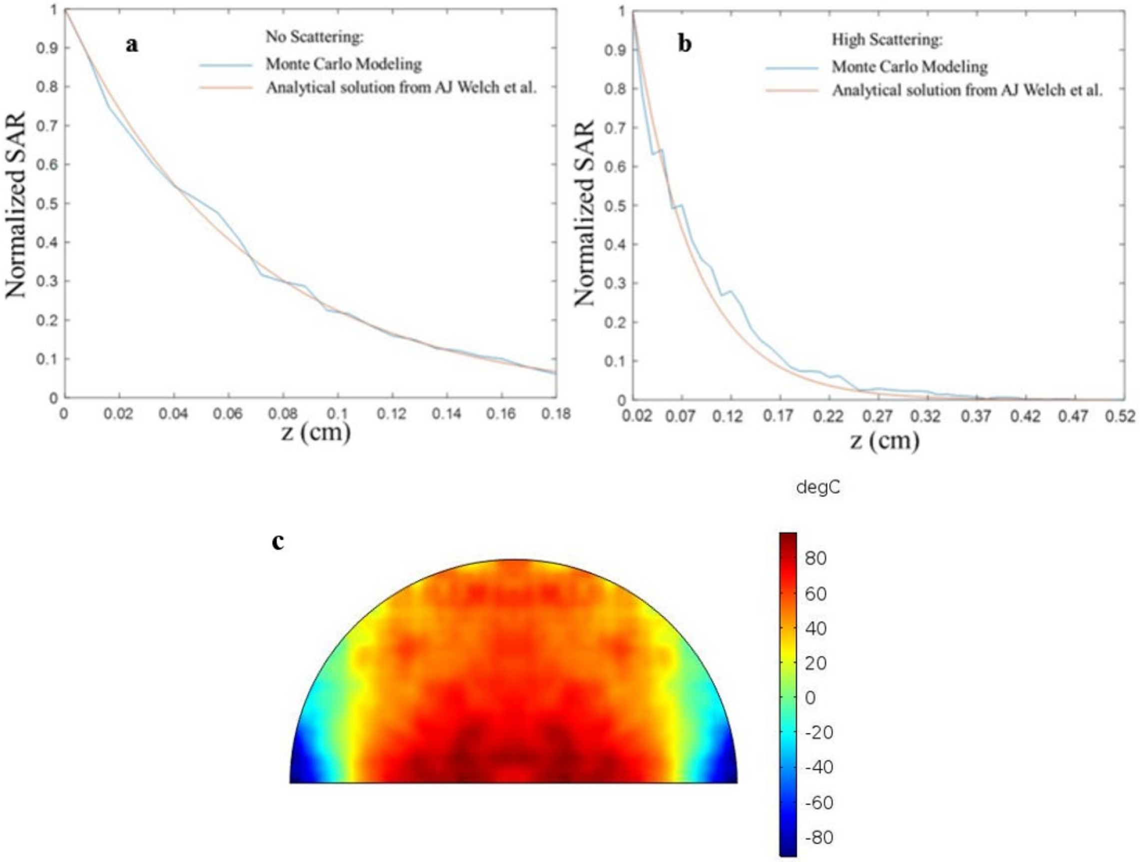

Figure 5.5 Monte Carlo simulations without scattering compared for Beer's Law (a), and with dominant scattering compared to the diffusion approximation (b). **(c)** Temperature profile post warming in a droplet subjected to laser warming.

We see strong agreement between the simplified cases with no and high scattering to Beer's Law and the diffusion approximation in Figure 5.5(a) and (b). This gives us confidence that the model is working correctly and thus we can trust it's outputs in more complicated systems. In Figure 5.5(c), we see the temperature profile of a typical laser warmed hemispherical droplet. Notice that the edges remain very cold, this is because of the large difference between the indexes of refraction of air and the droplet. This causes incoming light to bend as it makes contact (from above) with the droplet. The angle of incidence of the laser on the droplet determines the degree of bending and also the ratio of transmitted to reflected light. This combination of low transmittance and inward bending of the laser

c

causes these areas of low warming to occur. In the next section we perform an optimization study on the absorption and scattering coefficients in order to determine the values that lead to the most uniform temperature profile post-warming.

5.3.2 *Optimizing Photothermal Properties for Uniform SAR*

In this section we examine the roll that the scattering and absorption coefficients have in the overall SAR profile, by considering the mainly absorptive effects of gold nano rods (GNRs) and absorption and scatter effects of gold nanoshells (GNSs). We consider a hemispherical droplet that is 1mm in radius and subject it to a .5ms laser pulse. The various other parameters are listed in Table 5.2.

A simulation of laser warming of a droplet on a perfectly reflective cryotop was carried out per the parameters in Table 5.2. The boundary condition applied at the underside of the droplet was a perfectly reflective boundary condition with no transmittance, no energy loss, and no scattering (normal or diffuse). This was done to simulate the warming of a droplet on a mirror to maximize the amount of laser energy absorbed by the droplet. The scattering and absorption coefficients were measured via the cuvette method outlined in Liu et al. (2020). The scattering anisotropy factor of the GNRs was assumed to be 0.25, which was obtained by fitting the experimental angular scattering data in the reference work, with the Henyey-Greenstein phase function for GNRs with sizes close to those used in this study.

Table 5.2. A summary of input parameters in the two Monte Carlo models for the cuvette experimental data analysis and laser warming of a GNP-loaded droplet simulation. *Measured values; **Assumed values. The other unmarked values are either known constants or derived from the measured or assumed values. The choice of scattering anisotropy factors for different GNPs is explained Liu et. al. (2020).[116]

PARAMETERS	**DESCRIPTION**	**VALUES**
n_d	Refraction index of solutions	1.35[139] (droplet)
n_a	Refraction index of air	1.00
r_a	$1/e^2$ radius of Gaussian beam (mm)	1 *
φ	Laser energy density (W/m^2)	1.83×10^9 *
PW	Pulse width of laser beam (ms)	0.5*
E_p	Photon energy at 1064 nm (eV)	1.211
$N_{photons}$	Flux of photons ($\frac{\#}{m^2 \cdot s}$)	I_0/E_p
μ_t	Attenuation coefficient of GNP solutions	$\mu_a + \mu_s$
μ_a	Absorption Coefficient of GNP solutions	5 cm^{-1}**
μ_s	Scattering Coefficient of GNP solutions	0.3 cm^{-1} (GNR) ** 11 cm^{-1} (GNS) ** or other assume values
γ	Ratio of scattering to absorption	μ_s/μ_a
g	Scattering anisotropy factor	0 (GNS)[140] ** 0.25 (GNR)[141] **

When modulating the absorption and scattering coefficients in this study, a linear average of the absorption and scattering properties of the GNR and GNS solutions located in Table 5.2 were used. Increased concentration was assumed to be a linear scaling up of both the absorption and scattering coefficients. Many simulations were carried out at various concentrations of GNR and GNS to determine the effect that scattering, absorption, and their relative ratio relative to the size of the droplet had on the warming uniformity within the droplet. A new parameter, γ, defined the ratio of the scattering coefficient, to the absorption coefficient.

In COMSOL simulation, the thermal properties of 2M (20.15 wt%) PG were used to simulate the thermal properties of a CPA laden droplet. The thermal conductivity, specific heat, and density of the liquid CPA solutions were calculated by the weighted average. As for the vitreous status, the thermal conductivity and density were assumed as constant from room temperature to the vitreous status. This assumption is based on the reported findings that thermal conductivity of a vitreous glycerol. and the density of other vitreous CPA solution keep almost constant during vitrification. For specific heat, however, there can be a ~ 56% jump during the vitrification transition. The transition temperature of the 2M PG was assumed to be -105 °C.

The results of the laser warming simulations can be seen in Figure 5.7. We see that for GNR alone (a), we have an extreme hotspot near the top of the droplet, corresponding to the reflected focus of the bent laser light entering the high refractive index droplet. We see, with the introduction of higher scattering (b), that the hotspot is diminished substantially. The optimal ratio of scattering to absorption is depicted in (c), which lacks a hotspot all together. Finally, in (d), we see that too much scattering can lead to poor penetration into the droplet, frequent photon scattering hinders penetration and causes them to stay near the surface, increasing the temperature near the boundary but leaving the interior of the droplet cold. In (e) and (f) we see the normalized standard deviation of SAR, a metric for temperature uniformity, whereby we can determine the γ value corresponding to the most uniform combination of the absorption coefficient and scattering coefficient, given the constraints of linking them to measured data for GNRs and GNSs. In (g) we see the optimal γ value as a function of the dimensionless constant $\mu_a R$, which is the ratio of the mean free path of photon absorption to the diameter of the droplet. We see γ decay exponentially with increasing $\mu_a R$.

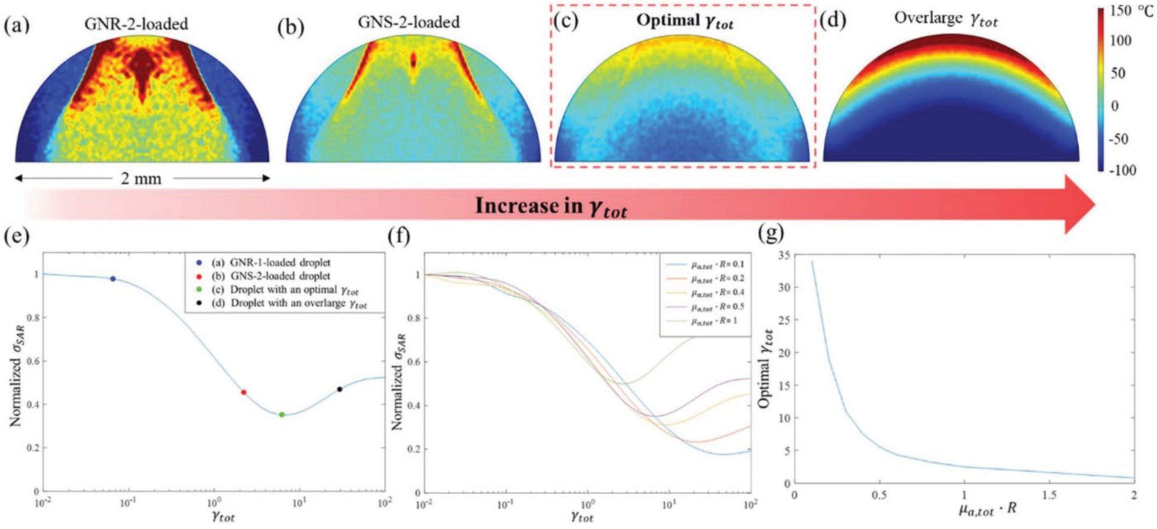

Figure 5.7. Predicted temperature profiles of the vertical central cross-sections in the laser-warmed 2 mm-diameter hemispherical droplets at the end of the 0.5ms laser pulse irradiation from the top of the droplet. (a) The temperature profile in the droplet loaded with GNR-2 at the end of the pulse with $\mu_a = .5\ cm^{-1}$, $\gamma = 0.06$. (b) The temperature profile in the droplet loaded with GNS-2 at the end of the pulse with $\mu_a = .5\ cm^{-1}$, $\gamma = 2.2$. (c) The temperature profile in the droplet at the end of the pulse assumed with an optimal γ where $\mu_a = .5\ cm^{-1}$, $\gamma = 5.5$. (d) The temperature profile in the droplet at the end of the pulse with an overlarge γ where $\mu_a = .5\ cm^{-1}$, $\gamma = 30$. (e) Normalized SAR, as an indicator of the uniformity of laser warming, changes with the optical γ of the droplet with the μ_a set constantly at $5\ cm^{-1}1$. The SAR was normalized by the value at $\gamma = 0.01$. (f) Normalized SAR changes with the optical properties γ and $\mu_a R$ of the hemispherical droplet. The σSAR was normalized by the value at $\gamma = 0.01$. (g) The optimal γ of the hemispherical droplet for each μ_a to achieve the lowest normalized SAR (i.e., the most uniform heating temperature profile).[116]

5.2.3 *Laser Warming of a Spherical Droplet*

Along with hemispherical droplets, there is a need for laser warming spherical droplets of vitrified material as well. Since a sphere is the most compact three dimensional shape, it is the ideal shape for uniform and rapid cooling. Additionally, it lends itself to easy printing and maneuverability in the vitrified state.

A 40 µL droplet of CPA was vitrified, and laser warmed while under high-speed video. Still shots of the video can be seen in Figure 5.8 while the corresponding temperature profile is given in the bottom-right, given the laser pulse energy and absorption properties of the GNRs used. The model captures the hotspot at the bottom of the droplet, seen top-right, where the laser is focused by the droplet into a small region at the bottom of the droplet. Light bent away from the loser edges causes cold spots around the bottom outer shell of the droplet which manifests itself as ice since it was not brought up to the melt temperature in time.[142]

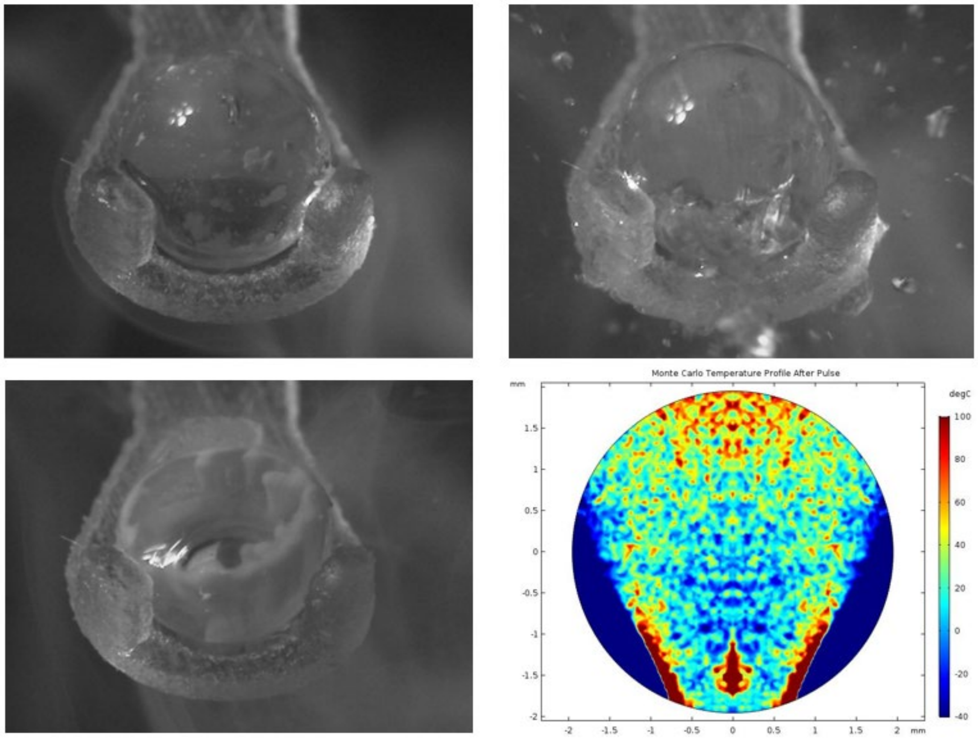

Figure 5.8. Top left: 40 µL vitrified droplet of 2M propylene glycol + 1M trehalose with GNR prior to laser warming. Top right: droplet during laser warming (note the boiling at the bottom of the droplet). Bottom left: droplet immediately after laser warming (note the shell of ice around the bottom of the droplet). Bottom right: temperature profile after laser pulse from Monte Carlo and finite element heat transfer model of laser warming (note that lensing causes a hotspot at the bottom and under warmed shell around the bottom half).

5.2.4 *Laser Warming of Zebrafish Embryos*

A more complex system modeled is the laser warming of a droplet-encapsuled zebrafish embryo. These embryos have complex geometries with a high scattering yolk in the center that acts as a shield to laser penetration. Fortunately, the only necessary parts of the embryo required to be warmed under ideal conditions are the cells composing the "head" of the embryo. This study used the Monte Carlo model to accompany the cryopreservation and laser warming of zebrafish to better understand the effects of rapid laser warming on the vitrified embryos. These zebrafish serve as a model organism for a vast array of aquatic organisms and are thus of high importance as they serve as a template for cryopreservation of many aquatic systems.

In this study. zebrafish embryos were injected via micro-pipette with a GNR and CPA solution to aid in vitrification and rewarming, outlined in Figure 5.9. Preserved embryos were imaged under a high-speed camera as they were laser warmed to study the dynamic effects of laser warming. We have found that there is significant warming in the surrounding droplet, but limited warming in the embryo yolk. Thus, to entirely rewarm the embryo, such a high laser power and pulse width were needed that the surrounding CPA-GNR droplet was vaporized in the process. This seemed to be centered at the top of the embryo. Multiple trials have confirmed this phenomenon, which could be attributed to several causes, including nonuniform distribution of laser absorption in the embryo or GNR and CPA leaking out of the embryo. To address this issue of large thermal gradients in the embryo a Monte Carlo model of light interaction with the system was constructed which considered absorption, scattering, refraction, and reflection. The absorption coefficient and scattering coefficients of GNR-CPA solution used for vitrification and rewarming were measured via methods outlined in Liu et. Al (2020) and determined to be 4.54 cm^{-1} and .05 cm^{-1} respectively while the scattering anisotropy coefficient was assumed to be .25, though the scattering coefficient was so low it had a negligible effect on the warming profile. Since the head containing the cells in the embryo was permeable to GNR and CPA, it too was given these properties. The absorption coefficient of the yolk was assumed to be identical to the droplet as the microinjection system controlled for this. The scattering coefficient and anisotropy coefficient were estimated to be 70 cm^{-1} and 0.70 respectively.[143] There is great uncertainty around these numbers since in egg yolk, and presumably zebrafish embryo yolk, the scattering coefficient changes with the denaturing of proteins. It is also unknown how vitrification, or crystallization, effects the optical properties of yolk. These parameters were then imputed into a Monte Carlo program that outputted the spatially dependent specific absorption rate throughout the system. This profile was then imputed into COMSOL Multiphysics and used, along with the thermal properties of the system constituents, to estimate the temperature profile in the system. This was then compared to a Beer's Law model of absorption.

Figure 5.9. Overview of the cryopreservation and laser warming process. Our new single injection protocol begins with the microinjection of CPA (PG and MeOH) and GNRs into the yolk of a zebrafish embryo reaching the high cell stage. After a recovery period of 2 h, the injected embryos are placed in a precooling bath for 5 min to dehydrate the perivitelline fluid. Immediately after, the embryos are placed on a polypropylene strip called a cryotop and plunged into liquid nitrogen. After equilibration to −196 °C, the embryo is brought under the laser for warming. After warming, the embryo is placed in a post-warming washout bath for rehydration and CPA removal from the perivitelline fluid, after which the embryo is placed in embryo medium and stored in an incubator at 28 °C. Embryo development was monitored regularly up to 5 days. Select embryos surviving to Day 5 were transferred to a separate housing where they reach spawning age. Once sexual maturation is reached, the adult zebrafish are spawned with the corresponding transgenic zebrafish adults.[130]

The modeling shows that there are significant temperature gradients in the system, more than were previously thought. Lensing of the laser by the droplet causes cold spots to arise at the periphery while the high scattering environment of the yolk leads do under warming below the yolk, and hot spots near the top of it. This leads us to believe that using a more uniform laser profile around the embryo would lead to lessen these thermal gradients. A more uniform SAR profile could then be achieved by using multiple lasers hitting the droplets from multiple sides. Figure 5.10 shows the result of laser warming of the embryo via Monte Carlo to using Beer's law, showing the necessity of more complicated simulations when difficult geometry and scattering are involved.

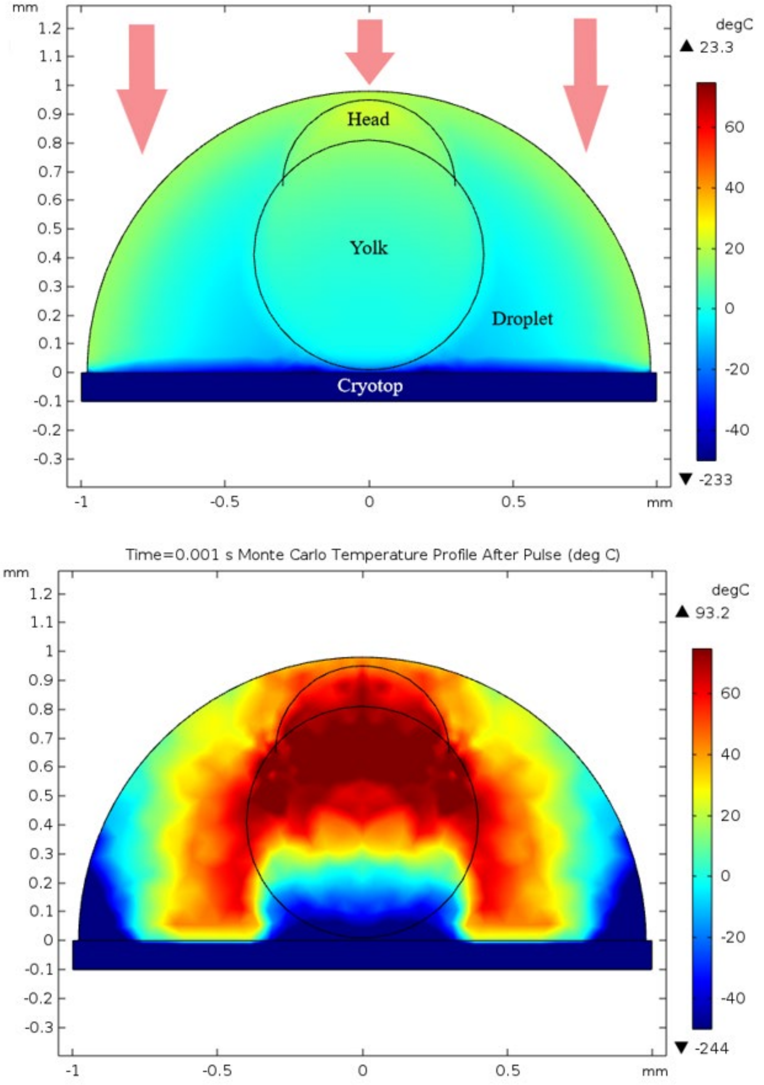

Figure 5.10. (Top) The temperature profile in a droplet encased zebrafish embryo after a 1ms laser pulse. This assumed a Beer's Law distribution of light in the system that only considered absorption. The laser profile was uniform across the embryo and is represented by the red arrows above. (Bottom) Monte Carlo simulation of the same embryo.[130]

5.3.5 *Laser Warming in Coral Nanofragments*

The rapid deterioration of coral reefs around the world's oceans is a direct consequence of rising temperatures and ocean acidity associated with anthropogenic climate change. Coral reefs also house an immense quantity of the ocean's biodiversity, making them of utmost value to preserve as a hedge against ecological collapse. One such preservation method is to preserve millimeter scale coral nanofragments, which consist of a fleshy layer of coral tissue atop of skeleton of bone.

In this study, Monte Carlo simulations for light transport within droplet encompassed coral nanofragments were carried out following previously outlined protocols.[39,144] Additionally, diffusion theory was applied to CPA loading to estimate the concentration of CPA in the coral vs time during the CPA loading protocol. The coral nanofragment skeleton was modeled as a 50 µm thick disc of diameter 1.5 mm. A secondary skeletal structure sat atop this disk, which was modeled as ring of diameter 500 µm and height 200 µm. Tissue filled the ring cavity and sat atop the rest of the skeletal structure with a thickness of 50-100 µm. A 2 mm diameter hemispherical droplet of GNR loaded CPA encompassed the nanofragment. A cross section of the droplet and nanofragment can be seen in Figure 5.11. Thermophysical and optical properties of the coral skeleton were modeled after those of human bone while those for the coral tissue were modeled after PBS +2M glycerol loaded tissue. The Monte Carlo simulations were carried out for varying amounts of GNR in the tissue to model the worst, realistic, and best cases for warming corresponding to a GNR concentration of 0%, 50%, and 100% inside the tissue relative to the droplet GNR concentration. The Monte Carlo simulation results were then analyzed in COMSOL to generate the predicted temperature profiles in the droplet and nanofragment given the system parameters outlined in Table 5.3.

Table 5.3. Thermophysical and optical properties used in Monte Carlo light transport simulations and COMSOL Multiphysics FEM heat transfer analysis.

PROPERTIES	**COMPARTMENT**	**VALUE**	**REFERENCE**
Density	Skeleton	2.94 g cm^{-3}	[145]
Thermal Conductivity		0.58 W m^{-1} K^{-1}	[146]
Specific Heat		1260 J kg^{-1} K^{-1}	[147]
μ_a		0.2 cm^{-1}	[137]
μ_s		20 cm^{-1}	
Density	Tissue + CPA	1.00 g cm^{2}	water density
Thermal Conductivity		PBS+2M glycerol*	[138]
Specific Heat		PBS+2M glycerol ref*	
μ_a		0.5 cm^{-1}	[137]
μ_s		10 cm^{-1}	
g		0.94	

Simulation results for laser warming of the nanofragments are shown in Figure 5.11 and 5.13. From these we see that even for a moderate GNR uptake, where only 50% of the GNRs enter the coral, we see relatively favorable warming profiles, with much of the coral rewarmed well above the critical warming rate for the CPA. The warming rates generated throughout the coral were 100 times faster than those generated from convective warming, indicating that this laser warming method allows for much lower concentrations of CPA than convective methods. Figure 5.12 shows the CPA loading and unloading protocol, and the concentration as a function of tissue depth assuming a diffusion coefficient of 6×10^{11} m^2/s. This indicates that the concentration of CPA in the outer 100 µm tissue layer is at least 50% of the loading CPA concentration. It is worth noting that as the concentration equilibrates in the tissue the CPA will continue to diffuse until cryopreservation locks the concentration gradients into place. Additionally, the concentration is relatively past 100 µm in depth. Coupling this with the fact that warming rates in this region are also lower, indicates a layer of dead coral tissue along the bone-tissue laser in the calyx.

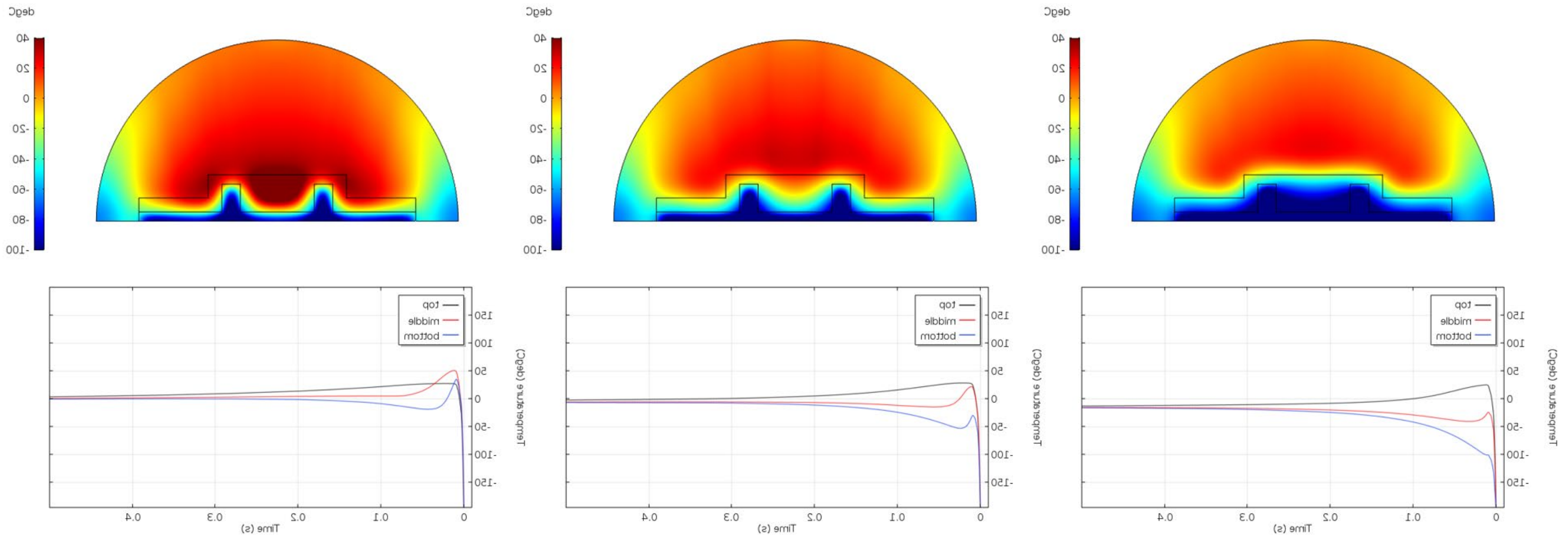

Figure 5.11. Temperature profiles immediately after laser pulse for coral nanofragments loaded with (a) no GNR, (b) 50% droplet GNR, and (c) 100% droplet GNR. (d), (e), and (f) show the temperature at the top, center, and bottom of the coral tissue corresponding to no GNR, 50% GNR, and 100% GNR respectively.

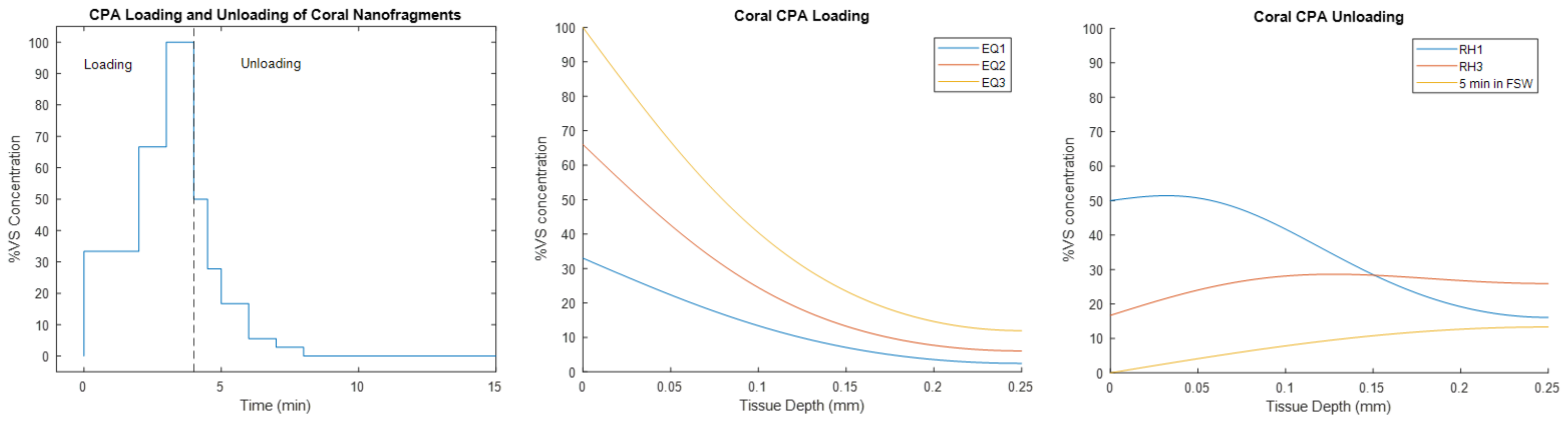

Figure 5.12 (a) CPA step loading protocol with CPA concentration in tissue after each (b) loading step and (c) unloading step assuming a diffusion coefficient of 6×10^{-11} m^2/s.

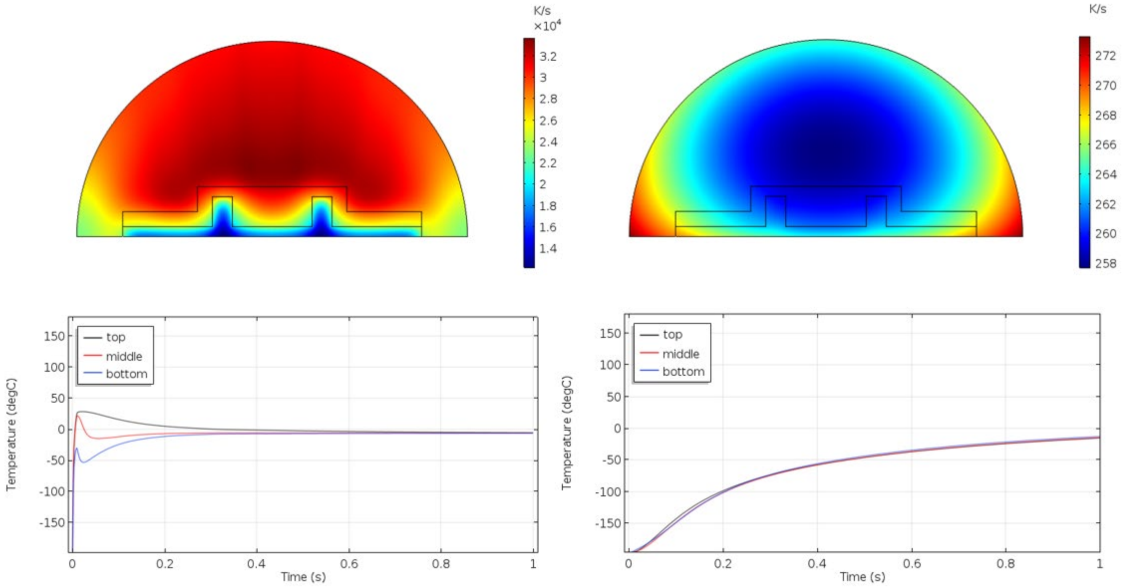

Figure 5.13. Warming rate profiles in the droplet for (a) laser warming (~30,000 K/s) and (b) convective warming in 300K water (~300 K/s) with (c) and (d) corresponding to the temperature at the top, middle, and bottom of the coral nanofragment for laser warming and convective warming respectively.

5.4 Optimizing Laser Warming Through Mirrors and Multiple Lasers

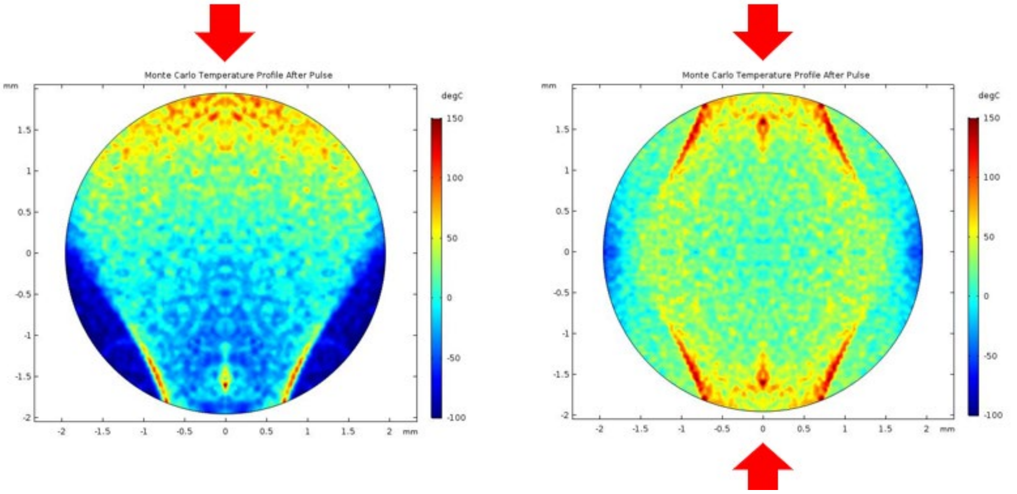

Figure 5.14 Laser warming on a spherical droplet with one laser (Right) and two lasers (Left)

Many systems that we may wish to cryopreserve and rewarm with laser warming will require droplets in excess of 4 mm in diameter, such as salmon embryos, or high numbers of specimens per droplets such as coral larvae and shrimp. Currently, this is not possible with the single beam laser warming system, due to optical constraints in the SAR profile in larger droplets. In this study, we model the results of using a beam splitter and mirrors to expand and manipulate the high-power laser pulse so that it hits the cryopreserved droplet from opposite sides, increasing the uniformity and volume of rewarmable material.

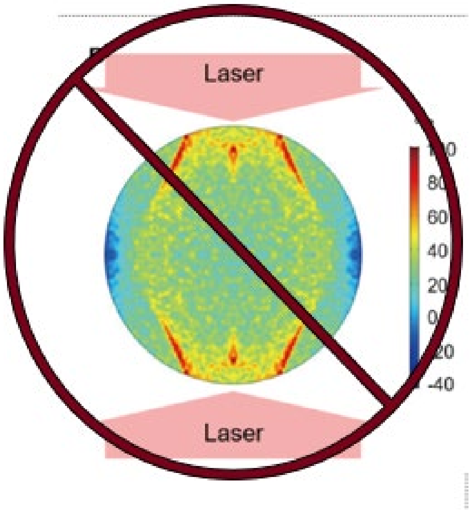

Figure 5.15. Model of laser warming for perfectly opposite lasers, which should be avoided due to reentering of beams into the laser. The goal instead must be to offset the beams slightly so that we can maximize uniformity while avoiding beams reentering the laser.

Several key design features need to be met for the system to function properly and safely. The peak power density of the laser in question is 0.2 MW/cm^2, meaning we need sufficiently durable optics to handle beam manipulation. This limits us to high energy Nd:YAG plate beam splitters. A one-inch diameter 1MW/cm^2 continuous wave beam splitter from Newport was selected, which gives us a buffer between the max laser fluence and damage threshold of the beam splitter. Note that increasing the beam diameter only makes damage less probable. One-inch diameter mirrors were selected from Newport with a damage threshold of 4.5 GW/cm^2 continuous wave, substantially higher than the power many commercial lasers can produce, including our own laser. We must be careful not to line up the beams directly across from one another so that they don't reconverge back at the laser. To solve this we propose offsetting the beams by about 10 degrees and having the beams termionate on absorbing pads so that the collimated beam doesn't continue indefinitly and cause damage or harm to someone or something.

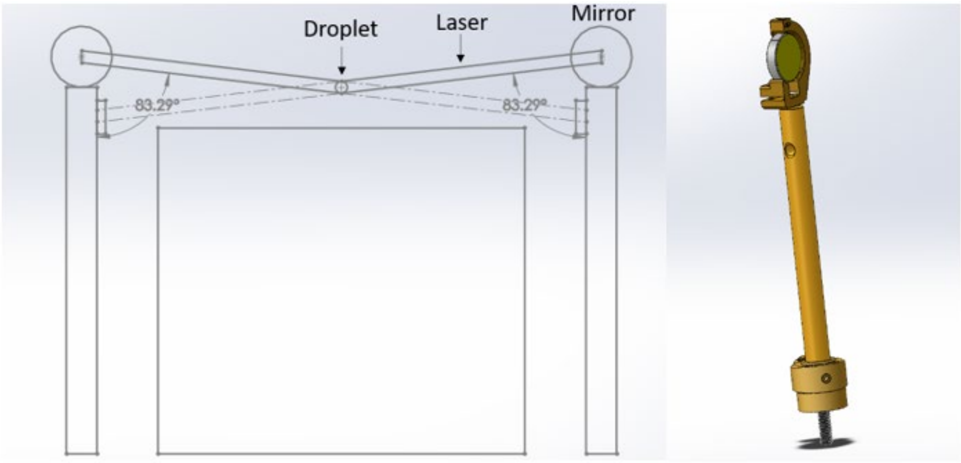

Figure 5.16. (Left) Schematic of lasers hitting the droplet as to no interest each other perfectly and reflect back into the laser. (Right) CAD model of laser mirror or beam splitter for horizontal-horizontal reflection.

Positioning of the mirrors and lining up all the optics will be accomplished by using a continuous wave lower power (10mW) 1064 nm laser so that we can adjust the optics without risking dangerous pulses from the high0power laser. Unfortunately, since the laser is invisible, the use of 1064 nm glowing cards will have to be used to determine where the beam is. We must also be very careful to keep the mirrors and beam splitter very clean, as dust or particulate may destroy the reflective coating if irradiated by the laser. This means regular proper cleaning per the manufacturer's instructions.

Another thing to consider is that the laser with the chamber open, and thus with the beam exposed, is a Class 4 laser. This is the highest class of laser, with the capability of burning the eyes or skin, leading to permanent damage from direct, diffuse, or indirect beam viewing. For this reason, as well as to keep the optics clean, an enclosure must be built around the open beams to make this system safe. An enclosure for our laser system need not be complicated. We can contain the system inside one large box, with holes cur through for the laser to emerge from, this will not just prevent the laser from doing damage to the surrounds, but also keep the optics clean from dust and debris from the environment, as well as prevent bumping the optics out of alignment. Laser safety fabric panels from Thorlabs will be used to design optical enclosures. These panels are made of a rubber compound fabric, which can withstand high energy laser irradiation at 1064 nm. Sliding doors allow for realignment and periodic cleaning of the optics while retaining safety capability, with an opening at the baser end to connect to the laser chamber without the possibility for laser leaking out.

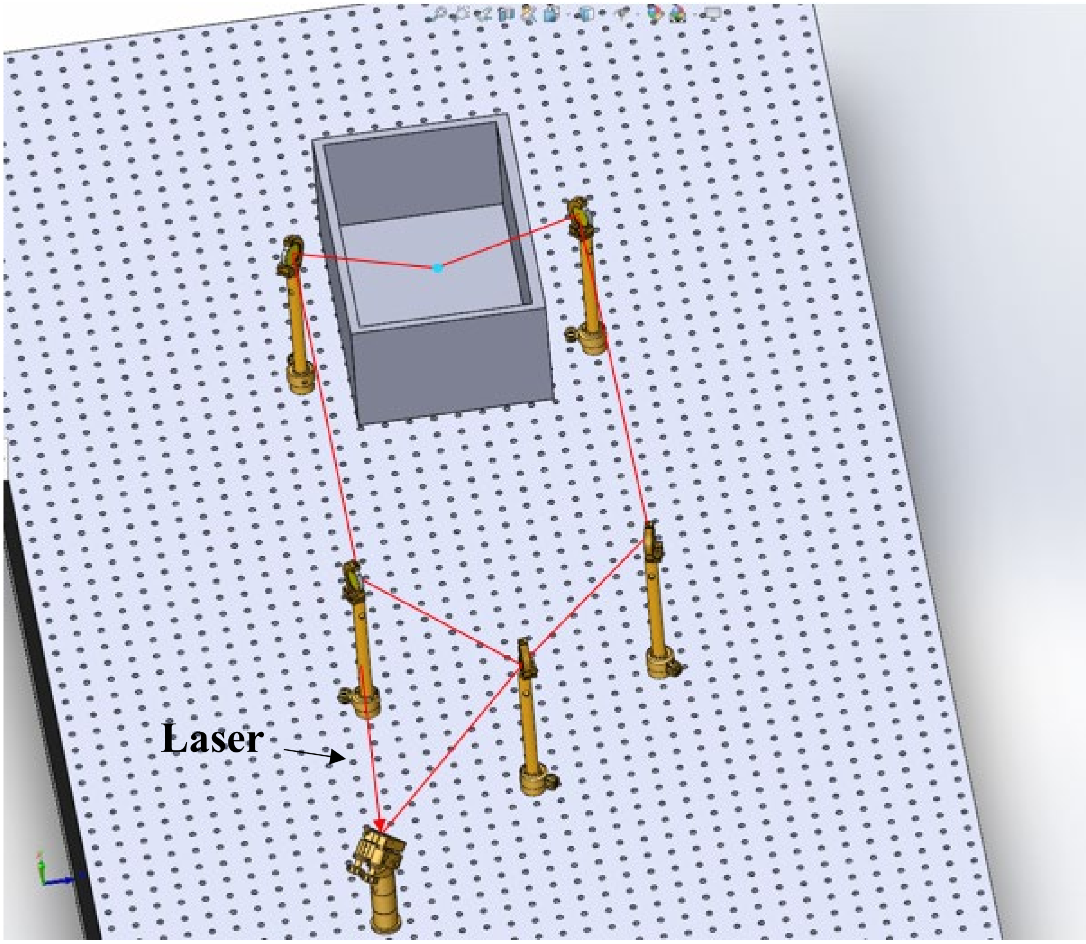

Figure 5.17. CAD model of optical setup for beam splitting system.

5.5 Conclusion

In this chapter, we presented an overview of the theory of light transport in scattering and absorbing media applied to systems undergoing laser warming for cryopreservation purposes. We examined the SAR profiles and how uniformity relates to system geometry and local optical properties. We examined several examples of laser warming including hemispherical and spherical droplets, zebrafish embryos, coral nanofragments, and multi-laser systems. These light transport simulations helped to identify the optimal optical properties of gold nanoparticles for laser nanowarming to maximize the survivable, revivable sample. We noticed several important phenomena that had been leading to unfavorable warming results, especially lensing-related hot spot formation and under-warmed zones. Monte Carlo modeling has proven to be an invaluable tool for analyzing laser-biosystem interaction.

ADAPTED FROM

Liu, Y. *et al.* Photothermal conversion of gold nanoparticles for uniform pulsed laser warming of vitrified biomaterials. *Nanoscale* **12**, 12346–12356 (2020).

Khosla, K. *et al.* Cryopreservation and Laser Nanowarming of Zebrafish Embryos Followed by Hatching and Spawning. *Adv. Biosyst.* **4**, (2020).

Zhan, L. *et al.* Conduction Cooling and Plasmonic Heating Dramatically Increase Droplet Vitrification Volumes for Cell Cryopreservation. *Adv. Sci.* **8**, 2004605 (2021).

AKNOWLEDGMENTS

This work was supported by the National Science Foundation, Grant No. 1941543, NSF Engineering Research Center for Advanced Technologies for Preservation of Biological Systems (ATP-Bio), IH SBIR Phase I (1R41OD024430-01) and Phase II (9R44MH122118-02), NIH R41 OD024430-01, and the Medtronic-Bakken Endowed Chair to John C. Bischof.

Chapter 6

Conclusion

The work presented sought to devise a theory that explained the links between nucleation, growth, phase geometry, and transformed fraction. Using a first principles approach, we linked these phenomena by deriving a nonlinear differential equation and an associated partial differential equation whose solutions allowed us to characterize a much broader class of phase change phenomena than previously possible. We determined the exact values of the Avrami parameters in isothermal systems in terms of the nucleation rate, growth rate, and fractal dimension of the phase inclusions. This allowed us to devise a process whereby the temperature dependent changes in nucleation and growth rate could be extracted from calorimetry curves, allowing for measurement of these properties from a relatively simple set of experiments. Using diffusion limited aggregation (DLA) as a model of crystallization, we simulated heat release curves and showed that the nucleation and growth rates could be recovered with high fidelity. We anticipate this method to join the standard methods for measuring these phenomena, likely replacing some of the more experimentally burdensome measurement methods.

Through ultra-rapid laser calorimetry and direct quenching experiments we built up the collective knowledge of CPA behavior and crystallization tendency in the low concentration regime. We outlined an experimental protocol for future research in this area, or adjacent fields concerned with crystallization on rapid time scales. Additionally, we created and validated a model of CPA mixing and its effects on the critical cooling and warming rates of CPA mixtures, allowing for the determination of these values for mixtures of CPAs given knowledge about their constituent parts. This is an important advancement in cryobiology as it allows for rapid screening of CPA cocktails as well as aiding in the determination of CPA concentrations within loaded and unloaded cells.

In the final chapter, we presented significant advancements in the understanding and application of laser nanowarming through the use of Monte Carlo simulations of light transport throughout various cryopreserved systems. Using these simulations, alongside optimization techniques, we were able to determine the optimal optical properties (i.e., absorption coefficient, scattering coefficient, scattering anisotropy) that maximized temperature uniformity throughout the system given some constraints such as system geometry and refractive index. This allowed us to optimize the concentrations of absorbing and scattering nanoparticles during warming, which ultimately led to a more uniform, higher viability warming protocol. Additionally, these simulations allowed for the increase in throughput of laser warming by spreading out the SAR distribution within cryopreserved, laser warmed droplets, allowing for larger droplets (and thus more biological substance) to be warmed. Finally, the simulations presented identified a key failure mode in the laser warming of spherical droplets. We discovered that the high refractive index of the droplet was causing the droplet to act as a lens, focusing the laser light within the bottom portion of the droplet, causing rapid boiling, and reducing overall cell survival. This led to a change in the cryopreservation laser warming protocol, ultimately increasing cell survival.

To summarize, the theory, models, and experiments in this work have led to a significant improvement in our understanding of phase change and how it relates to nucleation, growth, phase geometry, and transformed fraction, both during the cryopreservation process as well as in the broader sense. These advancements have led to (and will lead to) better measurement methods for nucleation rates and growth rates, a better understanding of calorimetric experiments, and more successful cryopreservation protocols.

Bibliography

1. Wilde, S. A., Valley, J. W., Peck, W. H. & Graham, C. M. Evidence from detrital zircons for the existence of continental crust and oceans on the Earth 4.4 Gyr ago. *Nature* **409**, 175+ (2001).
2. Mojzsis, S. J., Harrison, T. M. & Pidgeon, R. T. Oxygen-isotope evidence from ancient zircons for liquid water at the Earth's surface 4,300 Myr ago. *Nature* **409**, 178–181 (2001).
3. Bell, E. A., Boehnke, P., Harrison, T. M. & Mao, W. L. Potentially biogenic carbon preserved in a 4.1 billion-year-old zircon. *Proc. Natl. Acad. Sci.* **112**, 14518–14521 (2015).
4. Chen, Y. & Zhang, L. Introduction BT - Polishing of Diamond Materials: Mechanisms, Modeling and Implementation. in (eds. Chen, Y. & Zhang, L.) 1–10 (Springer London, 2013). doi:10.1007/978-1-84996-408-1_1.
5. Libbrecht, K. G. Physical Dynamics of Ice Crystal Growth. *Annu. Rev. Mater. Res.* **47**, 271–295 (2017).
6. Pegg, D. E. Mechanisms of freezing damage. *Symp. Soc. Exp. Biol.* **41**, 363–378 (1987).
7. Menegalli, F. C. & Calvelo, A. Dendritic growth of ice crystals during the freezing of beef. *Meat Sci.* **3**, 179–198 (1979).
8. Salzmann, C., Radaelli, P., Finney, J. & Mayer, E. A calorimetric study on the low temperature dynamics of doped ice V and its reversible phase transition to hydrogen ordered ice XIII. *Phys. Chem. Chem. Phys.* **10**, 6313–6324 (2008).
9. MAZUR, P. Stopping Biological Time: The Freezing of Living Cells. *Ann. N. Y. Acad. Sci.* **541**, 514–531 (1988).
10. Karthika, S., Radhakrishnan, T. K. & Kalaichelvi, P. A Review of Classical and Nonclassical Nucleation Theories. *Cryst. Growth Des.* **16**, 6663–6681 (2016).
11. Nyquist, R. M., Talanquer, V. & Oxtoby, D. W. Density functional theory of nucleation: A semiempirical approach. *J. Chem. Phys.* **103**, 1175–1179 (1995).
12. Erdemir, D., Lee, A. Y. & Myerson, A. S. Nucleation of Crystals from Solution: Classical and Two-Step Models. *Acc. Chem. Res.* **42**, 621–629 (2009).
13. Saridakis, E. & Chayen, N. E. Towards a 'universal' nucleant for protein crystallization. *Trends Biotechnol.* **27**, 99–106 (2009).

14. Baidakov, V. G. & Tipeev, A. O. Crystal nucleation and the solid-liquid interfacial free energy. *J. Chem. Phys.* **136**, (2012).

15. Němec, T. Estimation of ice-water interfacial energy based on pressure-dependent formulation of classical nucleation theory. *Chem. Phys. Lett.* **583**, 64–68 (2013).

16. Zeldovich, Y. No Title. *Zh. Eksp. Teor. Fiz.* **12**, (1942).

17. Kelton, K. F. & Greer, A. L. Chapter 6 - Heterogeneous Nucleation. in *Nucleation in Condensed Matter* (eds. Kelton, K. F. & Greer, A. L. B. T.-P. M. S.) vol. 15 165–226 (Pergamon, 2010).

18. Málek, J., Barták, J. & Shánělová, J. Spherulitic Crystal Growth Velocity in Selenium Supercooled Liquid. *Cryst. Growth Des.* **16**, 5811–5821 (2016).

19. Jonsson, T. On the one dimensional Stefan problem. 041004 (2013).

20. Takahashi, M., Nagahama, H., Masuda, T. & Fujimura, A. Fractal analysis of experimentally, dynamically recrystallized quartz grains and its possible application as a strain rate meter. *J. Struct. Geol.* **20**, 269–275 (1998).

21. Libbrecht, K. G. Physical Dynamics of Ice Crystal Growth. *Annu. Rev. Mater. Res.* **47**, 271–295 (2017).

22. Devos, C., Van Gerven, T. & Kuhn, S. A Review of Experimental Methods for Nucleation Rate Determination in Large-Volume Batch and Microfluidic Crystallization. *Cryst. Growth Des.* **21**, 2541–2565 (2021).

23. Cedeno, R., Maosoongnern, S. & Flood, A. Direct Measurements of Primary Nucleation Rates of p-Aminobenzoic Acid and Glutamic Acid and Comparison with Predictions from Induction Time Distributions. *Ind. Eng. Chem. Res.* **57**, 17504–17515 (2018).

24. Brus, D., Hyvärinen, A.-P., Ždímal, V. & Lihavainen, H. Homogeneous nucleation rate measurements of 1-butanol in helium: A comparative study of a thermal diffusion cloud chamber and a laminar flow diffusion chamber. *J. Chem. Phys.* **122**, 214506 (2005).

25. Chen, J. *et al.* Measuring the activation energy barrier for the nucleation of single nanosized vapor bubbles. *Proc. Natl. Acad. Sci. U. S. A.* **116**, 12678–12683 (2019).

26. Sosso, G. C. *et al.* Crystal Nucleation in Liquids: Open Questions and Future Challenges in Molecular Dynamics Simulations. *Chem. Rev.* **116**, 7078–7116 (2016).

27. Weinberg, M. C., Zelinski, B. J., Uhlmann, D. R. & Zanotto, E. D. Critical cooling rate calculations for glass formation. *J. Non. Cryst. Solids* **123**, 90–96 (1990).

28. Xu, Y., Petrik, N. G., Smith, R. S., Kay, B. D. & Kimmel, G. A. Growth rate of

crystalline ice and the diffusivity of supercooled water from 126 to 262 K. *Proc. Natl. Acad. Sci. U. S. A.* **113**, 14921–14925 (2016).

29. Špillar, V. & DolejŠ, D. Calculation of Time-dependent Nucleation and Growth Rates from Quantitative Textural Data: Inversion of Crystal Size Distribution. *J. Petrol.* **54**, 913–931 (2013).

30. Whaley, D. *et al.* Cryopreservation: An Overview of Principles and Cell-Specific Considerations. *Cell Transplant.* **30**, 1–12 (2021).

31. Stokes, P. J. *et al.* Metabolism of human embryos following cryopreservation: Implications for the safety and selection of embryos for transfer in clinical IVF. *Hum. Reprod.* **22**, 829–835 (2007).

32. Hernández-Tapia, L. G. *et al.* Effects of Cryopreservation on Cell Metabolic Activity and Function of Biofabricated Structures Laden with Osteoblasts. *Materials* vol. 13 (2020).

33. Hopkins, J. B., Badeau, R., Warkentin, M. & Thorne, R. E. Effect of common cryoprotectants on critical warming rates and ice formation in aqueous solutions. *Cryobiology* **65**, 169–178 (2012).

34. Elliott, G. D., Wang, S. & Fuller, B. J. Cryoprotectants: A review of the actions and applications of cryoprotective solutes that modulate cell recovery from ultra-low temperatures. *Cryobiology* **76**, 74–91 (2017).

35. Vitrification in Assisted Reproduction. *Vitrification in Assisted Reproduction* (2007) doi:10.3109/9780203090022.

36. Rahman, A. T. *et al.* Ice recrystallization is strongly inhibited when antifreeze proteins bind to multiple ice planes. *Sci. Rep.* **9**, 2212 (2019).

37. Han, Z. & Bishop, J. PERSPECTIVE: Critical Cooling and Warming Rates as a Function of CPA Concentration. *Cryo Letters* **41**, 185–193 (2020).

38. Woods, E. J., Thirumala, S., Badhe-Buchanan, S. S., Clarke, D. & Mathew, A. J. Off the shelf cellular therapeutics: Factors to consider during cryopreservation and storage of human cells for clinical use. *Cytotherapy* **18**, 697–711 (2016).

39. Kangas, J. *et al.* Ultra-Rapid Laser Calorimetry for the Assessment of Crystallization in Low-Concentration Cryoprotectants. *J. Heat Transfer* **144**, 1–9 (2022).

40. Zhan, L. *et al.* Rapid joule heating improves vitrification based cryopreservation. *Nat. Commun.* **13**, 6017 (2022).

41. Bissoyi, A. & Braslavsky, I. Adherent cell thawing by infrared radiation. *Cryobiology* **103**, 129–140 (2021).

42. Etheridge, M. L. *et al.* RF heating of magnetic nanoparticles improves the thawing of cryopreserved biomaterials. *TECHNOLOGY* **02**, 229–242 (2014).

43. Sharma, A. *et al.* Vitrification and Nanowarming of Kidneys. *Adv. Sci.* **8**, 2101691 (2021).

44. Kolmogorov, A. On the Statistical Theory of Crystallization of Metals. *Izv. Akad. Nauk SSSR, Ser. Mat.* **3**, 355–359 (1937).

45. Avrami, M. Kinetics of phase change. I: General theory. *J. Chem. Phys.* **7**, 1103–1112 (1939).

46. Avrami, M. Kinetics of phase change. II Transformation-time relations for random distribution of nuclei. *J. Chem. Phys.* **8**, 212–224 (1940).

47. Avrami, M. Granulation, phase change, and microstructure kinetics of phase change. III. *J. Chem. Phys.* **9**, 177–184 (1941).

48. Farjas, J. & Roura, P. Modification of the Kolmogorov-Johnson-Mehl-Avrami rate equation for non-isothermal experiments and its analytical solution. *Acta Mater.* **54**, 5573–5579 (2006).

49. Vázquez, J., López-Alemany, P. L., Villares, P. & Jiménez-Garay, R. Generalization of the Avrami equation for the analysis of non-isothermal transformation kinetics. Application to the crystallization of the Cu0.20As0.30Se0.50 alloy. *J. Phys. Chem. Solids* **61**, 493–500 (2000).

50. Lambrigger, M. Non-Isothermal Crystallization Kinetics of Poly(ethylene terephthalate) from the Point of View of Isokinetic Models. *Polym. J.* **30**, 262–264 (1998).

51. Kelton, K. F. Numerical model for isothermal and non-isothermal crystallization of liquids and glasses. *J. Non. Cryst. Solids* **163**, 283–296 (1993).

52. Holten, V., Bertrand, C. E., Anisimov, M. A. & Sengers, J. V. Thermodynamics of supercooled water. *J. Chem. Phys.* **136**, 1–23 (2012).

53. Sear, R. P. Nucleation: Theory and applications to protein solutions and colloidal suspensions. *J. Phys. Condens. Matter* **19**, 0–28 (2007).

54. Turnbull, D. & Fisher, J. C. Rate of nucleation in condensed systems. *J. Chem. Phys.* **17**, 71–73 (1949).

55. Dehaoui, A., Issenmann, B. & Caupin, F. Viscosity of deeply supercooled Water and its coupling to molecular diffusion. *Proc. Natl. Acad. Sci. U. S. A.* **112**, 12020–12025 (2015).

56. Adam, G. & Gibbs, J. H. On the temperature dependence of cooperative relaxation

properties in glass-forming liquids. *J. Chem. Phys.* **43**, 139–146 (1965).

57. Limmer, D. T. & Chandler, D. Corresponding states for mesostructure and dynamics of supercooled water. *Faraday Discuss.* **167**, 485–498 (2013).

58. Elmatad, Y. S., Chandler, D. & Garrahan, J. P. Corresponding States of Structural Glass Formers The variation with respect to temperature T of transport properties of 58 fragile structural glass-forming liquids (67 data sets in total) are analyzed and shown to exhibit a remarkable degree of universa. *Glass* **2**, 5563–5567 (2009).

59. Kangas, J., Bischof, J. C. & Hogan, C. J. Kinetics of nonisothermal phase change with arbitrary temperature-time history and initial transformed phase distributions. *J. Chem. Phys.* **155**, (2021).

60. Wood, S. E., Baker, M. B. & Swanson, B. D. Instrument for studies of homogeneous and heterogeneous ice nucleation in free-falling supercooled water droplets. *Rev. Sci. Instrum.* **73**, 3988 (2002).

61. Kimmel, G. A. *et al.* Homogeneous ice nucleation rates and crystallization kinetics in transiently-heated, supercooled water films from 188 K to 230 K. *J. Chem. Phys.* **150**, (2019).

62. Manka, A. A. *et al.* Nucleation of ethanol, propanol, butanol, and pentanol: A systematic experimental study along the homologous series. *J. Chem. Phys.* **137**, 54316 (2012).

63. Hagen, D. E., Anderson, R. J. & Kassner, J. L. Homogeneous Condensation—Freezing Nucleation Rate Measurements for Small Water Droplets in an Expansion Cloud Chamber. *J. Atmos. Sci.* **38**, 1236–1243 (1981).

64. Pruppacher, H. R. Interpretation of experimentally determined growth rates of ice crystals in supercooled water. *J. Chem. Phys.* **47**, 1807–1813 (1967).

65. Perkins, S. J. Protein volumes and hydration effects. *Eur. J. Biochem.* **157**, 169–180 (1986).

66. Liu, J., Nicholson, C. E. & Cooper, S. J. Direct measurement of critical nucleus size in confined volumes. *Langmuir* **23**, 7286–7292 (2007).

67. Boutron, P. & Mehl, P. Theoretical prediction of devitrification tendency: Determination of critical warming rates without using finite expansions. *Cryobiology* **27**, 359–377 (1990).

68. Koralay, H., Cavdar, S. & Aksan, M. A. Kinetics of non-isothermal crystallization of Bi3Sr 2Ca2Cu3-xSnxO10δ glassceramics. *Phys. B Condens. Matter* **405**, 4801–4805 (2010).

69. Warkentin, M., Stanislavskaia, V., Hammes, K. & Thorne, R. E. Cryocrystallography in capillaries: Critical glycerol concentrations and cooling rates. *J. Appl. Crystallogr.* **41**, 791–797 (2008).

70. Bruggeller, P. & Mayer, E. Complete vitrification in pure liquid water and dilute aqueous solutions. *Nature* **288**, 569–571 (1980).

71. Schawe, J. E. K. & Löffler, J. F. Existence of multiple critical cooling rates which generate different types of monolithic metallic glass. *Nat. Commun.* **10**, 1–10 (2019).

72. Zhang, Y. *et al.* Avrami kinetic-based constitutive relationship for armco-type pure iron in hot deformation. *Metals (Basel).* **9**, (2019).

73. McHenry, M. E., Willard, M. A. & Laughlin, D. E. *Amorphous and nanocrystalline materials for applications as soft magnets. Progress in Materials Science* vol. 44 (1999).

74. Nishiyama, N. & Inoue, A. Supercooling investigation and critical cooling rate for glass formation in Pd-Cu-Ni-P alloy. *Acta Mater.* **47**, 1487–1495 (1999).

75. Yang, J., McCoy, B. J. & Madras, G. Distribution kinetics of polymer crystallization and the Avrami equation. *J. Chem. Phys.* **122**, (2005).

76. Wang, R.-Y. *et al.* A Generalized Avrami Equation for Crystallization Kinetics of Polymers with Concomitant Double Crystallization Processes. *Cryst. Growth & Des.* **17**, 5908–5917 (2017).

77. Capece, M. & Davé, R. Enhanced physical stability of amorphous drug formulations via dry polymer coating. *J. Pharm. Sci.* **104**, 2076–2084 (2015).

78. Mehl, P. Isothermal and non-isothermal crystallization during warming in aqueous solutions of 1,3-butanediol: Comparison of calorimetry and cryomicroscopy. *Thermochim. Acta* **155**, 187–202 (1989).

79. Mehl, P. M. Nucleation and Crystal Growth in a Vitrification Solution Tested for Organ Cryopreservation by Vitrification. *Cryobiology* **30**, 509–518 (1993).

80. Málek, J. The applicability of Johnson-Mehl-Avrami model in the thermal analysis of the crystallization kinetics of glasses. *Thermochim. Acta* **267**, 61–73 (1995).

81. Weinberg, M. C., Birnie, D. P. & Shneidman, V. A. Crystallization kinetics and the JMAK equation. *J. Non. Cryst. Solids* **219**, 89–99 (1997).

82. Matsui, T., Ogawa, T. & Adachi, Y. Relationship between three-dimensional microstructure and Avrami exponent for recrystallization in pure iron. *Results Mater.* **1**, 100002 (2019).

83. Saeki, R. & Ohgai, T. Determination of crystal growth geometry factors and

nucleation site densities of electrodeposited ferromagnetic cobalt nanowire arrays. *Crystals* **9**, (2019).

84. Lorenzo, A. T., Arnal, M. L., Albuerne, J. & Müller, A. J. DSC isothermal polymer crystallization kinetics measurements and the use of the Avrami equation to fit the data: Guidelines to avoid common problems. *Polym. Test.* **26**, 222–231 (2007).

85. Witten, TA, Sander, L., Witten, T. A. & Sander, L. M. Diffusion-Limited Aggregation, a Kinetic Critical Phenomenon. *Phys. Rev. Lett.* **47**, 1400–1403 (1981).

86. Ball, R. C. Large scale lattice effect in diffusion-limited aggregation. *J. Phys. A. Math. Gen.* **18**, L809-LS13 (1985).

87. Rayleigh, Lord. VIII. On the pressure developed in a liquid during the collapse of a spherical cavity. *London, Edinburgh, Dublin Philos. Mag. J. Sci.* **34**, 94–98 (1917).

88. Plesset, M. S. & Prosperetti, A. Bubble Dynamics and Cavitation. *Annu. Rev. Fluid Mech.* **9**, 145–185 (1977).

89. Wolkers, W. F. & Oldenhof, H. *Cryopreservation and Freeze- Drying Protocols-third edition.* (2015).

90. Wowk, B. How cryoprotectants work. *Cryonics* **3**, 28 (2007).

91. Muldrew, K. & McGann, L. E. Mechanisms of intracellular ice formation. *Biophys. J.* **57**, 525–532 (1990).

92. Takamatsu, H. & Zawlodzka, S. Contribution of extracellular ice formation and the solution effects to the freezing injury of PC-3 cells suspended in NaCl solutions. *Cryobiology* **53**, 1–11 (2006).

93. Best, B. P. Cryoprotectant Toxicity: Facts, Issues, and Questions. *Rejuvenation Res.* **18**, 422–436 (2015).

94. Fahy, G. M., Lilley, T. H., Linsdell, H., Douglas, M. S. J. & Meryman, H. T. Cryoprotectant toxicity and cryoprotectant toxicity reduction: In search of molecular mechanisms. *Cryobiology* **27**, 247–268 (1990).

95. Khosla, K., Wang, Y., Hagedorn, M., Qin, Z. & Bischof, J. Gold Nanorod Induced Warming of Embryos from the Cryogenic State Enhances Viability. *ACS Nano* **11**, 7869–7878 (2017).

96. Guthrie, H. D., Liu, J. & Critser, J. K. Osmotic tolerance limits and effects of cryoprotectants on motility of bovine spermatozoa. *Biol. Reprod.* **67**, 1811–1816 (2002).

97. Szurek, E. A. & Eroglu, A. Comparison and avoidance of toxicity of penetrating cryoprotectants. *PLoS One* **6**, (2011).

98. Marques, L. S. *et al.* Slow freezing versus vitrification for the cryopreservation of zebrafish (Danio rerio) ovarian tissue. *Sci. Rep.* **9**, 1–11 (2019).

99. Zhao, J., Simon, S. L. & McKenna, G. B. Using 20-million-year-old amber to test the super-Arrhenius behaviour of glass-forming systems. *Nat. Commun.* **4**, 1–6 (2013).

100. Abidalla, M. & Roversi, P. F. Vitrification Assessment: Thermal Analysis of Cryoprotective Aqueous Solutions 1,2 Propanediol and Ethylene Glycol. *Biopreserv. Biobank.* **16**, 207–216 (2018).

101. Berejnov, V., Husseini, N. S., Alsaied, O. A. & Thorne, R. E. Effects of cryoprotectant concentration and cooling rate on vitrification of aqueous solutions. *J. Appl. Crystallogr.* **39**, 244–251 (2006).

102. Wowk, B., Fahy, G. M., Ahmedyar, S., Taylor, M. J. & Rabin, Y. Vitrification tendency and stability of DP6-based vitrification solutions for complex tissue cryopreservation. *Cryobiology* **82**, 70–77 (2018).

103. Yi, F. & Lavan, D. A. Nanocalorimetry: Exploring materials faster and smaller. *Appl. Phys. Rev.* **6**, (2019).

104. Minakov, A. A. & Schick, C. Ultrafast thermal processing and nanocalorimetry at heating and cooling rates up to 1 MKs. *Rev. Sci. Instrum.* **78**, (2007).

105. Gregson, F. K. A. *et al.* Studies of competing evaporation rates of multiple volatile components from a single binary-component aerosol droplet. *Phys. Chem. Chem. Phys.* **21**, 9709–9719 (2019).

106. Furuta, T., Sakai, M., Isobe, T. & Nakajima, A. Evaporation behavior of microliter- and sub-nanoliter-scale water droplets on two different fluoroalkylsilane coatings. *Langmuir* **25**, 11998–12001 (2009).

107. Kuhn, T., Earle, M. E., Khalizov, A. F. & Sloan, J. J. Size dependence of volume and surface nucleation rates for homogeneous freezing of supercooled water droplets. *Atmos. Chem. Phys.* **11**, 2853–2861 (2011).

108. Song, Y. S. *et al.* Vitrification and levitation of a liquid droplet on liquid nitrogen. *Proc. Natl. Acad. Sci. U. S. A.* **107**, 4596–4600 (2010).

109. Su, F., Zhao, N., Deng, Y. & Ma, H. An Ultrafast Vitrification Method for Cell Cryopreservation. *J. Heat Transfer* **140**, 1–4 (2018).

110. Su, F. *et al.* Thin-film evaporation heat transfer of liquid nitrogen and its application in cell vitrification. *J. Heat Transfer* **142**, 1–6 (2020).

111. Daly, J. *et al.* Successful cryopreservation of coral larvae using vitrification and laser warming. *Sci. Rep.* **8**, 1–10 (2018).

112. Khosla, K. *et al.* Characterization of Laser Gold Nanowarming: A Platform for Millimeter-Scale Cryopreservation. *Langmuir* **35**, 7364–7375 (2019).

113. Kuwayama, M., Vajta, G., Kato, O. & Leibo, S. P. Highly efficient vitrification method for cryopreservation of human oocytes. *Reprod. Biomed. Online* **11**, 300–308 (2005).

114. Kuwayama, M. Highly efficient vitrification for cryopreservation of human oocytes and embryos: The Cryotop method. *Theriogenology* **67**, 73–80 (2007).

115. Kleinhans, F. W., Seki, S. & Mazur, P. Simple, inexpensive attainment and measurement of very high cooling and warming rates. *Cryobiology* **61**, 231–233 (2010).

116. Liu, Y. *et al.* Photothermal conversion of gold nanoparticles for uniform pulsed laser warming of vitrified biomaterials. *Nanoscale* **12**, 12346–12356 (2020).

117. Wowk, B., Darwin, M., Harris, S. B., Russell, S. R. & Rasch, C. M. Effects of solute methoxylation on glass-forming ability and stability of vitrification solutions. *Cryobiology* **39**, 215–227 (1999).

118. Baudot, A., Alger, L. & Boutron, P. Glass-forming tendency in the system water-dimethyl sulfoxide. *Cryobiology* **40**, 151–158 (2000).

119. Xue, X., Jin, H. L., He, Z. Z. & Liu, J. Quantifying the growth rate and morphology of ice crystals growth in cryoprotectants via high-speed camera and cryomicroscope. *J. Heat Transfer* **137**, 1–5 (2015).

120. Kuleshova, L. L., MacFarlane, D. R., Trounson, A. O. & Shaw, J. M. Sugars exert a major influence on the vitrification properties of ethylene glycol-based solutions and have low toxicity to embryos and oocytes. *Cryobiology* **38**, 119–130 (1999).

121. Lankhorst, D., Schriever, J. & Leyte, J. C. Determination of the Rotational Correlation Time of Water by Proton NMR Relaxation in H217O and Some Related Results. *Berichte der Bunsengesellschaft für Phys. Chemie* **86**, 215–221 (1982).

122. Welch, A. J. & Van Gemert, M. J. C. *Optical-thermal response of laser-irradiated tissue. Optical-Thermal Response of Laser-Irradiated Tissue* (2011). doi:10.1007/978-90-481-8831-4.

123. Wang, T., Zhao, G., Tang, H. & Jiang, Z. DETERMINATION OF CONVECTIVE HEAT TRANSFER COEFFICIENT AT THE OUTER SURFACE OF A CRYOVIAL BEING PLUNGED INTO. **36**, 285–288 (2015).

124. Keblinski, P., Cahill, D. G., Bodapati, A., Sullivan, C. R. & Taton, T. A. Limits of localized heating by electromagnetically excited nanoparticles. *J. Appl. Phys.* **100**, (2006).

125. Qin, Z. & Bischof, J. C. Thermophysical and biological responses of gold nanoparticle laser heating. *Chem. Soc. Rev.* **41**, 1191–1217 (2012).

126. Choi, J. H. & Bischof, J. C. A quantitative analysis on the thermal properties of phosphate buffered saline with glycerol at subzero temperatures. *International Journal of Heat and Mass Transfer* vol. 51 640–649 (2008).

127. Schellenberg, M. W. & Hunt, H. K. Hand-held optoacoustic imaging: A review. *Photoacoustics* **11**, 14–27 (2018).

128. Everall, N., Hahn, T., Matousek, P., Parker, A. W. & Towrie, M. Photon Migration in Raman Spectroscopy. *Appl. Spectrosc.* **58**, 591–597 (2004).

129. Huang, X., El-Sayed, I. H., Qian, W. & El-Sayed, M. A. Cancer Cell Imaging and Photothermal Therapy in the Near-Infrared Region by Using Gold Nanorods. *J. Am. Chem. Soc.* **128**, 2115–2120 (2006).

130. Khosla, K. *et al.* Cryopreservation and Laser Nanowarming of Zebrafish Embryos Followed by Hatching and Spawning. *Adv. Biosyst.* **4**, (2020).

131. Bhatnagar, P. L., Gross, E. P. & Krook, M. A Model for Collision Processes in Gases. I. Small Amplitude Processes in Charged and Neutral One-Component Systems. *Phys. Rev.* **94**, 511–525 (1954).

132. Harrison, R. L. Introduction To Monte Carlo Simulation. *AIP Conf. Proc.* **1204**, 17–21 (2010).

133. Rabin, Y., Steif, P. S., Hess, K. C., Jimenez-Rios, J. L. & Palastro, M. C. Fracture formation in vitrified thin films of cryoprotectants. *Cryobiology* **53**, 75–95 (2006).

134. Khosla, K., Wang, Y., Hagedorn, M., Qin, Z. & Bischof, J. Gold Nanorod Induced Warming of Embryos from the Cryogenic State Enhances Viability. *ACS Nano* **11**, 7869–7878 (2017).

135. Eustis, S. & El-Sayed, M. A. Why gold nanoparticles are more precious than pretty gold: Noble metal surface plasmon resonance and its enhancement of the radiative and nonradiative properties of nanocrystals of different shapes. *Chem. Soc. Rev.* **35**, 209–217 (2006).

136. Qin, Z. *et al.* Significantly Improved Analytical Sensitivity of Lateral Flow Immunoassays by Using Thermal Contrast. *Angew. Chemie* **124**, 4434–4437 (2012).

137. Jacques, S. L. Optical properties of biological tissues: a review. *Phys. Med. Biol.* **58**, R37–R61 (2013).

138. Choi, J. & Bischof, J. C. Review of biomaterial thermal property measurements in the cryogenic regime and their use for prediction of equilibrium and non-equilibrium

freezing applications in cryobiology. *Cryobiology* **60**, 52–70 (2010).

139. Otanicar, T. P., Phelan, P. E. & Golden, J. S. Optical properties of liquids for direct absorption solar thermal energy systems. *Sol. Energy* **83**, 969–977 (2009).

140. Hu, Y., Fleming, R. C. & Drezek, R. A. Optical properties of gold-silica-gold multilayer nanoshells. *Opt. Express* **16**, 19579 (2008).

141. He, G. S. *et al.* Scattering and Absorption Cross-Section Spectral Measurements of Gold Nanorods in Water. *J. Phys. Chem. C* **114**, 2853–2860 (2010).

142. Zhan, L. *et al.* Conduction Cooling and Plasmonic Heating Dramatically Increase Droplet Vitrification Volumes for Cell Cryopreservation. *Adv. Sci.* **8**, 2004605 (2021).

143. Pickering, J. W. Optical property changes as a result of protein denature in albumen and yolk. *J. Photochem. Photobiol. B Biol.* **16**, 101–111 (1992).

144. Liu, Y. *et al.* Photothermal conversion of gold nanoparticles for uniform pulsed laser warming of vitrified biomaterials. *Nanoscale* **12**, 12346–12356 (2020).

145. Hughes, T. P. Skeletal density and growth form of corals. *Mar. Ecol. Prog. Ser.* **35**, 259–266 (1987).

146. Davidson, S. R. H. & James, D. F. Measurement of thermal conductivity of bovine cortical bone. *Med. Eng. & Phys.* **22**, 741–747 (2000).

147. Huiskes, R. & Chao, E. Y. S. A survey of finite element analysis in orthopedic biomechanics: The first decade. *J. Biomech.* **16**, 385–409 (1983).